STRUCTURAL, ELECTRICAL AND OPTICAL STUDY OF 'A' SITE DEFICIENT HETEROVALENT ION DOPED BARIUM ZIRCONIUM TITANATE PEROVSKITE

A thesis by

Tanmaya Badapanda

for the award of the degree

of

DOCTOR OF PHILOSOPHY

DEPARTMENT OF PHYSICS
NATIONAL INSTITUTE OF TECHNOLOGY
ROURKELA, ORISSA-INDIA-769008

SEPTEMBER - 2010

.

DECLARATION

I here by declare that thesis entitled "**STRUCTURAL, ELECTRICAL AND OPTICAL STUDY OF 'A' SITE DEFICIENT HETEROVALENT ION DOPED BARRIUM ZIRCONIUM TITANATE PEROVSKITE**" which is being submitted by me to National Institute of Technology for the award of degree of **Doctor of Philosophy** is original and authentic work conducted by me in the Department of Physics, National Institute of Technology, Rourkela under the supervision of **Prof. S. Panigrahi**, Department of Physics, National Institute of Technology, Rourkela. No part or full form of this thesis work has been submitted elsewhere for a similar or any other degree.

Date: Tanmaya Badapanda

CERTIFICATE

This is to certify that the thesis entitled "**STRUCTURAL, ELECTRICAL AND OPTICAL STUDY OF 'A' SITE DEFICIENT HETEROVALENT ION DOPED BARRIUM ZIRCONIUM TITANATE PEROVSKITE**" submitted by **Tanmaya Badapanda** to the National Institute of Technology, Rourkela for the award of the degree of Doctor of Philosophy is a bonafide record of research work carried out by him under my supervision. In my opinion, the work fulfills the requirements for which it is being submitted. The contents of the thesis, in full or in parts, have not been submitted to any other Institute or University for the award of any degree or diploma.

Signature of Supervisor

Prof. S. Panigrahi,
Department of Physics,
National Institute of Technology,
Rourkela-769008

ACKNOWLEDGEMENTS

The five years, I have spent at National Institute of Technology, Rourkela given me a source of most precious experience in my life. I take the opportunity to acknowledge all those who directly or indirectly helped me throughout this difficult journey.

Foremost, I would like to express my deep sense of gratitude to **Dr.S.Panigrahi** for his guidance, lively discussion, constant encouragement, expert advice, constructive and honest criticism. I am greatly indebted to him for providing me excellent freedom to work on what I was interested in. He is excellent mentor and very supportive throughout the work.

I extended my heart-felt thanks to **Dr. T.P.Sinha** and **Dr. Alo Dutta**, Bose Institute, Kolkata for their wholehearted suggestion and cooperation to carry out all the dielectric measurements.

I sincerely thank to **Dr. L.S.Cavalcante**, Universidade Federal de S˜ao Carlos, Brazil for his wholehearted cooperation for carryout XANEF and Optical properties.

I also must acknowledge **Dr.S. K. Sarangi**, Director, National institute of Technology, Rourkela for providing me a platform to carry out this research.

I also would like to express my gratitude to the rest of my doctoral scrutiny committee members: **Dr.D.K.Bisoyi, Dr.S.K.Jena, Dr.B.K.Ojha** for their invaluable, insightful comments and suggestions that improved the quality of this work.

I am extremely thankful to all the supporting and technical staff of the Department of Physics and Department of Materials and Metallurgical Engineering for their help as and when required without which I have been in troubled waters.

I would also like to acknowledge the contribution of my friends and colleagues. **Dr. S.K.Rout, Mr. Santosh Sahoo, Mr. Subasish Sarangi,** and **Mr. V. Senthil,** deserve special thanks for their timely help and cooperation during this study.

Finnaly, I owe a deep sense of indeptedness to my beloved parents **Mr. Harachand Badapanda** and **Mrs. Anjali Badapanda** for their affection, wholehearted, untiring and immeasurebale support at every stage of my life. I am gratefully indepted to my brother **Mr. Chinmaya Badapanda,** sister **Mrs. Trupti Dash** and to all my family members for their umsinted moral support, encouragement and wishes throughout the course of the work.

Tanmaya Badapanda
September 2010

ABSTARCT

In view of the processing and environmental issues pertaining to lead based ferroelectric materials, investigations on lead free ferroelectrics are carried intensively in recent years. These materials are interesting because, they are flexible with respect to structural changes and functional properties. These materials have potential device applications such as capacitors, sensors, actuators, and memory storage and microwave devices. This thesis is an attempt to elucidate the effect of substitution of heterovalent ions (Bi, Y, Dy) on the 'A' site of Barium Zirconium Titanate $BaZr_{0.25}Ti_{0.75}O_3$ (BZT) pervoskite. Their structural, morphological, electrical and optical properties are investigated. The XRD study on the ceramic compositions showed single phase cubic perovsite structure at room temperature. The existence of Raman active modes in $BaZr_{0.25}Ti_{0.75}O_3$ is associated with the structural order-disorder at short-range into the lattice due to the presence of polar [TiO_6] distorted clusters. The SEM micrograph shows that the grains are uniformly distributed throughout the surface and the average grain size decreases with substitution heterovalent ion doping in $BaZr_{0.25}Ti_{0.75}O_3$ ceramic. The dielectric study confirmed the relaxor nature of the heterovalent ions doped ceramic and the transition temperature (T_m), dielectric permittivity and dielectric loss are decreasing with

increase in heterovalent ions concentration .The diffusivity of ceramics increases with increase in heterovalent ions concentration. The impedance and modulus spectroscopy were employed to evaluate the different electrical properties of the grain and grain boundary of the ceramics. The optical band gaps were calculated from UV –Visible spectroscopy ceramic suggested the presence of intermediary energy levels within the band gap. The Photo luminescent study of heterovalent ions doped $BaZr_{0.25}Ti_{0.75}O_3$, when excited with 350 nm wavelength at room temperature, exhibited broad PL band with a maximum emission in blue region.

Keywords: *Ferroelectrics, Relaxor ferroelectrics, Diffuse phase transition, Dielectric relaxation, Raman spectroscopy, Impedance spectroscopy, UV–vis absorption spectroscopy, Photoluminescence, X-ray absorption near-edge spectroscopy analyses.*

CONTENTS

List of Tables

List of Figures

INTRODUCTION

Chapter 1 introduces the basic concepts of dielectricity, ferroelectricity and piezoelectricity. A brief introduction about the classification of dielectrics and theory of dielectric classification, theory of the dielectric polarization phenomenon are presented. The phenomenon of ferroelectricity and piezoelectricity are discussed in detail. The classification of crystal systems and the interrelationship between the piezoelectrics and subgroups with respect to symmetry of crystal structure is presented. The basic understanding of the perovskite structure is elaborated and systems that possess this structure are discussed. The summary of few models explaining relaxor behavior have been presented and finally, the objective of the present work is highlighted.

Chapter 2 contains details of the experimental techniques used for preparation, structural characterization as well as to measure the dielectric and optical properties of materials.

Chapter 3 explains the phase formation of polycrystalline $BaZr_xTi_{1-x}O_3$ (x=0.05-0.25) ceramic. The details structural study of $BaZr_{0.25}Ti_{0.75}O_3$ ceramics was done by the help of X-ray diffraction and Reitveld analysisi. The microstructural and compositional study was done by scanning electron microscope and Energy Dispersive X-ray spectroscopy respectively. The dielectric study of $BaZr_{0.25}Ti_{0.75}O_3$ reveals that the composition shows relaxor behavior. The impedance study shows two semicircle arcs within the studied temperature. The sample shows negative temperature coefficient of resistivity (NTCR) effect as the grain and grain boundary resistance decreases with increase in temperature

Chapter 4 contains the dielectric and AC conductivity study of Bismuth (Bi^{+3}) ion doped $BaZr_{0.25}Ti_{0.75}O_3$ ceramic. The polycrystalline $Ba_{1-x}Bi_{2x/3}Zr_{0.25}Ti_{0.75}O_3$ (x= 0.025, 0.05) ceramic has been prepared by solid state reaction route. The sample shows well developed and relatively equal shaped grains as the Bismuth content increases and the size of the grains decreases with the increase in Bismuth concentration. The dielectric study reveals that the material shows relaxor behavior with decrease in magnitude of dielectric constant (ε') and loss tangent ($tan\delta$) with increase in Bi content. The impedance data shows two semicircles in Nyquist plot within the study temperature indicating the contribution of grain and grain boundary to the total impedance. The variation of imaginary part of impedance and modulus with frequency shows asymmetric peaks and the peak maximum shifts towards higher frequencies with increase in temperature indicating a non-Debye type of relaxation behavior in the investigated system. It is observed that the conductivity decreases with increasing in Bi concentration. The variation of DC conductivity with

temperature follows Arrhenius behavior. The AC conductivity is used to calculate the Fermi level, binding energy and thermal conductivity at different temperature.

Chapter 5 contains the dielectric study of heterovalent Dysprosium (Dy^{+3}) ion substituted $BaZr_{0.25}Ti_{0.75}O_3$ ceramic. The polycrystalline $Ba_{1-x}Dy_{2x/3}Zr_{0.25}Ti_{0.75}O_3$ (x= 0.01, 0.025, 0.05) ceramic has been prepared by solid state reaction route. The samples were found to be well crystallized in single phase. The scanning electron microscopy (SEM) micrographs suggest that materials comprise of polycrystalline microstructure and the concentration of dopant affects the microstructure. The dielectric response indicates relaxor behavior and the magnitude of dielectric constant (ε') and loss tangent ($tan\delta$) decreases rapidly as Dysprosium concentration increases. It is seen that the loss tangent decreases rapidly at high temperature. The second part of the chapter deals with the study of the glassy nature of the ceramics using various theoretical models such as Debye law and Vogel-Fulcher law which provides better understanding of the relaxor behavior. The diffusiveness coefficient and the dielectric dispersion value increases significantly with increase in Dysprosium content. The electrical properties of the samples have been studied by impedance spectroscopy which shows poly-dispersive nature of the samples.

Chapter 6 mainly explains the structural study of Yttrium (Y^{+3}) substitute $BaZr_{0.25}Ti_{0.75}O_3$ ceramic. $[Ba_{1-x}Y_{2x/3}](Zr_{0.25}Ti_{0.75})O_3$ powders with different yttrium concentrations (x =0.01, 0.025 and 0.05) were prepared by solid state reaction. X-Ray Diffraction (XRD) patterns and Fourier Transform Raman Spectroscopy (FT-RS)

show perovskite-type cubic structure without the presence of deleterious phases in all compositions. XRD data indicates a reduction of lattice parameters/unit cell volume and FT-RS spectra shows a disappearance of some Raman active-modes with the increase of yttrium concentration into the lattice. FT-IR spectra exhibited a high absorption band situated in range 536-570 cm^{-1}, which is ascribed to the M-O (M = Ti, Zr and/or Y) antisymmetric stretching vibrations into the lattice. The dielectric study shows relaxor behavior and the dielectric permittivity decreases with increases in yttrium content. The transition temperature increases for 1 atom% of yttrium and decreases for higher concentration of yttrium content. The optical band gap values estimated from the UV-vis spectra suggested the presence of intermediary energy levels (shallow holes) within the band gap. When excited with 350 *nm* wavelength at room temperature, all the powders obtained exhibited broad PL band with a maximum emission in blue region. The electrical properties of the sample have been studied by impedance spectroscopy.

Chapter 7 presents the summary of the research work and major conclusion drawn after in depth discussion in individual chapters. A brief report on the scope for future work is also presented**.**

CHAPTER 1

BACKGROUND AND MOTIVATION

1. Introduction

It is the intent of this chapter to provide a brief description of the phenomena of ferroelectricity and piezoelectricity with an emphasis on dependence of these properties on the microstructure and phase purity of the material.

1.1 Ferroelectricity

The phenomenon of ferroelectricity was discovered by *Valasek (1921)*. There after many essential features of the ferroelectric phenomenon were studied and described. Table 1.1 provides the chronological information on the early ferroelectric crystals. Since then many excellent books introducing the number of phenomenological theories of ferroelectricity and various ferroelectric material systems have been published *(Kanzig (1957), Burfoot (1967), Jaffe et al. (1971), Lines et al. (1977))*. Rochelle salt ($NaKC_4H_4O_6.\ H_2O$) was the first material found to show ferroelectric properties such as re-orientable spontaneous polarization (P_s) on cooling below a transition temperature (T_c - Curie temperature). In the ferroelectric phase,

modifications to cation and anion positions occur to give relative displacements of ions inside the unit cell, resulting in reversible spontaneous dipole moments.

Table 1.1 A partial list of early ferroelectric systems *(Jona et al 1962 and Lines et al 1977)*

Name and Chemical Formula	**Curie Temperature, T_c (^oC)**	**Spontaneous Polarization, Ps ($\mu C/cm^2$)**	**Year in which reported**
Rochelle salt $NaKC_4H_4O_6.H_2O$	23	0.25	1921
Potassium Dihydrogen Phosphate (KDP) KH_2PO_4	-150	4	1935
Potassium Dihydrogen Arsenate KH_2AsO_4	-177	5	1938
Potassium Dideuterium Phosphate KD_2PO_4	-60	5.5	1942
Barium Titanate $BaTiO_3$	120	26	1945
Lead Titanate $PbTiO_3$	490	>50	1950
Potassium Nibonate $KNbO_3$	415	30	1951
Lead Zirconate Titanate (PZT) $Pb(Zr_xTi_{1-x})O_3$	~350	>40	1952

The moment which develops polarization ($\vec{P}$) is equal to $q\frac{\vec{d}}{v}$, where q is the electric charge on the displaced ion, $\vec{d}$ is the relative displacement, and V is the volume of the unit cell. This moment is related to the electric displacement as,

$$\overline{D} = \varepsilon_0 \varepsilon \overline{E} = \varepsilon_0 \overline{E} + \overline{P} \qquad (1.1)$$

where ε_0 and ε are the free space and relative susceptibilities or permittivities, respectively *(Nye 1957).*

One distinctive characteristic of ferroelectrics is the hysteresis loop in the polarization versus electric field curve. A net spontaneous polarization exists even at zero electric field and the loop disappears at the Curie temperature T_c, where the material undergoes a phase transition from high temperature paraelectric to low temperature ferroelectric state.

1.2 Piezoelectricity

All ferroelectric materials are potentially piezoelectric (see Figure 1.1 for crystal classification). Piezoelectricity is the ability of certain crystalline materials to develop an electrical charge proportional to an applied mechanical stress. This is also called the direct piezoelectric effect. Piezoelectric materials also show a converse effect, where a geometric strain (deformation) is produced up on the application of a voltage. The direct and converse piezoelectric effects can be expressed in tensor notation as,

$$\vec{P} = d_{ijk}\sigma_{jk} \qquad (direct\ piezoelectric\ effect) \tag{1.2}$$

$$x_{ij} = d_{kij}E_k \qquad (converse\ piezoelectric\ effect) \tag{1.3}$$

Where, $\vec{P}_i$ is the polarization generated along the i – axis in response to the applied stress σ_{jk}, and d_{ijk} $(= d_{kij})$ is the piezoelectric coefficient. For the converse effect, x_{ij} is the strain generated in a particular orientation of the crystal up on the application of electric field $\vec{E}_k$ along the k – axis.

1.3 Basis for the Ferroelectricity in Crystals

Crystal can be divided into 32 groups. Of the 32 possible crystal classes (i.e. point groups), 11 are Centro symmetric and thus cannot exhibit polar properties. The remaining 21 lack a center of symmetry and thus can posses one or more polar axes. Among these, 20 classes are piezoelectric, the one exception being cubic class (Figure 1.1). Piezoelectric crystals have the property that the application of mechanical stress induces polarization, and conversely, the application of an electric field produces mechanical deformation. Of the 20 piezoelectric classes, 10 have a unique polar axis and thus are spontaneously polarized, i.e. polarized in the absence of an electric field. Crystals belonging to these 10 classes are called pyroelectric. The intrinsic polarization of pyroelectric crystals is often difficult to detect experimentally because of the neutralization of the charges on the crystal surfaces by free charges from the atmosphere and by conduction within the crystal. However, because the polarization is a function of temperature, it is often possible to observe the spontaneous moment in these crystals by changing the temperature, hence the name pyroelectrics. Ferroelectric crystals belong to the pyroelectric family, but they also exhibit the additional property that the direction of the spontaneous polarization can be reversed by the application of an electric field.

Thus, we have the following simple definition for a ferroelectric crystal: "*A ferroelectric crystals is a crystal that possesses reversible spontaneous polarization as exhibited by a dielectric hysteresis loop"*. A more detailed discussion on ferroelectric is given in the subsequent sections.

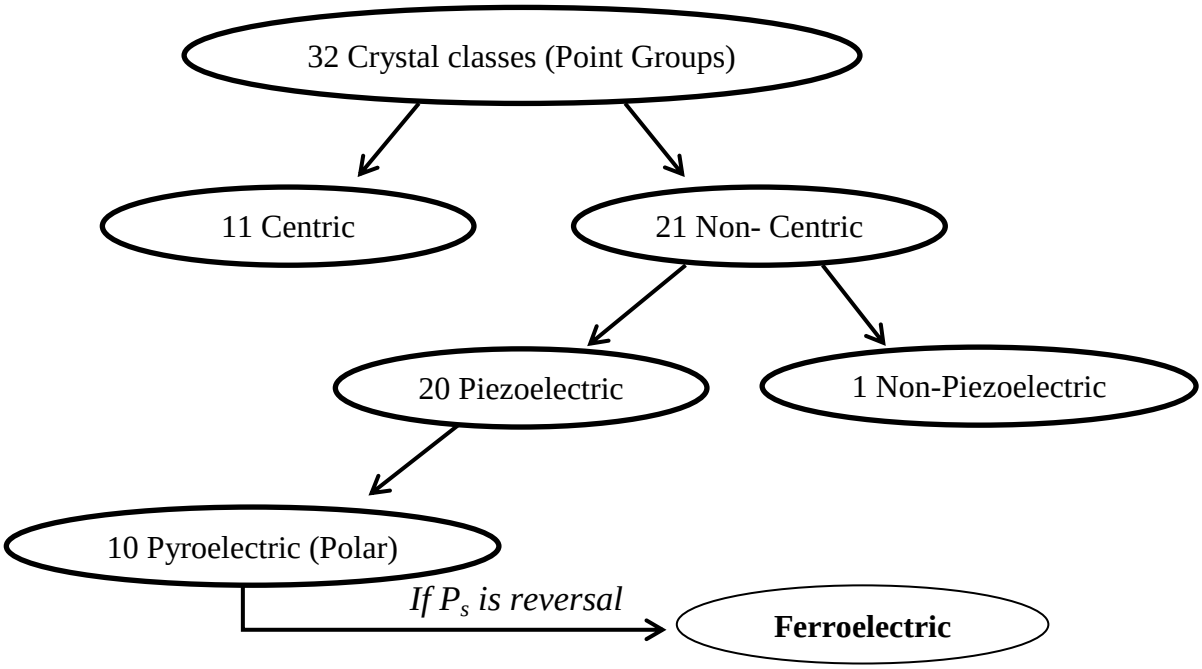

Figure 1.1 A classification scheme for the 32 crystallographic point groups

1.4 Perovskite Crystal Structure

Most of the useful ferroelectrics, such as Barium Titanate (BT), Lead Titanate ($PbTiO_3$), Lead Zirconate Titanate (PZT), Lead Lanthanum Zirconate Titanate (PLZT), and Potassium Niobate ($KNbO_3$), have the perovskite structure. Perovskite is the mineral name of Calcium Titanate ($CaTiO_3$). Its simplest structure is cubic, which is the high temperature form of many mixed oxides of the ABO_3 type.

The simple cubic structure (space symmetry P*m3m*) consists of corner sharing oxygen octahedra (BO_6) arranged in three dimensions with smaller, highly charged cations (B: Ti^{4+}, Zr^{4+}, Sn^{4+}, Nb^{5+}, Ta^{5+}, W^{6+} etc.) located in the middle of the octahedral, and lower charged, larger cations (A: Na^{+}, K^{+}, Ca^{2+}, Ba^{2+}, Pb^{2+} etc.) in between the octahedral. The ABO_3 structure is shown in Figure 1.2. Most perovskite type

ferroelectrics are compounds with either $A^{2+}B^{4+}O_3^{2-}$ or $A^{1+}B^{5+}O_3^{2-}$ type formulation *(Xu 1991)*.

The perovskite structure can be also regarded as a cubic close packed arrangement of large A and O ions with smaller B ions filling the octahedral interstitial positions. The structure is also very tolerant to cation substitution at both A and B sites of lattice, and hence can lead to more complex compounds, such as $(K_{1/2}Bi_{1/2})TiO_3$, $Pb(Fe_{1/2}Ta_{1/2})O_3$, $Pb(Co_{1/4}Mn_{1/4}W_{1/2})O_3$, $Pb(Mg_{1/3}Nb_{2/3})$, and $Pb(Zn_{1/3}Nb_{2/3})O_3$ *(Xu 1991and Cross 1994)*. As will be discussed later, ferroelectricity is mostly observed in certain temperature regions delineated by transition (or Curie temperature, T_C) points above which the crystals are no longer ferroelectric.

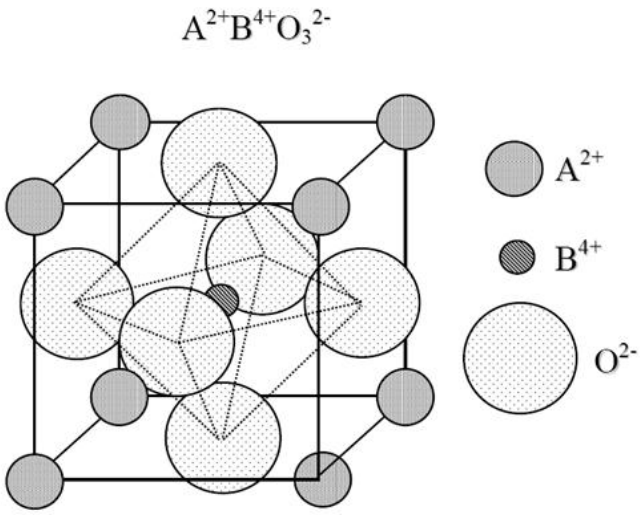

Figure 1.2 A cubic ABO_3, perovskite type unit cell

In 1945, Barium Titanate ($BaTiO_3$), the first ceramic material in which ferroelectric behaviour was observed, *(Wul et al 1945)*. With its much simpler structure (perovskite), better ferroelectric properties, chemical and mechanical stability, Barium Titanate (BT) became one of the most extensively studied ferroelectric materials *(Lines et al 1977)*. $BaTiO_3$ was considered not only as a model system for

ferroelectricity, but also used for practical applications. Added to the chemical and mechanical stability, it exhibits ferroelectric properties at and above room temperature ($\sim 125^{o}C$) and can be easily prepared and used in polycrystalline form *(Jona et al 1962).* By the 1950s the solid solution system $Pb(Zr,Ti)O_3$ (PZT), which also possess the perovskite structure, was found to be ferroelectric. PZT compositions are now the most widely exploited of all piezoelectric ceramics both in research and industry. An up to date brief description of BT and PZT systems can be found in *Jaffe et al (1971)* and *Moulson (1990)*. Although the ideal perovskite structure is cubic, the real structure often deviates from the cubic structure. The degree of distortion in the perovskite materials is determined by the Goldschmidt tolerance factor (t) given as

$$t = \frac{r_a + r_o}{\sqrt{2}(r_b + r_o)} \tag{1.4}$$

where r_a , r_b and r_o are the ionic radii of A, B and O ions respectively. For ideally packed perovskite structure, t is one. In most of the cases, t varies from 0.8 to 1. Under topological and geometrical constraints three structural degrees of freedom of distortion from the ideal perovskite structure are considered to be possible: i) displacement of A-site and B-site cations from the centers of the polyhedra, ii) distortions of the anion octahedra and iii) tilting of the BO_6 octahedra *(Knight 1994; Yang et al 1999)*. The displacement of the cations and the distortion of the octahedra are usually correlated and driven by electronic instability of the metal cations. The John-Teller distortion in KCuF *(Okazaki and Snemune 1961)* and the cation displacement in PbZrO *(Corker et al 1997)* are the typical examples. Octahedral tilting is a more common distortion mechanism that can be realized by tilting the rigid BO_6 octahedra while maintaining their corner sharing connectivity *(Megaw and*

Darlington 1975; Glazer 1972; Glazer 1975). This type of distortion is generally observed when the A-site cation is too small for the cubic BO_6 corner sharing octahedral network.

1.5 Classification of Ferroelectric Crystals

Depending on the temperature variation of dielectric constant or Curie constant C, ferroelectrics (*FE*) can be divided into two groups. In one group, the compounds undergoing order-disorder type transition, have a Curie constant of the order 10^3 while for others which undergoes displacive type transition, it is of the order of 10^5. Initially ferroelectric materials were broadly classified into two categories: (a) soft (KH_2PO_4 - type) and (b) hard ($BaTiO_3$ -type).The phase transition in soft (H-bonded) ferroelectrics is of order disorder type where as in hard ones it is displacive type. The phase transition in soft ferroelectrics involves not only the ordering of the disordered hydrogen atom, but also the deformation of the atomic groups like SO_4^{-2} and PO_4^{-3}. In case of displacive type of transition a small atomic displacement of some of the atoms is mainly responsible for phase transition, which has been found in some of the perovskites. However, the difference between displacive and order-disorder type of transition becomes uncertain when the separation of relevant disorder becomes comparable with the mean thermal amplitude of those atoms. The character of ferroelectrics is represented in terms of the dynamics of phase transition.

1.5.1 Relaxor Ferroelectrics

Relaxor ferroelectrics (RFE) or relaxors, exhibit many properties similar to those of spin and dipolar glasses. Normally relaxor behavior in FE materials results from compositionally induced disorder or frustration. This behavior has been observed and studied most extensively in disordered ABO_3 perovskite ferroelectrics and is also seen in mixed crystals of hydrogen-bonded FEs and AFEs, the so-called protonic glasses. In this section we restrict our comments largely to the ABO_3 oxides. Relaxor ferroelectrics are characterized by a broad maximum in the temperature dependence of the real part of the dielectric permittivity (ε'), a frequency-dependent temperature of the dielectric maximum (T_m) and a strong relaxation dispersion of the permittivity at temperatures around and below T_m. They possess local polarization at temperature above T_m.

In the ABO_3 oxides substituting ions of different sizes, valences, and polarizabilities at both the A and B lattice sites produces dipolar defects and can introduce a sufficiently high degree of disorder so as to break translational symmetry and prevent the formation of a long-range ordered state. Instead, the dipolar motion in such systems freezes into a glass-like state on cooling below a dynamic transition temperature, T_m In these highly polarizable host lattices, the presence of a dipolar impurity on a given site can induce dipoles in a number of adjacent unit cells within a correlation length of that site. We expect the dipolar motion within this correlation length to be correlated, leading to the formation of polar nanodomains. Indeed, such nanodomains have been observed in many ABO_3 relaxors at temperatures far above the peak in $\varepsilon'(T)$, and their occurrence is now considered to be crucial to the understanding of the properties of relaxors. We picture a distribution of sizes of such

nanodomains in which the orientational degrees of freedom are correlated within each domain, but uncorrelated across the various domains. At sufficiently low temperatures, the dipolar motion within each domain freezes, resulting in the formation of an orientational glass (relaxor) state. Such a state is characterized by a distribution of relaxation times related to the sizes of the nanodomains. Two important characteristics of this relaxor state that distinguish it from simple dipolar glasses or spin glasses are the predominant existence of the dipolar nanodomains (vs. largely individual dipoles or spins) and the presence of some degree of cooperative freezing of the orientational degrees of freedom. Evidence of this cooperative effect comes from the observation of some remanent polarization in electric field hysteresis loops. It should be noted, however, that such evidence is also seen in systems of random dipoles in low polarizability hosts for doped alkali halides with sufficiently high concentration of dipoles. In order to appreciate and understand the properties of relaxors, it is useful to contrast some of their properties with those of normal ferroelectrics. We do so with the help of Figure 1.3 The contrast is as follows, The P-E hysteresis loop is the signature of a ferroelectric in the low temperature ferroelectric (FE) phase. The large remanent polarization, P_R, is a manifestation of the cooperative nature of the ferroelectric FE phenomenon. A relaxor, on the other hand, exhibits a so-called slim-loop. For sufficiently high electric fields the nanodomains of the relaxor can be oriented with the field leading to large polarization; however, on removing the field most of these domains reacquire their random orientations resulting in a small P_R. The small P_R is evidence for the presence of some degree of cooperative freezing of dipolar (or nanodomain) orientations.

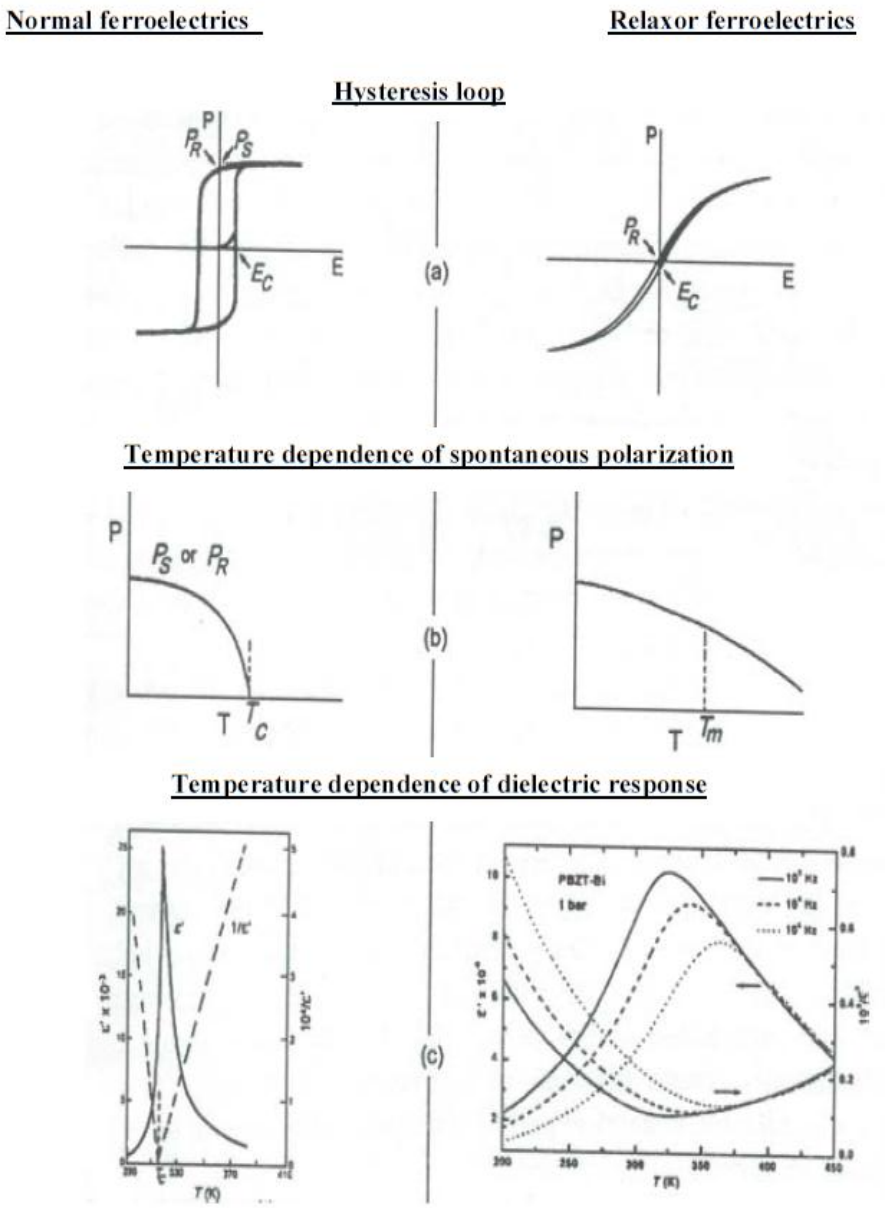

Figure 1.3 Contrast between the properties of normal ferroelectrics and relaxor ferroelectrics or relaxors

The saturation and remanent polarizations of a ferroelectric decrease with increasing temperature and vanish at the FE transition temperature (T_c). The vanishing of P at T_c is continuous for a second-order phase transition and discontinuous for a first-order transition. No polar domains exist above T_c. By contrast, the field induced polarization of a relaxor decreases smoothly through the

dynamic transition temperature T_m and retains finite values to rather high temperatures due to the fact that nano-size domains persist to well above T_m.

The static dielectric susceptibility or dielectric constant (ε'), of a ferroelectric exhibits a sharp, narrow peak at T_c. For a single crystal the peak is very sharp and the width at half max is ~10-20 *K*. For a mixed oxide ferroelectric, e.g., PZT, the peak is somewhat rounded due to compositional fluctuations, and the width at half max is typically ~20-40 *K*. The ferroelectric response is frequency independent in the audio frequency range.

By contrast, a relaxor exhibits a very broad $\varepsilon'(T)$ peak and strong frequency dispersion in the peak temperature (T_m) and in the magnitude of ε' below T_m. The conventional wisdom has been that the broad $\varepsilon'(T)$ peak, also referred to as a "diffuse phase transition," is associated with compositional fluctuations leading to many micro FE regions with different compositions and T_c' s. The breadth of the peak is simply a manifestation of the dipolar glass-like response of these materials. The temperature dependence of ε' of a ferroelectric obeys a Curie-Weiss law,

$$\varepsilon = \frac{c}{T - Tc} \tag{1.5}$$

above, T_c could be shown by the linear $1/\varepsilon'$ vs. T response. By contrast $\varepsilon'(T)$ of a relaxor exhibits strong deviation from this law for temperatures of many 10s to a few 100s degrees above T_m.

1.5.2 Diffuse Phase Transition

Many phase transitions in macroscopic homogeneous materials are characterized by the fact that the transition temperature is not sharply defined. In these, so-called diffuse phase transition temperature (DPT), the transition is smeared out over a certain temperature interval, resulting in a gradual change of physical properties in this temperature region. Though this phenomenon is observed in several types of materials, however, the most remarkable examples of DPT are found in ferroelectric materials. Ferroelectrics diffuse phase transitions (FDPT) are first mentioned in the literature in the early 1950's (*Kanzig, 1951*). Some characteristics of the DPT are: (a) broadened maxima in the permittivity- temperature curve, (b) gradual decrease of spontaneous and remanent polarizations with rising temperature, (c) transition temperatures obtained by different techniques which do not coincide, (d) relaxation character of the dielectric properties in transition region and (e) no Curie-Weiss behavior in certain temperature intervals above the transition temperature. The diffuseness of the phase transition is assumed to be due to the occurrence of fluctuations in a relatively large temperature interval around the transition. Usually two kinds of fluctuations are considered: (a) compositional fluctuation and (b) polarization (structural) fluctuation. From the thermodynamic point of view, it is clear that the compositional fluctuation is present in ferroelectric solids-solutions and polarization fluctuation is due to the small energy difference between high and low temperature phases around the transition. This small entropy difference between ferroelectric and paraelectric phase will cause a large probability of fluctuation. *Kanzing (1951)* has observed from X-ray diffraction that in a narrow temperature range around the transition $BaTiO_3$ single crystal splits up into FE and

PE micro regions. According to *Fritsberg (1977)* substances of less stability are expected to have a more diffuse transition. For relaxor as well as other FDPT the width of the transition region is mainly important for practical applications. *Smolensky (1970)* and *Rolov (1965)* have introduced a model calculation, based on the concept of Gaussian distribution for both the compositional and polarization fluctuation, from which the diffuseness parameter can be calculated.

Complex perovskite type ferroelectrics with distorted cation arrangements show DPT which is characterized by a broad maximum for the temperature dependence of dielectric constant (ε') and dielectric dispersion in the transition region *(Smolensky, 1984)*. For DPT ε' follows modified temperature dependence.

$$\frac{1}{\varepsilon'} - \frac{1}{\varepsilon_m} = (T - T_m)^{\gamma} / C' \tag{1.6}$$

where T_m is the temperature at which ε reaches maximum, ε_m is the value of ε' at T_m, C' is the modified Curie Weiss like constant and: is the critical exponent, explains the diffusivity of the materials, which lies in the range *1< γ<2 (Tiwari 1994)*. The smeared out ε' vs T response has generally been attributed *(Kirillov and V.A. Isupov, 1973)* to the presence of micro regions with local compositions varying from the average composition over length scale of 100 to 1000 $\AA$. Different micro regions in a macroscopic sample are assumed to transfer at different temperature, so-called Curie range, leading DPT which is due to compositional fluctuations *(Cross, 1987).* The dielectric and mechanical properties of FE system below their T_C are functions of the state of polarization and stress. So ferroelectrics have major application today because of their characteristic electro-optic, dielectric and hysteresis properties. For many practical applications, it is desired to use the very large property maxima in the

vicinity of the ferroelectric phase transition, to move the transition into the temperature range of interest and to broaden and diffuse the very large sharp peak values. In DPT the dielectric maxima is now much rounder and polarization persists for a short range of temperature above T_m.

1.5.3 Theoretical models to explain relaxor behaviour

The relaxor behavior in normal ferroelectric materials results from compositionally induced disorder or frustration. In the ABO_3 oxides, substitution of ions of different sizes, valencies, electronegativities and polarizabilities at both the A and B lattice sites produces dipolar defects and introduces a sufficiently high degree of disorder so as to break translational symmetry and prevent the formation of a long range ordered state *(Dai et al 1993; Dai et al 1996)*. In reflecting on the occurrence of relaxor behavior in perovskites, there appear to be three essential ingredients: the existence of lattice disorder *(Priya and Viehland 2002; Lu 2004)*, evidence for the existence of polar nanodomains at temperatures much higher than T_m and these domains existing as islands in a highly polarizable (soft-mode) host lattice *(Gupta and Viehland 1996)*. The existence of nano polar regions has also been evidenced by several other experimental techniques such as transmission electron microscopy *(Randall and Bhalla 1989)*, diffuse x-ray scattering and neutron diffraction studies *(de Mathan, 1991; Conlon et al 2004; Gehring et al 2004; Xu et al 2004)*. Various physical models such as super paraelectric model, order-disorder transition model, microdomain and macrodomain switching model, dipolar glass model and random field model have been proposed to explain the behavior of Relaxor Ferroelectric Electrics (RFEs). *Smolenskii (1959)* proposed that the responsible factor for the

relaxor behavior in PMN was compositional fluctuation due to the randomness in the B-site. The compositional fluctuation leads to the fluctuation in local field component resulting a distribution of transition temperatures. This simple model has been widely cited, but it failed to explain the RFE behavior in the systems without any compositional fluctuation. *Burns and Dacol (1983)* proposed that the polar regions (regions with a net dipole moment) start appearing at a temperature much higher than T_m, named as Burn temperature (T_B). They have observed a deviation from the linear response of refractive index with temperature which attributed to the nucleation of dipolar nanoregions at T_B. The T_B was found to be very much close to the temperature at which the classical Curie-Weiss law begins to deviate. The dielectric behavior of RFEs at temperatures lower than T_B is mainly dependent on the concentration and dipole moment of the polar regions.

Cross (1987) proposed in his superparaelectric model that the relaxors possess polar micro regions that are dynamically disordered above T_m. The cations continuously flip between equivalent directions when activated by thermal energy. The heterogeneity caused by the mixed B-site creates locally favorable directions. Therefore, the local symmetry is different from the global symmetry. However, the energy barrier separating the different directions is so small that the polar domains do not extend to a larger size as in normal ferroelectrics. The relaxation mechanism involved in RFEs seems to be deviating from Debye type. *Viehland et al (1990, 1991)* proposed a glassy polarization behavior for RFEs and successfully explained the frequency dependence of T_m in $0.9PMN$-$0.1PT$ using the Vogel-Fulcher relation (V-F law). Later, many authors confirm that the polar clusters in the RFEs freeze at low temperature similar to the dipolar glasses. *Bell (1993)*, explained the dielectric

behavior based on ideal super-paraelectric by considering an ensemble of independent, identical, nano-sized super-paraelectric clusters, with a distribution in the size of the clusters. Taking the temperature dependent of cluster sizes and interactions into consideration, the calculations are carried out employing Landau-Ginsberg-Devonshire formalism to determine the dielectric function of clusters. *Glazounov et al (1995)* introduced the possibility of distribution of local transition temperatures of the polar regions. The model considers the relaxors as an ensemble of non-interacting polar regions with unique size. It could explain the static polarization and the real part of permittivity to some extent but fails to explain the imaginary part of permittivity and the relaxation time phenomena. This suggests that there exists a distribution of size of the polar regions in RFEs. *Lu and Calvarin (1995)* assumed an exponential distribution of the size of polar regions. The model predicts that the dielectric absorption always increases with increasing frequency, which contradicts the experimental results in the low-temperature range. *Cheng et al (1996, 1997,1998)* proposed a power law to explain the relation between T_m and frequency. To explain the behavior of polar clusters, they have also proposed a model in which the relation between the frequency and dielectric constant at temperatures much lower and higher than T_m can be expressed by two exponential functions. The analysis at high temperature gives the information about the production rate and the concentration of polar clusters whereas the analysis at low temperature range gives an idea about the freezing of polar clusters. *Glazounov and Tagantsev (2000)* proposed a phenomenological model, which describes frequency dispersion of nonlinear dielectric response of RFEs as a result of dispersion of their linear dielectric permittivity. It provided a good qualitative description of temperature and frequency dependence of the third harmonics of PMN.

Kleemann (2006) reported that the substitutional charge disorder giving rise to quenched electric random-fields is probably the origin of the peculiar behavior of relaxor ferroelectrics. Spatial fluctuations of the RFs correlate the dipolar fluctuations and give rise to polar nanoregions in the paraelectric regime evidenced by piezoresponse force microscopy at the nanoscale. Frustrated interaction between the polar nanoregions in cubic relaxors gives rise to cluster glass states as evidenced by strong pressure dependence, typical dipolar slowing-down and theoretically treated within a spherical random bond-RF model. On the other hand, freezing into a domain state takes place in uniaxial relaxors. *Samara and Venturini (2006)* reported the influence of hydrostatic pressure on the dielectric properties of compositionally disordered ABO_3 perovskites has been the discovery of a pressure-induced FE to RFE crossover making the RFE state, the ground state, of these materials at reduced volume. They have observed that the pressure favors the RFE state and biasing fields favor the FE state. The combined results provide new insights into the physics and can be explained in terms of changes in the correlation length for dipolar interaction among the polar nano-regions (PNRs) that exist in these disordered materials.

1.6 Review of previous work

The properties of $BaTiO_3$ can be significantly modified by substitution at either or both of the cationic sites by other metal ions of suitable valency and ionic size. This facilitates the tailoring of functional properties of $BaTiO_3$ suitable for practical applications. Such ferroelectric and piezoelectric applications as sensors, actuators and memory devices require a material having good piezoelectric constants along with high remanent polarization and low coercive field parameters. However, barium titanate ceramic suffers from two main disadvantages: firstly it has a tetragonal to orthorhombic transition below room temperature ($\sim 5^{o}C$) and secondly in the tetragonal phase the resonant frequency rises rapidly with temperature. This necessitated the need to look for alternate materials with suitable properties. Most ceramic formulations require a Curie point shifter, a material that forms a solid solution with $BaTiO_3$ and alters the lattice so that the phase change and therefore the permittivity maximum occurs at a more appropriate temperature. This is commonly done by substitution of isovalent cations for Ti^{4+} and/or Ba^{2+}; that is to say, by the addition of materials such as $BaZrO_3$, $SrZrO_3$, $SrTiO_3$ or $CaZrO_3$.

For capacitor, sensor, actuator and memory device applications besides a high permittivity, other decisive factors that are required are a fast dielectric response, low leakage currents and a long life time under dc voltage stress. In alkaline earth titanate bulk ceramics, the dominant mechanism causing resistance degradation is the motion of oxygen vacancies to the cathode of the capacitor structure, giving rise to induced enhancement of the electronic carrier concentrations which increase the conductivity and limits the lifetime of the capacitor. Investigations on the Zr^{4+} substituted $BaTiO_3$ ceramics show that in comparison to alkaline earth titanates the

zirconates are more stable with respect to temperature and degradation. Also, in the $Ba(Zr_xTi_{1-x})O_3$ system the tetragonal to cubic phase transition temperature can be shifted to lower values by increasing the Zr content. Therefore, $Ba(Zr_xTi_{1-x})O_3$ ceramics have great potential for functional device applications. The early work on the $Ba(Zr_xTi_{1-x})O_3$ ceramics to a great extent was done by Russian researchers. *McQuarrie et al (1954)* initially reported the complete solid solution formation of $BaTiO_3$ and $BaZrO_3$. *Kell et al (1956)* had investigated the structural transitions in $BaTiO_3$ – $BaZrO_3$ system and constructed a compositional phase diagram between $BaTiO_3$ and $BaZrO_3$. He also reported the effect of increasing Zr content on the electrical properties and stated that 5 mol% Zr substituted $BaTiO_3$ has the maximum dielectric constant at the phase transition temperature (T_C $\sim 105^oC$). Later, *Verbitskaia et al (1958)* carried out detailed X-ray diffraction and electrical property study to investigate the effect of increasing Zr content on the structural parameters and nature of phase transitions. They also refined the compositional phase diagram constructed by *Kell et al (1956)* clearly defining the shifting of lower and higher phase transition temperatures in $BaTiO_3$ with increasing Zr content substitution at the Ti site. Until early 1980s, no reported literature is available on the materials based on this compound. The next report was available in 1982 by *D. Hennings et al (1982)*, in which the detailed structural and phase transition details in $Ba(Zr_xTi_{1-x})O_3$ ceramics prepared using solid state mixed route with 1% excess TiO_2 as sintering aid were described. It was shown that the coexistence of ferroelectric and paraelectric phase is the main reason for the diffused nature of phase transitions in $BaZr_xTi_{1-x}O_3$ ceramics with higher Zr content. Chemical inhomogeneity and internal stresses in microstructure could also be the reasons for diffused phase transition behaviour in $Ba(Zr_xTi_{1-x})O_3$ ceramics. *Neirman (1988)* studied the dependence of sintering

conditions on the Curie temperature in $Ba(Zr_xTi_{1-x})O_3$ ceramics prepared by hydrothermal $Ba(Zr_xTi_{1-x})O_3$ powders and by a mixture of $BaTiO_3$ and $BaZrO_3$. He found that the ceramics prepared from the mixture of $BaTiO_3$ and $BaZrO_3$ showed larger dependence of Curie temperature on sintering conditions whereas the ceramics prepared from hydrothermal powders showed minimum dependence. He also reported that the shift in Curie temperature is not linear with increase in Zr content in chemically homogeneous $Ba(Zr_xTi_{1-x})O_3$ ceramics. *Kazaoui et al (1993)* studied the dependence of relaxor properties on chemical homogeneity and microstructure in $BaZr_{0.2}Ti_{0.8}O_3$ ceramics prepared by sol-gel route and solid state mixed oxide route and found that dielectric relaxation occurs at 10^8 *Hz* near the phase transition temperature. *Dobal et al (2001)* studied the phase transition behaviour using dielectric and Raman scattering techniques in $Ba(Zr_xTi_{1-x})O_3$ ceramics and found excellent agreement between both the techniques on crystallographic phase transition temperatures. *Sciau et al (2000)* investigated the influence of electric field on the relaxor behaviour with the support of X-ray diffraction studies in $BaZr_{0.35}Ti_{0.65}O_3$ and $Ba_{0.92}Ca_{0.08}Ti_{0.75}Zr_{0.25}O_3$ and found that $BaZr_{0.35}Ti_{0.65}O_3$ has the relaxor behaviour typical of $PbMg_{1/3}Nb_{2/3}O_3$. *Chazono et al (2000)* studied the influence of firing conditions and microstructure on the dielectric behaviour in $Ba(Zr_xTi_{1-x})O_3$ ceramics with Ni multilayer capacitor structure and found that the ceramic fired in reducing atmosphere has two dielectric relaxation features and the ceramic fired in weak oxidizing atmosphere has one dielectric relaxation feature and less degree of variation in dielectric permittivity. The ferroelectric relaxor behaviour in $BaZr_{0.3}Ti_{0.7}O_3$ ceramics was reported by *Yu et al (2002)* and he found that the relaxation rate followed the Vogel – Fulcher relation. *Tang et al (2004)* studied the $Ba(Zr_xTi_{1-x})O_3$ ceramics with 20 mol% to 35 mol% Zr

content and found that as the Zr content is increased, the diffusive nature of the phase transition increased suggesting the composition related diffusive nature of the phase transition. They observed the relaxor ferroelectric nature in $Ba(Zr_xTi_{1-x})O_3$ ceramics with Zr content more than 25 mol% and the tenability and the figure of merit for these compositions is high. *Tang et al (2004)* investigated the effect of grain size on the dielectric and tunable properties of $Ba(Zr_xTi_{1-x})O_3$ ceramics, with 20 mol% Zr, derived from sol-gel prepared $Ba(Zr_xTi_{1-x})O_3$ powders and found that with increasing grain size dielectric constant and Curie temperature were found to decrease. They also reported that with decreasing grain size the ceramic showed relaxor ferroelectric behavior.

Substitution and doping of trivalent ions in $BaTiO_3$ is widely studied and many reports are available on the structural behaviour and dielectric properties of rare earth ion doped $BaTiO_3$. Many defect mechanisms were proposed for the charge compensation because of the doping of trivalent ions. The simultaneous substitution of isovalent and aliovalent ions in the $BaTiO_3$ is not widely studied and very few reports are available. *Buscaglia et al (2000)* studied the influence of foreign ions (Cr, Co, Fe, Ni, Y, Er, Tb, Gd, Pr and La) on the crystal structure of $BaTiO_3$. *Hiroshi Kishi et al (1999)* studied the effect of rare earth ions on the microstructure of the $BaTiO_3$ and found that La^{3+} and Pr^{3+} have A site preference, Tb^{3+} and Gd^{3+} substitute partially at the B site and Er^{3+} and Y^{3+} have B site preference in $BaTiO_3$. *Makovec et al (1995)* and *Morrison et al. (1999)* investigated the influence of La^{3+} doping on the structural and dielectric properties in $BaTiO_3$. Yttrium site occupancy in $BaTiO_3$ was studied by *Lin et al. (2002)* and *Jing Zhi et al. (1999)* and both reported that Y^{3+} can substitute for either A site or B site. *Jin Hyun et al (2001)* studied the dielectric

properties of erbium doped $BaTiO_3$ and found that up to 2 mol% Er, no change in the Curie temperature was observed. However, above 3 mol% the Curie temperature is lowered along with the appearance of a secondary phase, namely, $Er_2Ti_2O_7$. *Pu et al (2005)* investigated the microstructure and dielectric properties of dysprosium doped $BaTiO_3$ and found that 0.75 mol% Dy^{3+} substitutions refines the grain size of the ceramic and showed a room temperature dielectric constant of 4100. *Wang et al (2002)* studied the dielectric and ferroelectric behaviour of the ytterbium doped $Ba(Zr_xTi_{1-x})O_3$ ceramic. They found that Yb doping reduced the Curie temperature, dielectric constant maximum is enhanced and the phase transition is broadened. They also found that Yb site occupancy preference shifted from B-site to A-site with increasing Yb content. Recently *Reddy et al (2009)* study the effect of La in $BaZr_{0.1}Ti_{0.9}O_3$ and found that 2 mol% substitution of La increase the dielectric permittivity. The substitution of La, Nd, and Pr $Ba_{1-y}Ln_{2y/3}Zr_{0.2}Ti_{0.8}O_3$, (Ln = La, Pr, Nd)] was studied by *Ostos et al (2009)* and found that the dielectric permittivity increases and the transition temperature decreases with increase in rare earth content. *Shan et al (2007)* studied the yttrium doping on $Ba(Zr_xTi_{1-x})O_3$ ceramics and found that the transition temperature increases with 6 weight% doping of Yttrium. It is clear from the above reported literature that, there are not much report avaialable on the heterovalent ion substitution in $Ba(Zr_xTi_{1-x})O_3$ ceramics. This work, therefore, is an attempt to prepare $Ba(Zr_xTi_{1-x})O_3$ (5 mol% ≤ Zr ≤ 30 mol%) ceramics solid state mixed oxide route and study microstructure and functional properties by making systematic comparison of the electrical and optical properties of heterovalent ion substituted $BaZr_{0.25}Ti_{0.75}O_3$ ceramics.

1.7 Objective and Motivation

$BaZr_xTi_{1-x}O_3$ (BZT) ceramics are interesting materials for being used as dielectrics in commercial capacitor applications. They present high dielectric constant, high voltage resistance, composition- dependent Curie temperature and exhibit better temperature stability in the paraelectric state *(Yu et al 2007; Ciomaga et al 2007; Zhai et al 2006)*. In the present study the parent composition $BaZr_{0.25}Ti_{0.75}O_3$ is chosen due to its relaxor behavior, high dielectric constant at room temperature and the transition temperature closed to room temperature.

Impurity-doping in $BaZr_xTi_{1-x}O_3$ electroceramics has become also a common way to improve the material performance *(Shan et al 2007; Wang et al 2002; Lee et al 2001)*. Heterovalent ions are known to exhibit useful functions, of stabilizing the temperature dependence of relative dielectric constant and lowering the dissipation factor in dielectric ceramics. Small heterovalent ions will occupy the B-site and large ones the A-site, whereas the intermediate ions will occupy both sites with different partitioning for each ion due to the local strain is similar in both A-site and B-sites. The heterovalent ions are known to act as a donor when they dissolve in A-site and an acceptor in B-site. Nevertheless, reported works related to the A-site vacancy defect compensation model on rare-earth doped $BaZr_xTi_{1-x}O_3$ ceramics are even scarcely investigated.

The aim of the present work is to trigger the coexistence between order (ferroelectric) and disorder (relaxor) by adding another degree of freedom on introducing a disorder on the A (Ba) site. This can be achieved by heterovalent substitutions in the 12-C.N. crystallographic site (Ba^{+2} cations) with trivalent ion in $Ba(Ti_{0.75}Zr_{0.25})O_3$. The choice of this composition is due to its relaxor behavior and

the T_m is close to room temperature. The $Ba_{1-x}Ln_{2x/3}(Ti_{0.75}Zr_{0.25})O_3$ (Ln = Bi, Dy, Y) compositions are then investigated to observe the influence on the structural, microstructural, electrical and optical study of heterovalent substitutions (in the *A*-site) of $Ba(Ti_{0.75}Zr_{0.25})O_3$.

In this context the main purpose of this research is to synthesis and characterization of A-site deficient rare-earth doped $BaZr_{0.25}Ti_{0.75}O_3$ (BZT) with different concentration of heterovalent ions in $(Ba_{1-y}Ln_{2y/3})Zr_{0.25}Ti_{0.75}O_3$ system (Ln=Bi, Y, Dy).

Several experimental techniques such as X-Ray Diffraction (XRD), Scanning Electron Microscopy (SEM), Energy Dispersive X-ray spectrum, Dielectric spectroscopy, Impedance spectroscopy, Raman spectroscopy, Ultraviolet-visible absorption spectroscopy analysis and Photoluminescence analysis have been employed to characterize the solid solution ceramics.

CHAPTER 2

EXPERIMENTAL TECHNIQUES

In this chapter, the synthesis of the compounds selected for present work and the experimental techniques employed to characterize the specimens, are briefly discussed.

2.1 Synthesis

Ceramic materials are one of the major groups in the Materials Science because of their direct and indirect applications in day today life. Hence the synthesis of new ceramic powders is of great importance in the progress of Materials Science. There are several methods of preparation such as mechanical method, which includes solid-state reaction, and ball milling etc., and the chemical method, which includes sol-gel, wet-dry and polymer-sol-gel etc. To achieve a quality product with respect to purity, homogeneity, reactivity, particle size etc., each method finds its own advantages and disadvantages. In this contest, the solid-state reaction found to be the easier, convenient and low cost technique among other available methods by means of performance, reliability, reproducibility and economy.

2.1.1 Solid state reaction

The various steps in solid-state reaction process are represented as a flow chart shown in Figure 2.1. In the present work, raw chemicals with high purity are used for the material preparation. The constituents of the required specimen are taken in a stoichiometric ratio and dry mixed followed by wet mixing with distilled water as medium. The mixing is accomplished using agate mortar and pestle. The amount of water used is just enough to form slurry to prevent the selective sedimentation of the reagents.

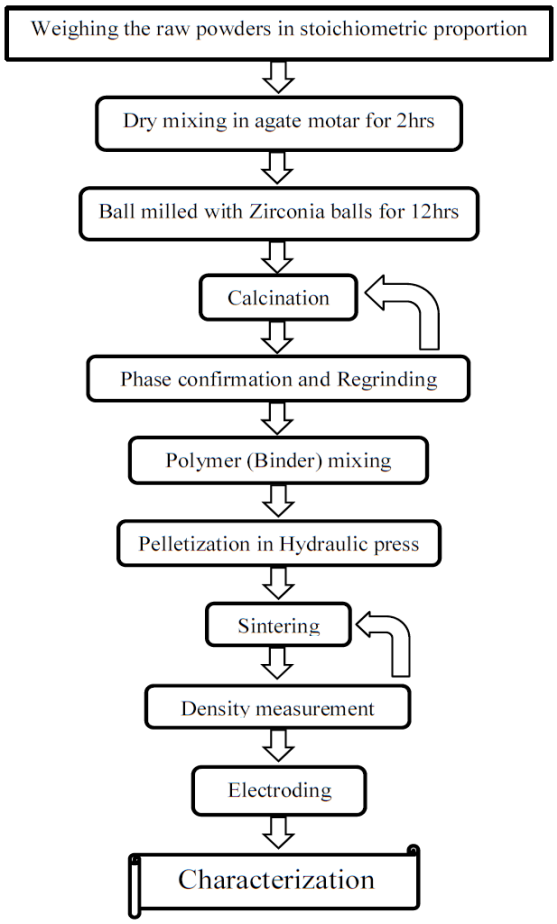

Figure 2.1 Flow chart of sample preparation

After proper mixing, mixed powders were calcined at different temperatures (detailed heat treatments are cited in the text) by an indigenous programmable

furnace with intermediate grinding to avoid agglomeration of the particles. The calcined powders were used for the study of their phase formation as well as their reaction mechanism. After study the phase formation, the powders are again ground and are mixed with poly vinyl alcohol (PVA) (which acts as a binder) to reduce the brittleness, and to have better compactness amongst the granules of the materials. To get uniform and fined grain, the granules were passed through a 73μm sieve. The residues after sieving were again crushed in an agate mortar and passed through the sieve. The process was repeated till all the granules became less than 73μm. The green pellets of dimension 10 *mm* diameter and 1 *mm* thickness are made using uniaxial press with the help of tungsten carbide dye.

2.2 Characterization

The following characterizing tools are used to study the structural, electrical and optical study of the ceramics.

2.2.1 X-Ray Diffraction Study

X-Ray Diffraction (XRD) technique is a powerful tool for material characterization as well as for detailed structural elucidation. As the physical properties of solids (e. g., electrical, optical, magnetic, ferroelectric, etc.) depend on atomic arrangements of materials, determination of the crystal structure is an indispensable part of the characterization of materials, mainly the identification of the chemical species. X-Ray Diffraction patterns are used to establish the atomic arrangement or structure of the materials because the d spacing of diffraction planes is of the order of X-Ray wavelength λ, the various orders n of reflection occur only at the precise values of

angle θ, which satisfies the Bragg equation given by $n\lambda = 2dsin\theta$. The powder profile of a substance, even without further interpretation, can be used for identification of materials.

The accurate determination of lattice parameters provides an important basis in understanding various properties of the materials. The calculation of lattice constants from the line positions or d spacing can be done from a general formula:

$$\frac{1}{d_{hkl}^2} = V^2[h^2b^2c^2sin^2\alpha + k^2c^2a^2sin^2\beta + l^2a^2b^2sin^2\gamma \quad (2.1)$$

where; V = volume of the unit cell

$$= abc(1 - cos^2\alpha - cos^2\beta - cos^2\gamma + cos\alpha\, cos\beta\, cos\gamma)^{1/2} \quad (2.2)$$

where a, b, c, α, β and γ are lattice parameters and h, k, l are the Miller indices. Using the above formula lattice parameters for all the compositions were found out. The kinematics theory of X-Ray diffraction describes that for a perfect cause the spread in the intensity distribution curves, the nature and extent of the intensity spread is an obvious measure of crystal imperfection present in the sample under study. Since the different types of defects may be co-existent in crystalline materials, the problems that arise are of separation of different types of defects and identification and quantitative estimation of the extent and distribution of each type of defects. The different factors affecting the diffraction intensities can be grouped into a single expression for use in calculating the relative intensities of reflections. For powder method, the intensity is

$$I = J\frac{1+cos^2\,2\theta}{4\,sin^2\theta cos\,\theta}F^2A(\theta) \quad (2.3)$$

where *J* is multiplicity factor, and *F* is structure factor, which can be written as

$$F = \sum_i \ f_j \exp 2\pi i(hx_i + ky_i + lz_j) \qquad (2.4)$$

where f_j = atomic scattering factor and A = absorption coefficient $= \frac{1}{v}\int e^{-\mu x}$ where μ is the linear absorption coefficient of the specimen, x is the distance traversed by the beam and v is the volume of the crystal exposed in X-Rays. A very important aspect of the intensity distribution among the reflections is to relate the extinction, which is a deciding factor for the symmetry elements involved in the material. The translations involved in these symmetry elements and centered lattices add a new periodicity in the patterns, which shows itself by extinguishing certain classes of X-Ray spectra. Each type of extinction is characteristic of a particular space group. Therefore, the absence of such characteristic spectra from the diffraction data is a major criterion for the determination of the lattice type and the space group. The following information can be obtained from their X-Ray powder diffractogram

(i) Quality and confirmation of the prepared samples,

(ii) The interplanar spacing *d* of the reflections,

(iii) The intensities of the reflections, and

(iv) The unit cell dimensions and lattice type.

In the present case, calcined powders were characterized with respect to phase identification, phase quantity measurement, crystallite size determination and lattice parameter measurement, etc., all by using Cu-K_α XRD (X-pert MPD, Philips, UK). For quantitative estimation of phases, calcined powders were uniformly mixed and the resulting mixture was analyzed using a step size of 2^o / *min*. The relative

weight fractions were quantified from the ratio of peak areas. The phases giving maximum peak area at a particular temperature were considered as 100% formation of those phases at that temperature. Considering that area as 100%, the relative percentages of the respective phases were calculated. On the basis of XRD line broadening at half maxima of the 100% RI peak, crystallite sizes of the phases were estimated using the Scherer equation, as $P=k\lambda / \beta_{1/2}Cos\theta_p$, where P-linear particle size, $k\lambda$-0.89, θ_p-peak position and $\beta_{1/2}$-half peak width.

2.2.2 Rietveld Refinement analysis

The Rietveld refinement is a method in which the profile intensities obtained from step-scanning measurements of the ceramics allow to estimate an approximate structural model *(Rietveld 1969)*. There is a simple relationship between the individual scale factor determined, considering all refined structural parameters of individual phases of a multiphase sample, and the phase concentration (volume/weight fraction) in the mixture. The structure refinement along with size-strain broadening analysis was carried out simultaneously by adopting the standard procedure. Particle size and lattice strain values of all the phases are found to be isotropic. The process of successive profile refinements modulates different structural and microstructural parameters of the simulated pattern to fit the experimental diffraction pattern. Refinement continues till convergence is reached with the value of the quality factor.

Initially, the positions of the peaks were corrected by successive refinements of systematic errors taking into account the zero-shift error and sample displacement

error. The *U*, *V*, *W* parameters of instrumental broadening, instrumental asymmetry and Gaussianity of reflections were estimated for the present setting of the instrument using a specially prepared Si standard and found to vary with scattering angle in different manners. Structure and microstructure refinements were carried out simultaneously by refining, scale factors, lattice parameters, occupancy factors, variable fractional atomic coordinates, Particle size, r.m.s. lattice strain, preferred orientation factors, etc. of individual phases. Considering the integrated intensity of the peaks as a function of structure/microstructure parameters only, the Marquardt least-squares procedures were adopted for minimizing the difference between the observed and simulated powder diffraction patterns. The minimization was carried out by using the reliability index parameter, R_{wp} (weighted residual error) and R_B (Bragg factor) given by

$$R_{wp} = \left[\frac{\Sigma_i w_i (I_o - I_c)^2}{\Sigma_i w_i I_o^2}\right]^{1/2} \tag{2.5}$$

$$R_B = 100\ \frac{\Sigma |I_o - I_c|}{\Sigma I_o} \tag{2.6}$$

$$R_{exp} = \left[\frac{N-P}{\Sigma_i w_i I_o^2}\right]^{1/2} \tag{2.7}$$

$$GoF = \frac{R_{wp}}{R_{exp}} \tag{2.8}$$

The weight fraction (W_i) for each phase was obtained from the refinement relation,

$$W_i = \frac{S_i (ZMV)_i}{\Sigma_j S_j (ZMV)_j} \tag{2.9}$$

where *i* is the value of *j* for a particular phase among the *N* phases present, S_j is the refined scale factor, *Z* is the number of formula units per cell, *M* is the atomic weight

of the formula unit and V is the volume of the unit cell. The goodness of fit (GoF) is established by comparing R_{wp} with the expected error, R_{exp}. The weight fraction (W_i) for each phase was obtained from the refinement relation.

In our work, the Rietveld refinement was performed through the GSAS program *(Larson et al 2004).* In the Rietveld analysis, the refined parameters were scale factor, background, shift lattice constants, profile half-width parameters (u, v, w), isotropic thermal parameters, strain anisotropy factor, occupancy, atomic functional positions, bond lengths and bond angles. The background was corrected using a Chebyschev polynomial of the first kind. The diffraction peak profiles were better fitted by the Thompson-Cox-Hastings pseudo-Voigt (pV-TCH) function and by the asymmetry function described by *Finger et al (1994)*. The strain anisotropy was corrected by the phenomenological model described by *Stephens et al (1999)*.

2.2.3 Sintering

Density of the electronic ceramic is a very sensitive parameter and that directly affects their properties. Therefore, proper sintering of the pallets is essential for electrical measurement. All the pellets were taken on an alumina plate and sintered at different temperature in a programmable furnace at a heating rate of 5^oC per minute with an intermediate shocking of 2 hours at 600^oC for organic binder removal in the initial heat treatment.

2.2.4 Density Determination

After the heat treatment on the samples, the dry weights of the pellets were measured by a digital electronic balance. Then the samples were given different identification to avoid any confusion and kept together in a glass beaker. The samples containing beaker was kept in a vacuum oven and heated at $100^{o}C$. At this temperature water starts boiling and simultaneously vacuum was also created by the use of a suction pump. Heating the samples in the vacuum for 30 *minutes*, the pores present in the pellets were completely filled with water. The heater of the oven was switched off and the vacuum was slowly released. Now the beaker was taken out of the oven. The weight of the pellets were taken, in a digital electronic balance and interpreted as shocked weight. After the shocked weights were taken the samples were suspended in water with the help of a special designed hanger to hang the pellets inside water and the measured weight is interpreted as suspended weight. The experimental bulk density and apparent porosity were measured by using Archimedes principle;

$$Bulk\ Density = D / (W-I) \tag{2.10}$$

$$Apparent\ Porosity = (W-D) / (W-I) \tag{2.11}$$

where, *D*-Dry weight, *W*-Shocked weight and *I*-Suspended weight.

X-ray densities were calculated as suggested by B.D. Cullity

$$\rho = \frac{\sum A}{NV} \tag{2.12}$$

$$= \frac{1.66042 \sum A}{V} \tag{2.13}$$

where, ρ - X-ray density (g/cc), ΣA - Sum of the atomic weights of all the atoms in the unit cell, N - Avogadro's number, V - Volume of a unit cell. If the composition is of atomic weight A, then

$$\sum A = n_1 M \tag{2.14}$$

where n_1 - number of molecules per unit cell and M - molecular weight. The macroscopic density or the experimental bulk density of a particular specimen, determined from Archimedes principle is usually less and that can't exceed the X-Ray density, because the macroscopic specimen usually contains some cracks and pores.

2.2.5 Scanning Electron Microscopy

The scanning electron microscopy (SEM) is a useful technique to study the topography, morphology and composition of the materials with much higher resolution. When a beam of highly energetic electrons strikes the sample, the secondary electrons, x-rays and back-scattered electrons are ejected from the sample. These electrons are then collected by the detector and convert into signal that displays on a screen. In the present study, the SEM micrograph was taken on the fractured surface of the sample using scanning electron microscope (SEM: JSM-840 scanning microscope JEOL). As the samples are non-conducting, a thin layer of platinum is coated using a sputter coater. For measurement of the grain size, some lines of known length were drawn on the micrograph. The number of grains cut by the lines was counted. Then the average grain sizes were calculated by dividing the length of the line by the no of grain coming under that line. Minimum 10 lines, each

having the length not less than 200 micrometers were drawn on the different places of a single micrograph and average grain sizes were calculated to minimize the error. The chemical composition of the sample has been determined by Energy Dispersive X-Ray Spectrometry (EDX).

2.2.6 Raman Spectroscopy

Raman spectroscopy is an appropriate tool to get more insight into the local distortions, disorder and the strain present in the system because the vibrational spectrum has shorter characteristic length scale than required for the diffraction experiment. Raman scattering is also a useful tool to study the dynamics of structure by analyzing the characteristic modes associated with nano regions. The selection rules are very sensitive to the local and global symmetries.

In crystalline solids, the Raman Effect deals with phonons, instead of molecular vibrations. The fundamental requirement of a phonon to be Raman active is that the first derivative of the polarisability with respect to the vibrational normal coordinate has a non-zero value. A phonon can be active only in the crystals with no center of inversion.

The Raman spectra are usually plotted in intensity versus the difference in wave number between the incident beam and the scattered beam and the peaks are in correspondence to the phonon frequency. Due to the small wave vector of the optical photons, the phonons involved in the Raman scattering of crystalline solids have (from the wave vector conservation law) a very small momentum compared with

the Brillouin zone. So only the zone-centered phonons participate to the Raman scattering.

2.2.7 Electroding

The selection of suitable electrode for the test materials is important. In our case the contacting, conducting thin film electrode method is adopted because (i) it causes minimum error caused by air gap between the electrode and surface of the test material, which is more in case of contacting rigid metal electrode method, and (ii) procedure to measure dielectric constant are simple, which are relatively complex in non-contacting electrode method. In our case, all the ceramic bodies after sintering were polished well and coated on both sides with conducting silver paste. For organic removal printed disks were kept on an alumina plate and fired at $500^{o}C$ for 15 *minutes*. This procedure is repeated twice for better electroding.

2.2.8 Dielectric Measurement

To measure the relative permittivity (dielectric constant) and dielectric loss, LCR meter can be used. In this work, (LCR Tester (Hioki, Japan,42 Hz – $1MHz$) were used to measure the dielectric constant and dielectric loss. The electroded samples were used to make the measurements. The LCR meter, was interfaced with the computer and the data (capacitance and D factor) was collected as a function of temperature at different frequencies. The measured capacitance was then converted into dielectric constant using the following formula:

$$C = \epsilon_0 \epsilon_r \frac{A}{d} \tag{2.15}$$

$$\epsilon_r = \frac{C \times d}{\epsilon_0 \times A} \tag{2.16}$$

where, C : Capacitance in farad (F)

ε : Permittivity of free space in farad per meter (8.85 x $10^{-12} F/m$)

ε_r : Dielectric constant or relative permittivity of the sample.

A : Area of each plane electrode in square meters (m^2)

d : Separation between the electrodes in meters (m)

2.2.9 Impedance spectroscopy

The complex impedance spectroscopy is a powerful tool to investigate the electrical properties of the complex perovskite oxides. The main advantages of the techniques, i) it involves relatively simple electrical measurements that can readily be automated ii) the measurements can be implemented by using arbitrary electrodes iii) the results can be often correlated with the properties such as composition, microstructure, defects, dielectric properties, chemical reaction etc. of the sample iv) the resistance of the grain boundaries and that of grains can be easily separated in most of the polycrystalline samples. AC measurements are often made with a Wheatstone bridge type of apparatus (Impedance analyzer or LCR meter) in which the resistance R and capacitance C of the sample are measured and balanced against variable resistors and capacitors. The impedance $|Z|$ and the phase difference (θ) between the voltage and current are measured as a function of frequency for the

given sample and the technique is called impedance spectroscopy. Analysis of the data is carried out by plotting the imaginary part of the impedance $Z''=|Z|\cos\theta$ against the real part $Z'=|Z|\sin\theta$ on a complex plane called the impedance plot. An impedance plot with linear scale is used to analyze the equivalent circuit as follows. Impedance plot of a pure resistor is a point on real axis and that of pure capacitor is a straight line coinciding with the imaginary axis. The impedance of a parallel *RC* combination is expressed by the following relation,

$$Z^* = Z' - jZ'' = R / 1+j\omega RC \tag{2.17}$$

After simplification, one gets

$$\left(Z' - \frac{R}{2}\right)^2 + Z''^2 = \left(\frac{R}{2}\right)^2 \tag{2.18}$$

which represents the equation of a circle with radius $R/2$ and center at $(R/2,0)$. Thus, a plot of Z' vs. Z'' (as parametric function of) will result in a semicircle of radius $R/2$ as shown in Figure 2.2 (a) and the equivalent circuit is shown in Figure 2.2 (b). (This plot is often called a Nyquist plot). The time constant of the simple circuit is defined as $t = RC = 1/\omega_m$.

This corresponds to the relaxation time of the sample and the characteristic frequency lies at the peak of the semi-circle. In an ideal polycrystalline sample, the impedance plot exhibits an arc at high frequency corresponds to the bulk property of the sample, an arc at low frequency corresponds to the grain boundary behavior and a spike at the lowest frequency corresponds to the electrode effect. Figure 2.3 (a) shows a typical impedance plot for a polycrystalline sample and Figure 2.3 (b) represented the equivalent circuit. In the present work, impedance measurements

have been performed using Hioki LCR tester in the frequency range 42 - 1*MHz* at different temperatures.

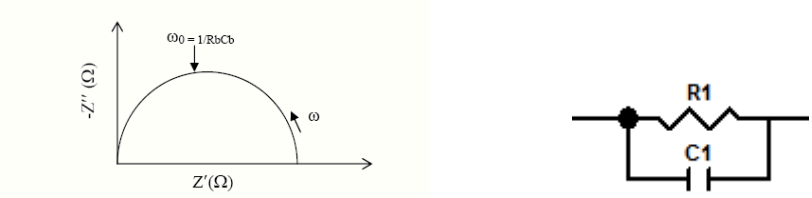

Figure 2.2 **(a)** The impedance plot for a circuit of a resistor and a capacitor in parallel and **(b)** the corresponding equivalent circuit

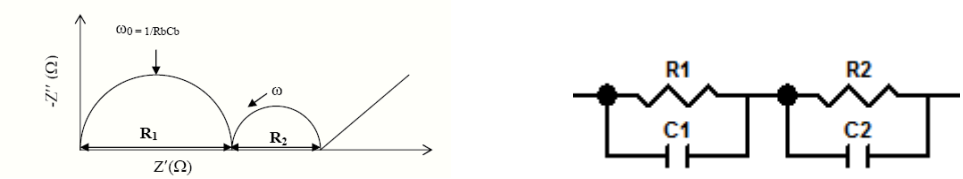

Figure 2.3 **(a)** The impedance plot for an ideal polycrystalline sample and **(b)** the corresponding equivalent circuit

2.2.10 Ultraviolet-visible absorption spectroscopy

The ultraviolet –visible spectroscopy deals with the recording of absorption of light in the visible and ultraviolet regions of the spectrum. Light of wavelength between 4000$\mathring{A}$ and 7500 $\mathring{A}$ (400-750 *nm*) is visible. Just beyond the red end of visible spectrum (wavelength more than 750*nm*) starts the infrared region and just beyond the violet end of the visible spectrum (wavelength less than 400 *nm*) lies the ultraviolet region. Thus, ultraviolet region starts at the blue end of the visible light (about 4000 $\mathring{A}$) and ends at 2000 $\mathring{A}$. This region is further sub-divided into near ultraviolet region and far or vacuum ultraviolet region (region below 2000 $\mathring{A}$). When radiant energy impinges upon a solution it may be absorbed, transmitted, reflected.

In spectrophotometery the absorbed light is determined. However, because of the difficulty of directly measuring the absorbed energy, the transmitted energy is measured and the amount absorbed is indirectly determined by subtracting the transmitted from the initial energy. The relationship $E=h\upsilon$, where E is the transition energy from the stable to excited state, h is the Planck's constant, and υ is the frequency. The energy of ultraviolet and visible radiation corresponds to that required for electronics transitions of the outer electrons. Since these are the valance electrons of the molecules or ions, the absorption spectra reflect the bonding characteristics of these particles. It is frequently impossible to obtain resolution of the numerous close absorption lines, and the plot of absorption vs wavelength yields a broad, smooth band spectrum.

2.2.11 Photoluminescence

Photoluminescence spectroscopy is a contactless, nondestructive method of probing the electronic structure of materials. Light is directed onto a sample, where it is absorbed and imparts excess energy into the material in a process called photo-excitation. One way this excess energy can be dissipated by the sample is through the emission of light, or luminescence. In the case of photo-excitation, this luminescence is called photoluminescence. The intensity and spectral content of this photoluminescence is a direct measure of various important material properties. Photo-excitation causes electrons within the material to move into permissible excited states. When these electrons return to their equilibrium states, the excess energy is released and may include the emission of light (a radiative process) or may not (a non-radiative process). The energy of the emitted light (photoluminescence)

relates to the difference in energy levels between the two electron states involved in the transition between the excited state and the equilibrium state. The quantity of the emitted light is related to the relative contribution of the radiative process.

2.2.12 Fourier Transforms Infrared Spectroscopy

Fourier transform infrared (FT-IR) spectroscopy is a powerful analytical tool for characterizing and identifying organic/inorganic samples. Using the IR spectrum, chemical bonds and the molecular structure of organic/inorganic compounds can be identified.

2.2.13 X-Ray Absorption Near-Edge Spectroscopy

The XANES principle is based on the determination of the X-Ray absorption coefficient μ depending on the photon energy hv at a fixed angle of illumination. As the optical excitation of a core level electron requires the binding energy E_B as minimum photon energy, the transgression of this energy will coincide with an increased absorption coefficient. This leads to the formation of absorption edges, which may be indexed by their atomic subshells (K,L,M...). Beyond the absorption edge the intensity of a monochromatic X-Ray passing through a medium of thickness d will follow the absorption law

$$I \propto \exp(-\mu d), \mu \propto \frac{Z^x}{(hv)^3}, 3 < x < 4, \quad (2.19)$$

where by μ depends the atomic number Z of the medium and decreases with increasing photon energy $h\nu$. However, the fine structure of this element-specific edge of the absorption coefficient is influenced by the energy of unoccupied electronic levels, as it is depicted in Figure 2.4 (a). Only sufficient photon energy enables the photoexcitation of a core level electron beyond the vacuum level E_{vac}. After 10×10^{-14} *sec* the ionized atom may relax by occupation of the core hole with an electron from the valence band (VB), while the generated energy will normally not be used for the emission of a fluorescence photon (probability 1 %), but will be absorbed for the vacuum emission of an *Auger electron* (probability 99%) from the valence band. In case of a non-sufficient energy for the emission of the primary electron, it may be excited into a conduction band (CB) level, so that a similar relaxation process becomes possible. This *spectator process* then results in the emission of only one Auger electron.

Alternatively the core hole may be reoccupied by the core level electron itself, so that the excitation energy is finally used for the emission of a valence electron. As the final state of this *participator process* is comparable to a direct photoemission process and as both mechanisms may happen concurrently, the participator excitation is also called resonant photoemission.

The number of generated secondary electrons is thereby directly proportional to the x-ay absorption cross section. On their way to the crystal surface these electrons undergo multiple scattering processes with other electrons (Figure 2.4 (b)), so that their number is multiplied while their averaged energy is reduced. Consequently, from the atomic layers near the surface up to 50 $\AA$ depth low-energy photoelectrons are emitted. For the determination of the absorption coefficient depending on the

photon energy two techniques are possible. The integrated detection of all emitted electrons (*total electron yield*) as well as the selective detection of electrons of fixed energy (*partial electron yield*) as a function of *hv* will lead to equivalent structures in the spectra.

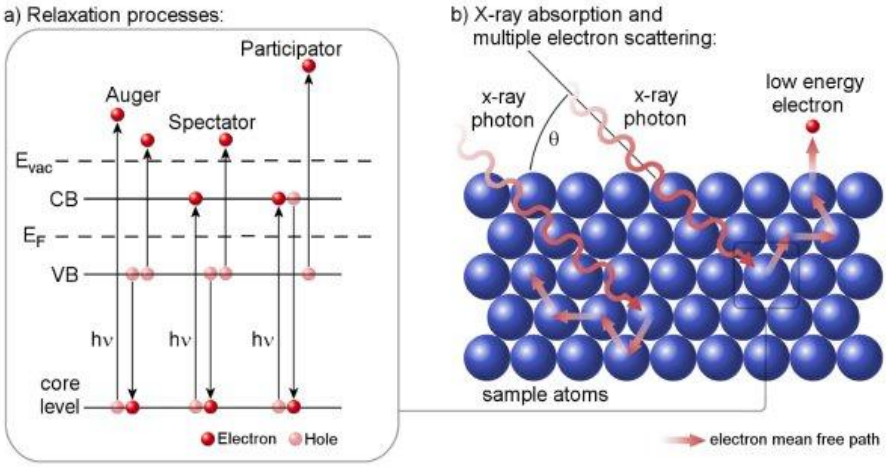

Figure 2.4 **(a)** Several ways of relaxation due to excitation of a core level electron and **(b)** Multiple scattering processes by secondary electrons.

CHAPTER 3

PHASE FORMATION AND DIELECTRIC STUDY OF $BaZr_XTi_{1-X}O_3$ CERAMICS

3.1 Introduction

$BaTiO_3$-based solid solutions are environment-friendly dielectrics with similar performances as shown by other Pb based electroceramics. Their properties can be tuned by composition and controlling their microstructural characteristics (porosity level, grain size, secondary phases, core-shell structures, etc). $BaZr_xTi_{1-x}O_3$ system is one of the most attractive material due to its phase formation mechanism *(Aliouane et al 2005; Bera and Rout 2005)*, local polar characteristics *(Farhi et al 1999)* and dielectric/tunability properties for microwave applications *(Weber et al 2001; Lee et al 2005)*. $BaTiO_3$ is known to form complete solid solution with $BaZrO_3$. It has been reported *(Hennings et al 1982)* that at ~ 15 atom% Zr substitution the three transition temperatures of $BaTiO_3$, rhombohedra to orthorhombic, orthorhombic to tetragonal and tetragonal to cubic, merge near room temperature and the doped material exhibits enhanced dielectric constant. With further increase in Zr contents beyond 15 atom %, a diffuse dielectric anomaly in ceramic has been observed with the decrease in the transition temperature *(Yu et al 2000)* and the material showed typical relaxor-like behaviour in the range 25–42 atom % Zr substitution *(Yu et al*

2002). It is also be found that for Zr 25 atom % has maximum dielectric constant in $BaZr_xTi_{1-x}O_3$ solid solution at room temperature. As Zr 25 atom% shows relaxor and maximum dielectric constant at room temperature a detail study on $BaZr_{0.25}Ti_{0.75}O_3$ ceramic has been done.

3.2 Outline of the present study

In the present work, $BaZr_xTi_{1-x}O_3$ solid solutions with different Zr contents, prepared using solid state reaction routes, were studied. Zr content in the present study was limited to 25 mol%. Beyond this, the ferroelectric phase transition temperature is well below room temperature and the compound behaves like a relaxor ferroelectric. Solid state mixed oxide technique is the most widely used method to prepare most of the ceramic materials for different applications. The phase purity and crystalline nature of the $BaZr_{0.25}Ti_{0.75}O_3$ (BZT) compounds were ascertained by X-ray powder diffraction (XRD) technique. The compositional accuracy of these compounds was confirmed by energy dispersive X-ray analysis (EDAX). Microstructural studies were done by scanning electron microscopy (SEM). The dielectric properties were measured using LCR meter. Efforts were made to correlate the microstructure with the functional properties. Details of all the experiments and characterization techniques mentioned above are discussed in Chapter 2.

3.3 Sample Preparation

$BaZr_xTi_{1-x}O_3$ ceramic was prepared by the solid state reaction route. In this synthesis method, barium carbonate ($BaCO_3$) (99.0%, E. Merck., India Ltd), titanium oxide

(TiO_2) (99.0%, E. Merck., India Ltd) and zirconium oxide (ZrO_2) (99.0%, E. Merck., India Ltd) were used as raw materials. These compounds were stoichiometricaly mixed using isopropyl alcohol (IPA) and milled using an agate mortar to obtain a homogeneous powder. Afterwards, these powders were ball milled for 12 *hrs*. The mixed powders were calcinied at different temperature for different duration to study the phase formation with repeated cycles of mixing and grinding. Finally, the pure $BaZr_xTi_{1-x}O_3$ (x=0.05 - 0.25) phase was obtained and pellets have been made.

3.4 Characterizations

The sample is characterized by the following tools to study of structural and electrical behavior.

3.4.1 Phase formation

Phase formation studies as a function of heat treatment temperature and duration were done. The phase purity and crystallinity of the ceramic compounds were confirmed by X-ray powder diffraction (XRD) method. Figure 3.1 shows the X-ray diffractograms of the $BaZr_{1-x}T_xO_3$ solid solution with 25 atom% Zr content heat treated at different temperatures for 6*h*. From the figure it is apparent that till about 1200^oC, $BaCO_3$ decomposition was not completed.

Figure 3.2 shows the X-ray diffraction patterns of the $BaZr_xTi_{1-x}O_3$ powder heat treated at 1350^oC for 6*h*. It can be clearly seen that for all Zr concentrations up to x = 0.25 ($0 \leq Zr \leq 0.25$), single phase $BaZr_xTi_{1-x}O_3$ is formed. A close examination of

Figure 3.2 reveals that as Zr content increased, the diffraction peaks (e.g., (110) shown by dotted line) were found to shift towards lower 2θ values suggesting an increase in lattice parameters due to the incorporation of Zr^{+4} ion in the Ti^{+4} ion site.

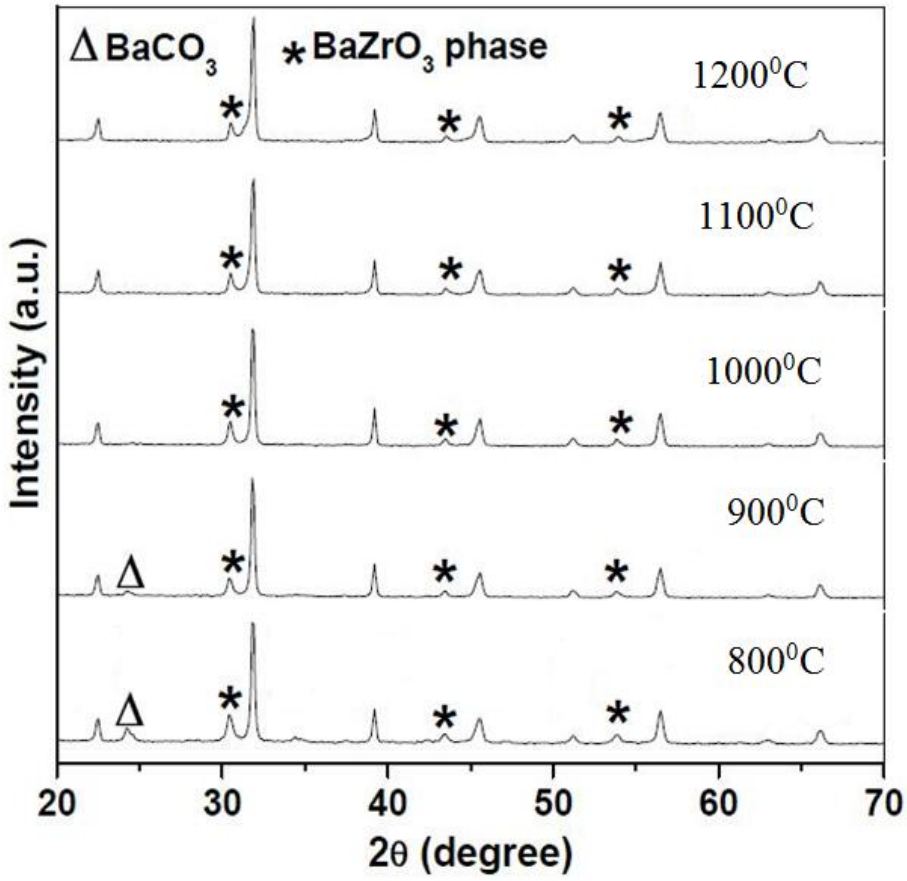

Figure 3.1 XRD of $BaZr_{0.25}Ti_{0.75}O_3$ powder heat treated at different temperatures for 6hrs

Table 3.1 XRD parameters of $BaZr_xTi_{1-x}O_3$ (x = 0.05 – 0.25) solid solutions heat treated at 1300^oC for 6 *h*

Composition	2θ (deg)	FWHM (deg)	d-spacing (Å)	a = b (Å)	c (Å)	c/a (Å)	Volume (Å)	crystallite size (Å)	strain
$BaZr_{0.05}Ti_{0.95}O_3$	31.56	0.24	2.8321	4.007	4.014	1.0017	64.49	344	0.371
$BaZr_{0.1}Ti_{0.9}O_3$	31.45	0.216	2.8413	4.018	4.026	1.0045	64.55	382	0.335
$BaZr_{0.15}Ti_{0.85}O_3$	30.86	0.288	2.8975	4.061	4.062	1.0002	67.68	286	0.456
$BaZr_{0.2}Ti_{0.8}O_3$	31.15	0.288	2.8542	4.036	4.036	1	65.775	286	0.448
$BaZr_{0.25}Ti_{0.75}O_3$	31.32	0.288	2.8685	4.052	4.052	1	66.557	286	0.451

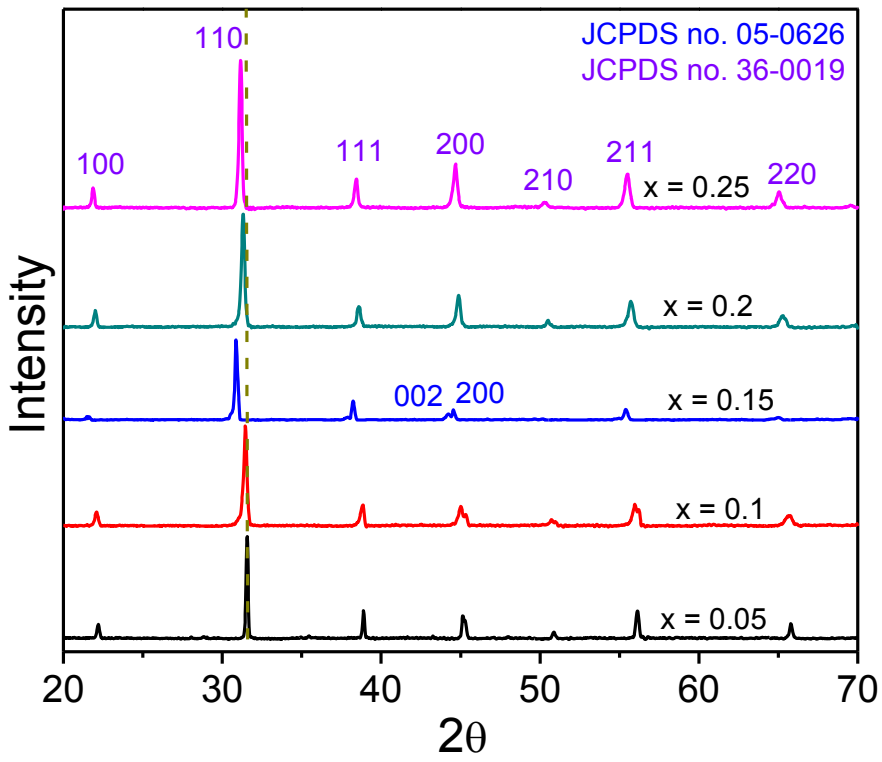

Figure 3.2 X-Ray diffractograms of $BaZr_xTi_{1-x}O_3$ (x = 0.05 – 0.25) solid solutions heat treated at 1350^oC for 6 *h*

3.4.2 X-ray diffraction and Rietveld refinement analysis of $BaZr_{0.25}Ti_{0.75}O_3$

In Figure 3.3 (a), the XRD pattern indicates that $BaZr_{0.25}Ti_{0.75}O_3$ ceramic shows cubic structure with space group *Pm*3*m*, in agreement with the respective Joint Committee on Powder Diffraction Standards (JCPDS) card N*o*. 36-0019. Diffraction peaks related to the deleterious phase were not detected, indicating a monophasic ceramic. Moreover, the sharp and well defined diffraction peaks indicate that this ceramic material has a degree of crystallinity at long range. The Rietveld refinement (as explained in chapter 2) is shown in Figure 3.3 (b). The lattice parameters and unit cell volume were calculated through Rietveld refinement. The obtained results from the Rietveld refinement are displayed in Table 3.2.

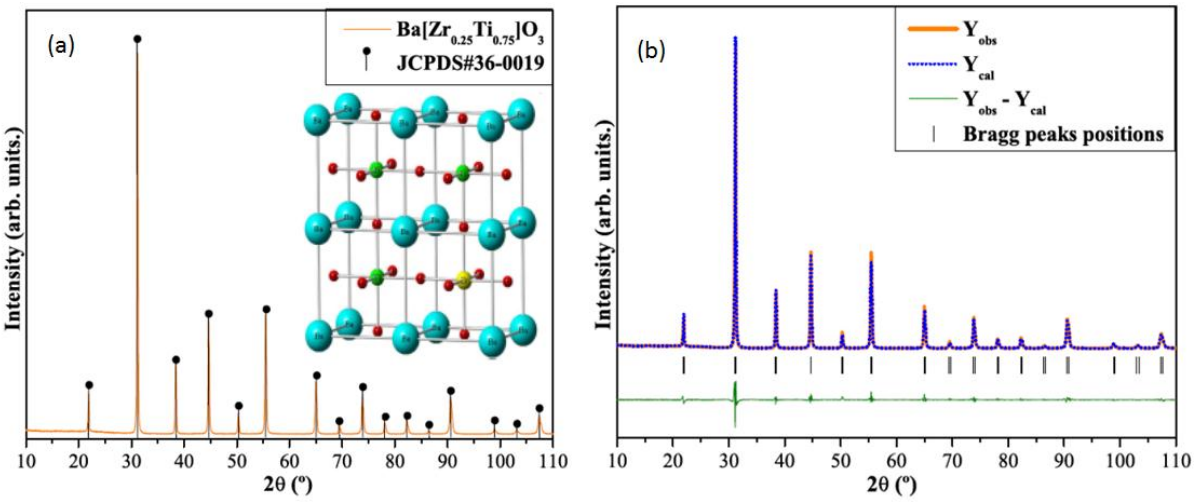

Figure 3.3 **(a)** XRD patterns and **(b)** Rietveld refinements plot of $BaZr_{0.25}Ti_{0.75}O_3$ ceramic

Table 3.2 Lattice parameters, unit cell volume, atomic coordinates and site occupation obtained from the Rietveld refinements for the $BaZr_{0.25}Ti_{0.75}O_3$ ceramic

Atoms	Site	*x*	*y*	*z*
Barium	1a	0	0	0
Titanium	1b	0.5	0.5	0.5
Zirconium	1b	0.5	0.5	0.5
Oxygen	3c	0.5	0.5	0
$a = b = c = 4.057$ *Å*, $V = 66.781$ Å^3				
$R_p = 8.83\%$, $R_{wp} = 11.78\%$, $R_{Bragg} = 2.96\%$, $\chi^2 = 2.606$,				

In this table, the fitting parameters (R_p, R_{wp}, R_{Bragg} and χ^2) indicate a good agreement between the refined and observed XRD patterns for the $BaZr_{0.25}Ti_{0.75}O_3$ phase. The refined lattice parameter values ($a = b = c = 4.057$ *Å*), unit cell volume ($V = 66.781$ Å^3) and bond angles ($\alpha = \beta = \gamma = 90^0$) confirmed that the $BaZr_{0.25}Ti_{0.75}O_3$ phase has a cubic structure. These Rietveld refinement results obtained in this work are in good

agreement with those reported in the literature for $BaZr_xTi_{1-x}O_3$ ceramics (*Huang et al 2008, Joseph et al 1999)*.

3.4.3 Compaction and Sintering

Densification behaviour as a function of sintering temperature was also studied. Figure 3.4 shows the effect of sintering temperature for a given sintering duration on the ceramic density. The maximum density was obtained at 1450^oC for 4hrs as further increase in temperature, resulted in a decrease in density. The decrease in density above 1450^oC could be due to the loss of certain constituents in the ceramic. The poor density at 1400^oC indicates that the temperature is insufficient to meet the diffusion requirements within the sample. Since sintering in ceramics is essentially a diffusion controlled process, sufficient thermal energy will be required for the diffusion to take place.

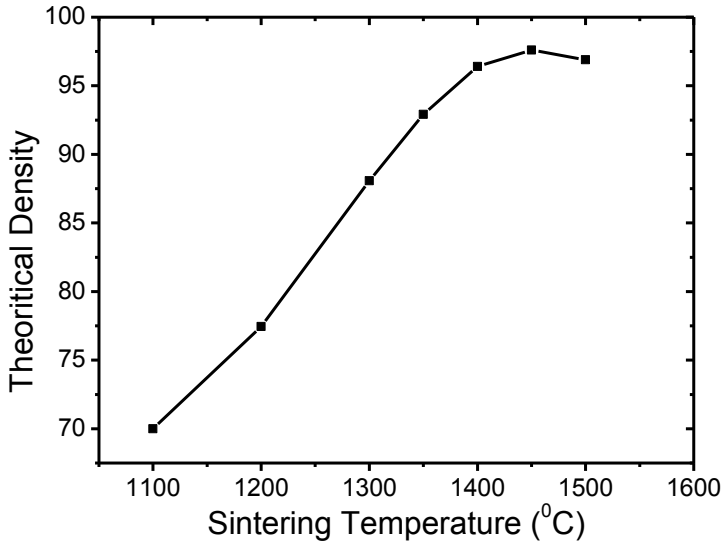

Figure 3.4 Effect of sintering temperature on the density of $BaZr_{0.25}Ti_{0.75}O_3$ ceramic

Considerable increase in the density at 1450^oC suggests that most of the interconnected pores might have been closed and grain growth rate is improved at this temperature because of the improved diffusion rates. At 1450^oC, the density of the sintered ceramic reached maximum suggesting that diffusion is no longer possible.

3.4.4 Microstructure

Figure 3.5 shows the micrograph $BaZr_{0.25}Ti_{0.75}O_3$ ceramic. As it can be seen in this micrograph, the $BaZr_{0.25}Ti_{0.75}O_3$ ceramic is composed of large grains with an average size of approximately $10\mu m$. We believe that these morphological characteristics are governed by the matter transport mechanism between the grains during the sintering process. In principle, in the initial stages of small solid state reaction route, the carbonates and oxides ($BaCO_3$, TiO_2 and ZrO_2) used to form the $BaZr_{0.25}Ti_{0.75}O_3$ phase are well mixed and constantly milled in order to reduce the powder particle sizes.

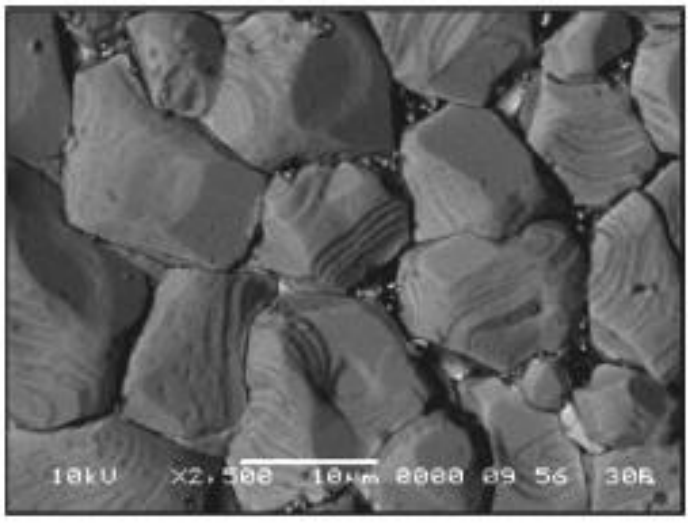

Figure 3.5 Microstructure of $BaZr_{0.25}Ti_{0.75}O_3$ ceramic sintered at 1450^oC for 4hrs

The heat treatments performed at 1450^oC for 4 hrs promotes a slow kinetics of inter diffusion in the contact points between the particles with irregular morphologies *(Lal et al 2000)*. Probably, this diffusion process leads to the formation of necks between the grains due to an elastic deformation caused by the surface energy reduction in the contact interface *(Rahaman et al 1995)*. The neck growth is favoured by the long sintering time, allowing the matter transport at long distances *(Kang et al 2005)*. In this process, the grain boundaries play a fundamental role in the material transport into the system. The formation of large grains with irregular shapes could be a result of the variations on the kinetics of movement from boundary to boundary, since the grain-boundary energy is dependent on the grain-boundary orientation and grain-boundary mobility (*Kang et al 2005).* When the sintering process was performed at 1450^oC for $4h$, the grain growth process was intensified, causing a reduction in the number of pores and disappearing with some grains, generally the smaller ones *(Rahaman et al 1995)*. In Figure 3.5, the occurrence of grooves between the grains was also observed. According to *(Ramasubramaniam et al 2005)*, this phenomenon is caused by a capillarity driven process, where the grain boundary emerges to intersect a free surface *(Reddy et al 2009).* In this case, the system seeks to minimize the combined energy of the grain boundary and the free surface by developing a groove at the point of intersection. The excess energy associated with the grain boundary provides the driving force to sustain the grooving process.

3.4.5 Stoichiometry

The compositional characterization of $BaZr_{0.25}Ti_{0.75}O_3$ ceramics was done using Energy Dispersive and X-Ray spectroscopy (EDXS). Measurement was taken at different location and the bulk composition of the sample was averaged from those measurements. Table 3.3 shows the nominal and Energy Dispersive and X-Ray spectroscopy (EDXS) derived composition of the $BaZr_{0.25}Ti_{0.75}O_3$ (BZT) ceramic.

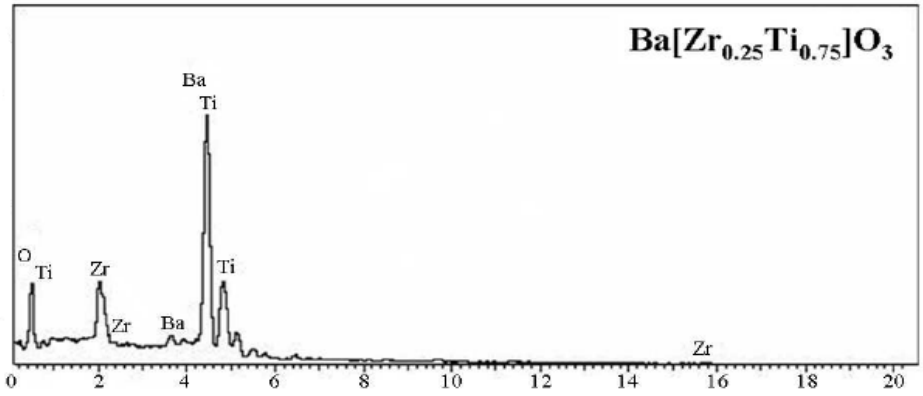

Figure 3.6 Energy Dispersive and X-Ray spectroscopy (EDXS) spectrum showing the elemental composition taken on $BaZr_{0.25}Ti_{0.75}O_3$

Table 3.3 Compositional analysis of $BaZr_{0.25}Ti_{0.75}O_3$ ceramic Energy Dispersive and X-Ray spectroscopy (EDXS)

Element	Wt % Calculated	Wt% from EDXS
Ba	55.87	55.91
Zr	9.46	9.66
Ti	15.01	14.94
O	19.66	19.49

The small fluctuations in the Energy Dispersive and X-Ray spectroscopy (EDXS) derived composition could be due to two reasons: 1) deficiency of oxygen during sintering in the ambient, which influences the calculation of composition from EDXS values as the summation of individual quantities of elements is equaled to 100% and 2) it is always difficult to get the microscopic uniformity in the composition in solid

state mixed oxide technique. Figure 3.6 shows Energy Dispersive and X-Ray spectroscopy (EDXS) pattern taken on a $BaZr_{0.25}Ti_{0.75}O_3$ (BZT) ceramic.

3.4.6 Dielectric Study of $BaZr_{0.25}Ti_{0.75}O_3$

Figure 3.7 shows the temperature dependence of relative real and imaginary dielectric permittivity performed at different frequencies (1 *kHz*, 10 *kHz*, 100 *kHz* and 1 *MHz*) for the $BaZr_{0.25}Ti_{0.75}O_3$ ceramic. The real permittivity (ε') value gradually increases up to a maximum value (ε_m) with the increase of temperature, and then it smoothly decreases, suggesting a phase transition. The maximum relative permittivity (ε_m) as well as its corresponding temperature (T_m) is dependent on the frequency. In this case, the relative dielectric permittivity magnitude decreases with the increase in the frequency, shifting the maximum value (ε_m) to higher temperatures. Hence, this result indicates that the dielectric polarization has relaxation-type behaviour. As can be seen in Figure 3.7, the dielectric loss value corresponding to the ferroelectric phase was substantially reduced at room temperature up to the paraelectric phase (above T_m). Probably, the frequency dispersion at lower temperatures (below T_m) is because of the presence of space charges.

The high dielectric loss (ε") value at 1 *kHz* can be related to the different types of polarization and/or caused by the finite resistivity of the material. Moreover, the increase of the ε' values in the region of low temperatures could be arising from the increase in the ionic conductivity as a consequence of a local disorder or displacement between the Ti–O, Zr–O, Ba–O bonds.

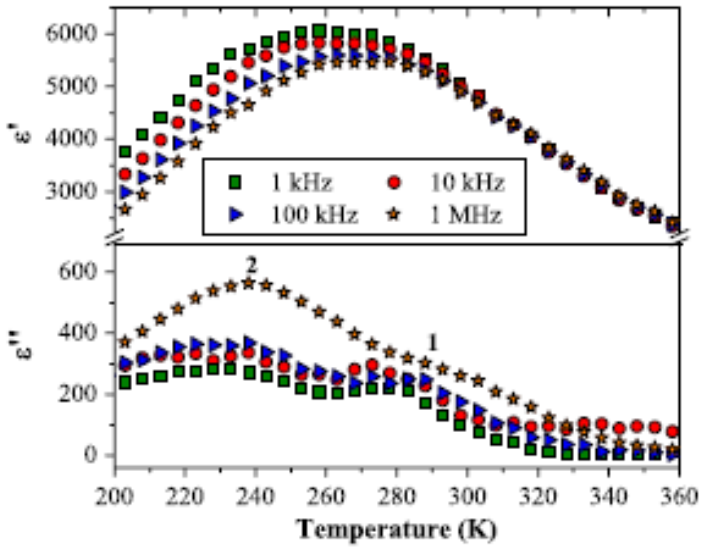

Figure 3.7 Temperature dependence of real and imaginary permittivity at different frequencies for the $BaZr_{0.25}Ti_{0.75}O_3$ ceramic

In this case, this symmetric break induces the charge mobility into the octahedral clusters *(Moreira et al 2008)*. In figure 3.7, when the frequency was increased, an increase in the dielectric loss with the temperature evolution was verified. This result indicates that the dielectric polarization is caused by a relaxation type as those observed in dipolar glasses *(Wang et al 2005)*. Also, two relaxation peaks were observed in the graph corresponding to the ε'' as a function of temperature. The first, one located at 240 *K*, is generally ascribed to the transition from crystalline to glassy phase, while the second one, at 290 *K*, represents the molecular motion of the glass phase. In analogy with spin glasses, the dynamic susceptibility behaviour in disordered ferroelectrics is supposed to be associated with a broad spectrum of relaxation times. Qualitatively, the strong and broad dielectric peak indicates that the phase transition is diffuse type near the transition temperature (T_m). This phenomenon can be related to the inhomogeneous distribution of $[ZrO_6]$ clusters into the Ti sites and/or by the mechanical stresses on the grains *(Tang et al 2004)*. At

10 *kHz*, the maximum relative dielectric permittivity (ε_m) of $BaZr_{0.25}Ti_{0.75}O_3$ ceramic was detected at 267K (T_m). The diffuse transition nature, especially in the case of ferroelectric ceramics, is usually attributed to the grain size distribution and/or a quadratic gradient, leading to a transition temperature distribution. This phenomenon is more pronounced in samples containing both $[TiO_6]$ and $[ZrO_6]$ clusters in its compositions, probably as a consequence of the difference in the electronic density between the polar $[TiO_6]$ and non-polar $[ZrO_6]$ clusters. Hence, the additional spatial fluctuations caused by the $[TiO_6]$ and $[ZrO_6]$ clusters into the structure lead to the coexistence of regions with different Curie temperatures, which are dependent on the Ti and Zr concentrations in the solid solution *(Reddy et al. 2007*).

3.4.7 Diffuse Phase Transition

A diffuse phase transition is commonly observed by the broadening of the dielectric constant (ε) as a function of temperature (T). The large separation (in temperature) between the maximum real and imaginary (dielectric loss) points from the dielectric constant curve, deviation from the Curie–Weiss law near T_m, frequency dispersion of both dielectric and dielectric loss in the transition region imply a frequency dependence with T_m *(Dixit et al 2003, Maiti et al 2007)*. Figure 3.8 (a) shows the inverse dielectric constant as a function of temperature performed at different frequencies (1 *kHz*, 10 *kHz*, 100 *kHz* and 1 *MHz*) for the $BaZr_{0.25}Ti_{0.75}O_3$ ceramic.

A deviation from the Curie–Weiss law can be observed for all frequencies (Figure 3.8(a)). This deviation is a typical behavior of ferroelectric materials with diffuse

phase transition. The parameter ΔT_m describes the degree of deviation from the Curie–Weiss law and is defined as $\Delta T_m = T_{cw} - T_m$, where T_{cw} denotes the temperature where the dielectric permittivity starts to deviate from the Curie–Weiss law and T_m is the temperature of the dielectric maximum *(Tang et al 2005).* The Curie temperature is determined from the graph by the extrapolation of the reciprocal dielectric constant in the paraelectric region. The obtained results are displayed in Table 3.4. A modified Curie–Weiss law has been proposed to describe the diffuseness in a phase transition *(*Uchino and Nomura *1986)*

$$\frac{1}{\varepsilon} - \frac{1}{\varepsilon_m} = (T - T_m)^{\gamma}/C' \qquad (3.1)$$

where both γ and C' are constants. The parameter γ gives information on the phase transition character ($\gamma = 1 \rightarrow$ a normal Curie–Weiss law is obtained and $\gamma = 2 \rightarrow$ it reduces to the quadratic dependence which describes a complete diffuse phase transition).

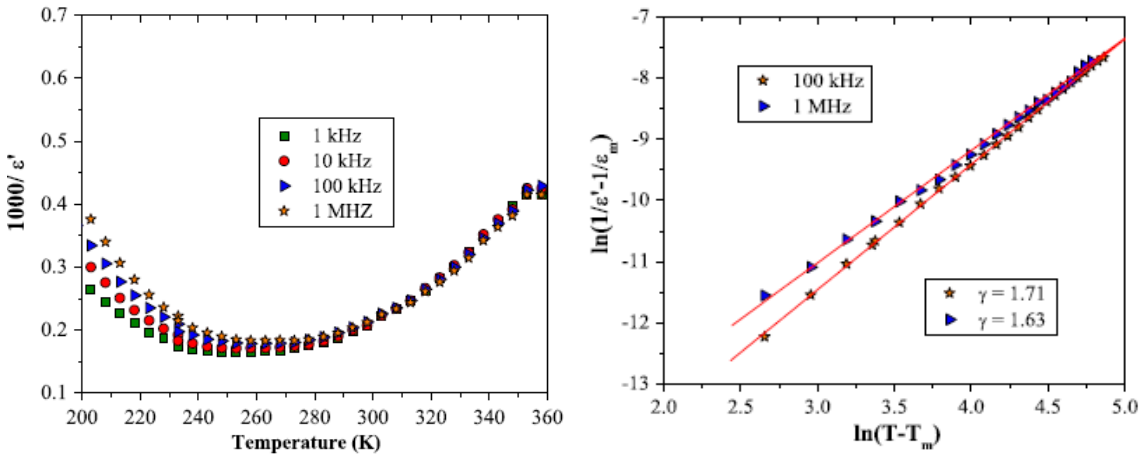

Figure 3.8 **(a)** Inverse dielectric constant as a function of temperature at different frequencies and **(b)** $\ln(1/\varepsilon - 1/\varepsilon_m)$ as a function of $\ln(T - T_m)$ plot at frequencies of 100 *kHz* and 1 *MHz* for the $BaZr_{0.25}Ti_{0.75}O_3$ ceramic

Table 3.4 Parameters obtained through the dielectric data as a function of temperature at different frequencies for the $BaZr_{0.25}Ti_{0.75}O_3$ ceramic

Frequency	T_m (K)	T_o (K)	ΔT_m (K)	ε_m	T_{cw} (K)
1 kHz	258(±1)	296(±1)	75(±2)	6062(±3)	333(±2)
10 kHz	263(±1)	303(±1)	80(±2)	5836(±3)	343(±2)
100 kHz	273(±1)	308(±1)	88(±2)	5572(±3)	361(±2)
1 MHz	283(±1)	321(±1)	90(±2)	5420(±3)	374(±2)

The plot of log $(1/\varepsilon'-1/\varepsilon_m)$ vs log $(T-T_m)$ at 100 *kHz* and 1 *MHz* for $BaZr_{0.25}Ti_{0.75}O_3$ ceramic is shown in Figure 3.8(b). Linear relationships are observed. The slopes of the fitting curve are used to determine the parameter γ value. The γ value was found to be 1.71 for 100 *kHz* and 1.63 for 1 *MHz*, respectively. An important observation on the fit performed in our experimental data by means of equation (3.1) indicated that a universal γ value was not obtained in the temperature range above T_m. The γ value continuously approaches unity when it departs from T_m. This value suggests that the material has structural order–disorder and diffuse phase transition. The observed broadness or diffusiveness occurs mainly because of the compositional fluctuation and/or due to the structural disorder into the lattice by the $[TiO_6]$ and $[BaO_{12}]$ clusters. This behaviour suggests a microscopic heterogeneity into the $BaZr_{0.25}Ti_{0.75}O_3$ structure, presenting different local Curie points. The nature and variation of the dielectric constant as well as the presence of non-polar $[ZrO_6]$ clusters indicate that the material has a ferroelectric–relaxor phase transition.

3.4.8 Vogel- Fulchur Equation

For a more detailed insight into the relaxation process in the relative dielectric permittivity, a graph of $1/T_m$ was plotted as a function of ln(f), as shown in Figure 3.9. In this figure, the nonlinear nature indicates that the data cannot be fitted by the simple Debye equation. In order to analyze the relaxation characteristics of $BaZr_{0.25}Ti_{0.75}O_3$ ceramic, the experimental curves were fitted using the Vogel–Fulcher equation *(Guo et al 2004)*

$$f = f_0 exp\left[\frac{E_a}{k_B(T_m - T_f)}\right] \tag{3.2}$$

where ν_o is the attempt frequency, E_a is the measure of average activation energy, k_B is the Boltzman constant and T_f is the freezing temperature. The T_f is considered as the temperature where the dynamic reorientation of distorted [TiO_6] clusters leads to polarization in the lattice.

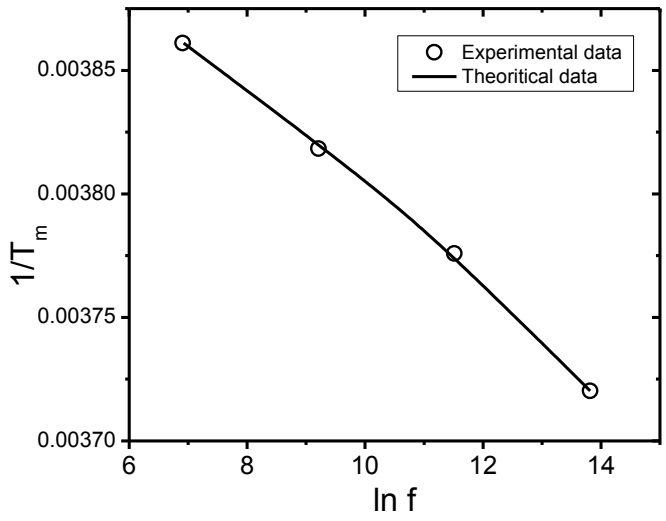

Figure 3.9 $1/T_m$ as function of ln(f) for the $BaZr_{0.25}Ti_{0.75}O_3$ ceramic. The symbols are the experimental points and the line is the Vogel–Fulcher relation

The fitting parameters are T_f = 128 *K*, E_a = 0.1538 *eV* and $f_o = 1.03 \times 10^{11}$ *Hz*. The empirical relaxation strength described by the frequency dispersion of T_m is defined as $\Delta T_{res} = T_m(1MHz) - T_m(10\ kHz)$, where ΔT_{res} is derived from the dielectric measurement of the ceramic compound. In our work, this value is approximately 17.14 *K*.

3.4.9 Impedance study

Fig. 3.10 shows the Nyquist plots (complex impedance spectrum) of $BaTi_{0.75}Zr_{0.25}O_3$ at different temperatures. This plot shows the transport response function. The symbols represent the experimental data the solid line represents the theoretical fitting of equation

$$Z^* = \frac{R}{1+(j\omega/\omega_0)^{1-n}} \tag{3.3}$$

Characteristically, two semicircular arcs have been observed. The low frequency semicircle is considered due to the grain boundary (blocking core) whereas the higher frequency semicircle depicts the bulk effect. This bulk effect arises due to the parallel combination of bulk resistance (R_b) and bulk capacitance (C_b) of $BaTi_{0.75}Zr_{0.25}O_3$ as shown in the equivalent circuit (Figure 3.10 (inset)). The value of bulk resistance (R_b) and grain boundary resistance (R_{gb}) at different temperatures has been obtained from the intercept of the semicircular arc on the real axis (Z'). The values of Resistance and Capacitance are given in Table 3.5. This plot indicates the changes in grain boundary resistance at elevated temperatures representing the role of grain boundaries in electrical conduction process of the material. The decrease in

grain boundary resistance with rise in temperature may be due to the lowering of barrier favoring the increase of mobility of charge carriers that adds to the conduction process.

The activation energy due to grain and grain boundary is found to be 0.42 *eV* and 0.34 *eV* respectively. The conduction mechanism for grains and grain boundaries are different.

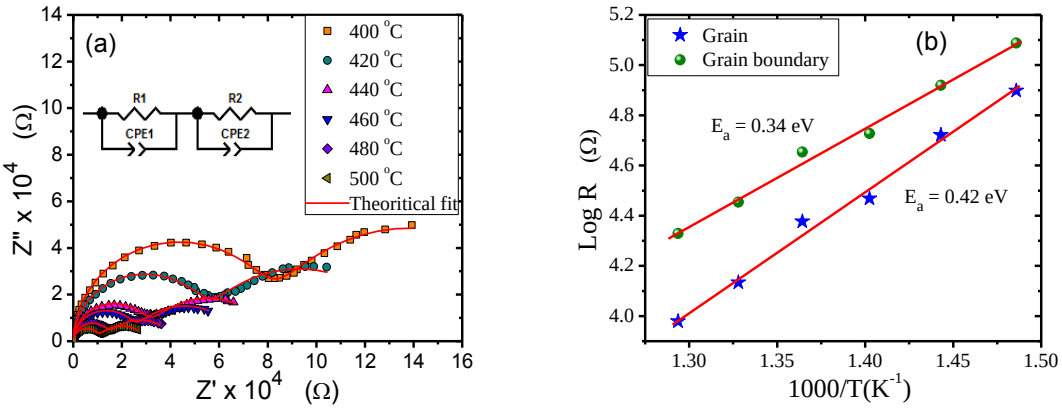

Figure 3.10 **(a)** Nyquist plots of $BaTi_{0.75}Zr_{0.25}O_3$ at different temperatures, (inset) equivalent circuit and **(b)** Temperature dependence of Grain and Grain boundary Resistance

Table 3.5 Grain and grain boundary Resistance and Capacitance of $BaTi_{0.75}Zr_{0.25}O_3$ at different temperatures

$T\ (^oC)$	$CPE_g\ (nF)$	$R_g\ (K\Omega)$	$CPE_{gb}\ (nF)$	$R_{gb}\ (K\Omega)$
400	0.191	79.05	25.1	122.5
420	0.185	52.68	34.0	83.15
440	0.190	29.40	56.4	53.36
460	0.186	23.83	69.2	45.01
480	0.171	13.62	98.4	28.43
500	0.166	9.54	137.0	21.31

A hopping mechanism through various defect sites contributes the intergrain conduction whereas the interface barrier potential plays the major role for intra-grain boundary condition *(Pradhan et al 2005)*. From Figure 3.10 (a) it is clear that the value of R_b and R_{gb} decreases with rise in temperature. This shows the negative temperature coefficient of resistivity (NTCR) behavior like that of a semiconductor.

3.4.10 AC and DC conductivity

The ac conductivity can be represented as,

$$\sigma(w) = \sigma(0) + A\omega^n \tag{3.4}$$

where L and A are the thickness and area of the sample respectively. Figure 3.11 (a) shows the variation of conductivity as a function of frequency at various temperatures for $BaZr_{0.25}Ti_{0.75}O_3$ (BZT) ceramic. The plot exhibits two different regions associated with different phenomena (i) an independent plateau region at low frequency region corresponding to DC conductivity and (ii) a frequency dispersion region at higher frequencies. It is clearly seen that the frequency at which the dispersion becomes predominant shifts towards higher frequency region as the temperature increases.

In the present work the DC conductivity at different temperatures has been extracted from the extrapolation of frequency independent plateau region from log σ versus log ω plot. Figure 3.11 (b) shows the temperature dependence of DC conductivity and slopes obey Arrhenius relation,

$$\sigma = \sigma_0 \, exp\left[-\frac{E_a}{k_B T}\right] \tag{3.5}$$

where σ_o is the pre-exponential factor, E_a is the activation energy and k_B is the Boltzmann constant. The activation energy from Dc conductivity is found to be 0.36 *eV.*

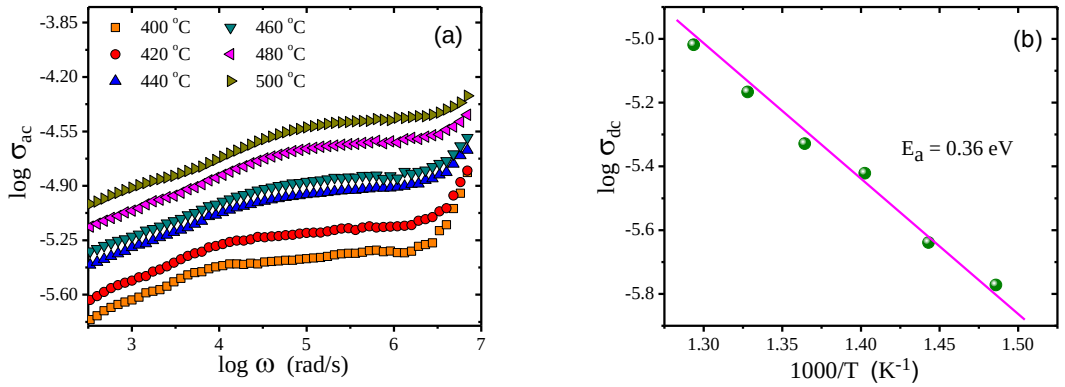

Figure 3.11 **(a)** Frequency dependence of the *AC* conductivity and **(b)** Temperature dependence of DC conductivity of $BaZr_{0.25}Ti_{0.75}O_3$ ceramic at various temperatures

3.4.11 Modulus analysis

The modulus analysis has an advantage that it suppresses the information about electrode effects *(Hodge et al., 1976; Sobha and Rao, 1995; Ganguli et al, 1999; Lanfredi et al, 2002).* This can also be used to study conductivity relaxation times *(Lanfredi et al, 2002; Ghosh and Ghosh, 2002).* The complex modulus is defined as the inverse of the complex permittivity and in the present work, the impedance data were converted into electrical modulus using the relations M' (real part) = $\omega C_0 Z''$ and M'' (imaginary part) = $\omega C_0 Z'$, where $C_o = \varepsilon_0 A/L$, A is the area of the sample, L is the thickness of the sample and $\varepsilon_o = 8.854 \times 10^{-14}$ F/cm is the permittivity of the free space *(Nowick and Lim, 1994)*. Figure 3.12 (a) and (b) shows the variation of real and

imaginary part of electric modulus as a function of frequency at different temperatures respectively. At lower frequencies, M' tends to be very small, confirming that the contribution from the electrode effect is negligible and hence can be ignored when the data are analyzed in modulus formalism *(Howell et al, 1974)*. The observed dispersion in M' at higher frequencies may be due to conductivity relaxation. The M'' versus log ω plot shows broad and asymmetric peaks compared to the peak predicted for ideal Debye type. The asymmetric nature of M'' plot is suggestive of stretched exponential character of relaxation times of the material. Each peak attains a maximum value M''_{max} at frequency ω_{max} called conductivity relaxation frequency and it obeys the Arrhenius relation. Figure 3.12 ((b) inset) shows the plot of peak frequency (ω_{max}) versus $1000/T$ and the activation energy is $0.43eV$. Figure 3.13 (a) shows the normalized plot of M''/M'' max versus log (ω/ω_{max}) at various temperatures. The plot also shows that ω_{max} shifts towards higher frequencies with increasing temperature. This suggests that conductivity relaxation mechanisms occurring at different frequencies exhibit different thermal energy and the dynamical processes are temperature dependent. This is mainly due to the existence of polar regions around this temperature range, where the system shows Diffuse Phase transition (DPT) in the dielectric response.

Figure 3.13 (b) shows that the Z'' peak coincides with the peak in M''. The closer value of activation energies obtained from the analysis of Z'' , M'' and the conductivity data suggests that there is some kind of hopping mechanism involved along with the dipolar orientation in the investigated sample.

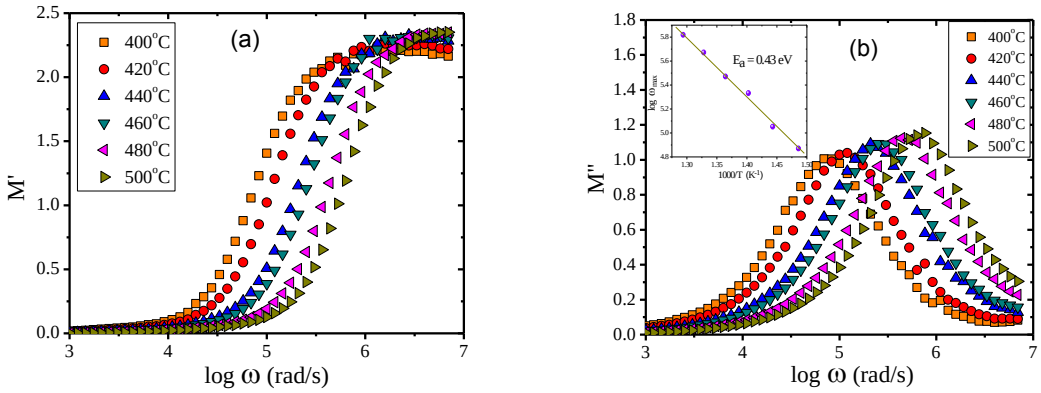

Figure 3.12 **(a)** Variation of real part of modulus, **(b)** imaginary part of modulus of $BaZr_{0.25}Ti_{0.75}O_3$ ceramic with frequency at different temperatures and **(inset)** Arrhenius plot of *log* ω_{max} from imaginary part of impedance

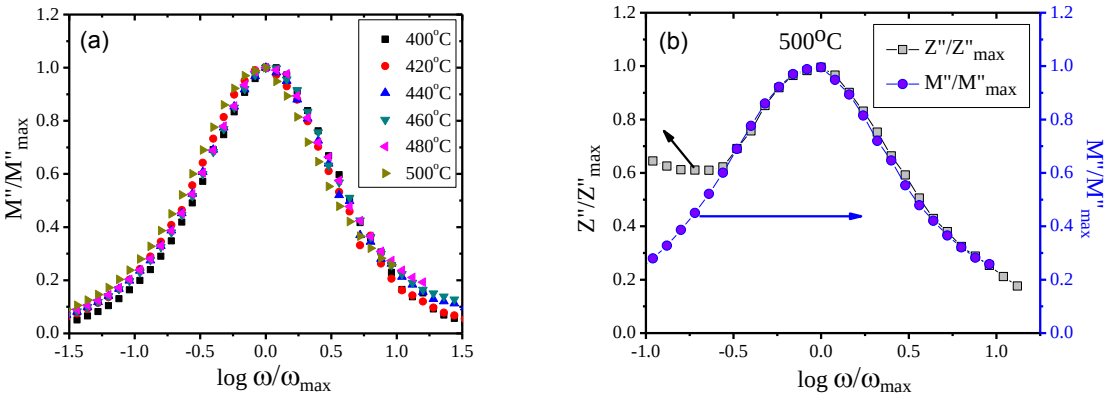

Figure 3.13 **(a)** Scaling behaviour of *M"* at various temperatures and **(b)** Frequency dependence of normalized peaks, *Z"/Z"$_{max}$* and *M"/M"$_{max}$* for $BaZr_{0.25}Ti_{0.75}O_3$ ceramic at 500 ^oC

CHAPTER 4

FREQUENCY AND TEMPERATURE DEPENDENCE STUDY OF HETEROVALENT BISMUTH SUBSTITUTED $BaZr_{0.25}Ti_{0.75}O_3$ CERAMIC

4.1 Introduction

Substantial quantities of heterovalent ions of proper ionic radius can enter $BaTiO_3$ lattice and cause gradual alteration of properties. A given ion can have radically different effects on the microstructure, nature of the dielectric and ferroelectric properties. However, ions of suitable size but unmatched valency, although limited in solubility, can cause profound changes in the nature of the dielectric and ferroelectric properties. By substituting the combinations of atoms replacing both Ba and Ti sites to $BaTiO_3$ extensive solid solution is possible provided the ionic sizes are properly chosen. These substitutions modify the ferroelectricity and almost always depress the Curie point sharply. It has been clearly observed from the previous chapter that isovalent Zr^{4+} substitution in place of Ti^{4+} in $BaTiO_3$ significantly altered its structural and functional properties. Substitution of heterovalent (having different valency to that of the replacing ion) cations in $BaZr_xTi_{1-x}O_3$ can drastically alter its dielectric and ferroelectric properties. Usually, in isovalent substitution, the substituent and substituted elements have the same valency. However, in heterovalent substitution, the substituent ion can replace

either A site or B site depending up on the ionic size and defect vacancy availability. It has been reported that heterovalent ion substitution in $BaTiO_3$ resulted in occupancy of both A and B sites. Hence, it will be interesting to study the influence of heterovalent ion substitution on the structural and functional properties of $BaZr_xTi_{1-x}O_3$ compound.

4.2 Outline of the present study

This chapter aims to study the effect of Bi^{+3} ion substituted on $BaZr_{0.25}Ti_{0.75}O_3$ ceramic. The chapter starts with the synthesis and followed by characterizations. The samples were synthesized by solid state reaction route and then characterized by X-Ray Diffraction, Scanning Electron Microscopy, Energy Dispersive X-Ray Spectroscopy, Dielectric study and impedance spectroscopy.

4.3 Sample Preparation

The samples were prepared through solid state reaction route. The compositions were prepared from $BaCO_3$ (E. Merck India Ltd), Bi_2O_3 (Loba Chem., Mumbai), TiO_2 (E. Merck India Ltd.) and ZrO_2 (E. Merck India Ltd). All the chemicals were having more than 99% purity. The raw powders were thoroughly mixed in agate mortar using IPA. The mixed powders were ball milled for 12 hrs in acetone medium. The intension of using ball milled is proper mixing of powder. After ball milling the powders were dried at room temperature. Then the dried powders were again grinded for 2 hrs in agate mortar. The homogenous mixture was calcined at 1350^oC

for 6 hrs with intermediate mixing and grinding. Then pellets were made by hydraulic press. The pellets were sintered at optimized temperature $1450^{o}C$ for 4hrs in a programmable furnace. The density of the pellets was measured by using Archimedes's principle. The measure density of the samples is given below in Table 4.1.

Table 4.1 The optimized sintering temperature and density of $Ba_{1-x}Bi_{2x/3}Zr_{0.25}Ti_{0.75}O_3$ ceramic

$Ba_{1-x}Bi_{2x/3}Zr_{0.25}Ti_{0.75}O_3$	Sintering Temperature	Theoretical Density
x = 0.0	1450^0C	98%
x = 0.025	1450^0C	95%
x = 0.05	1450^0C	93%

4.4 Characterization

The samples were characterized by the following tools and the results were discussed.

4.4.1 X-Ray Diffraction

Figure 4.1 (a) shows the XRD patterns of $Ba_{1-x}Bi_{2x/3}Ti_{0.75}Zr_{0.25}O_3$ (x= 0, 0.025 and 0.05) ceramics with different Bi (x) content. The pattern shows that the compositions are of single phase cubic perovskite structure without the evidence of any additional phase. This indicates Bi forms complete solid solution with $BaTi_{0.75}Zr_{0.25}O_3$ in the studied composition range. There is a little shift of the peaks towards higher angles indicating decrease in lattice parameters due to the incorporation of smaller Bi in place of Ba. Figure 4.1 (b) shows the variation of crystallite size and cell volume with increase in Bi content. The lattice parameters

and the unit cell volume (Table 4.2) decrease with increase in Bismuth content. This is expected, as the ionic radius of Bi is smaller than that of Ba.

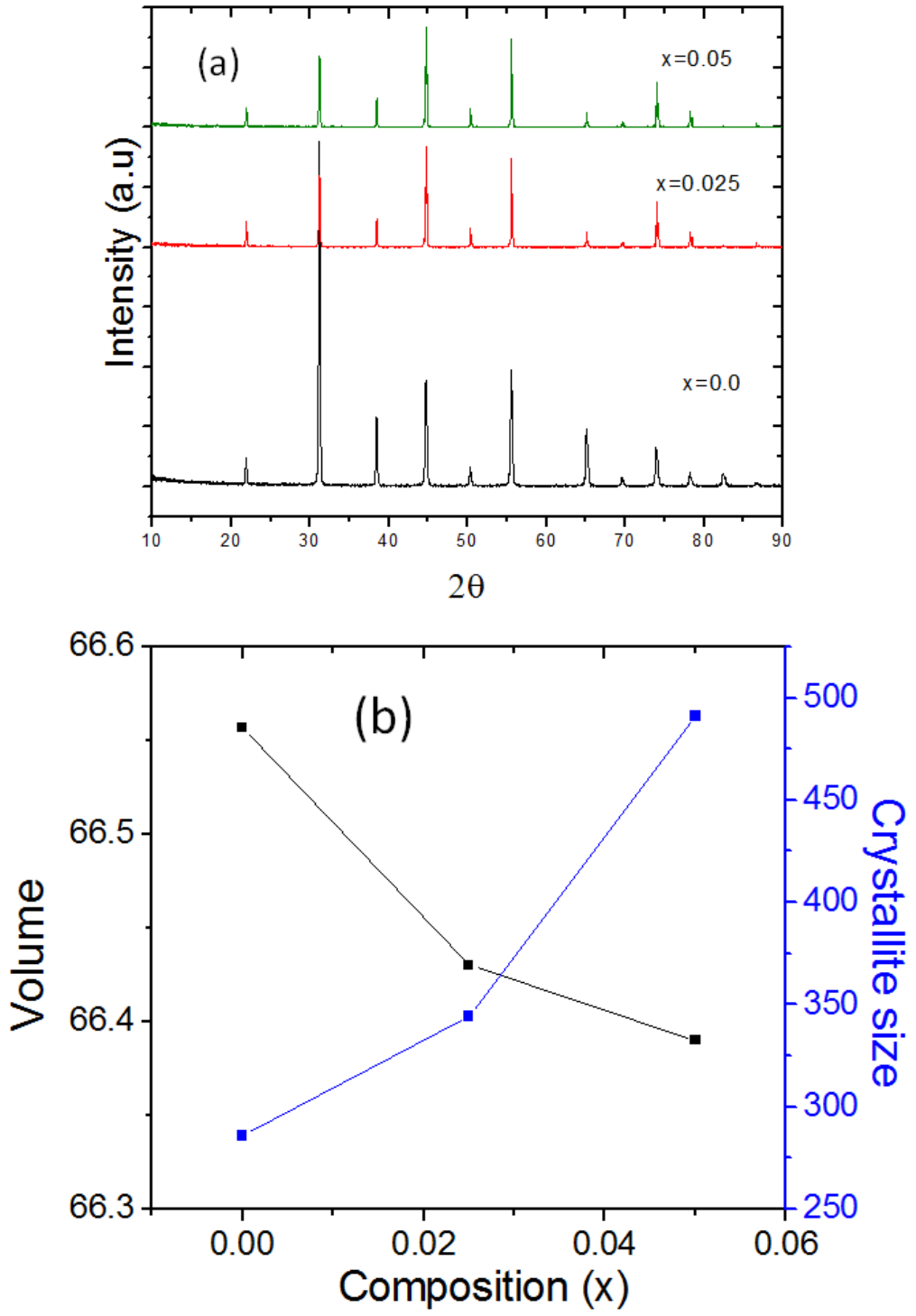

Figure 4.1 **(a)** XRD patterns **(b)** XRD parameters of $Ba_{1-x}Bi_{2x/3}Ti_{0.75}Zr_{0.25}O_3$ Ceramics (x= 0.0, 0.025, 0.05)

Table 4.2 XRD parameters of $Ba_{1-x}Bi_{2x/3}Ti_{0.75}Zr_{0.25}O_3$ ceramics (x= 0.0, 0.025, 0.05)

Composition $Ba_{1-x}Bi_{2x/3}Zr_{0.25}Ti_{0.75}O_3$	2θ (deg)	FWHM (deg)	d-spacing ($Å$)	$a = b = c$ ($Å$)	Volume ($Å^3$)	crystallite size ($Å$)	X-Ray density	Strain
x = 0	31.32	0.288	2.8685	4.0526	66.557	286	6.19	0.451
x=0.025	31.51	0.168	2.8905	4.0500	66.43	491	6.012	0.265
x=0.05	31.91	0.1574	2.8692	4.0492	66.39	525	6.095	0.246

4.4.2 Microstructure

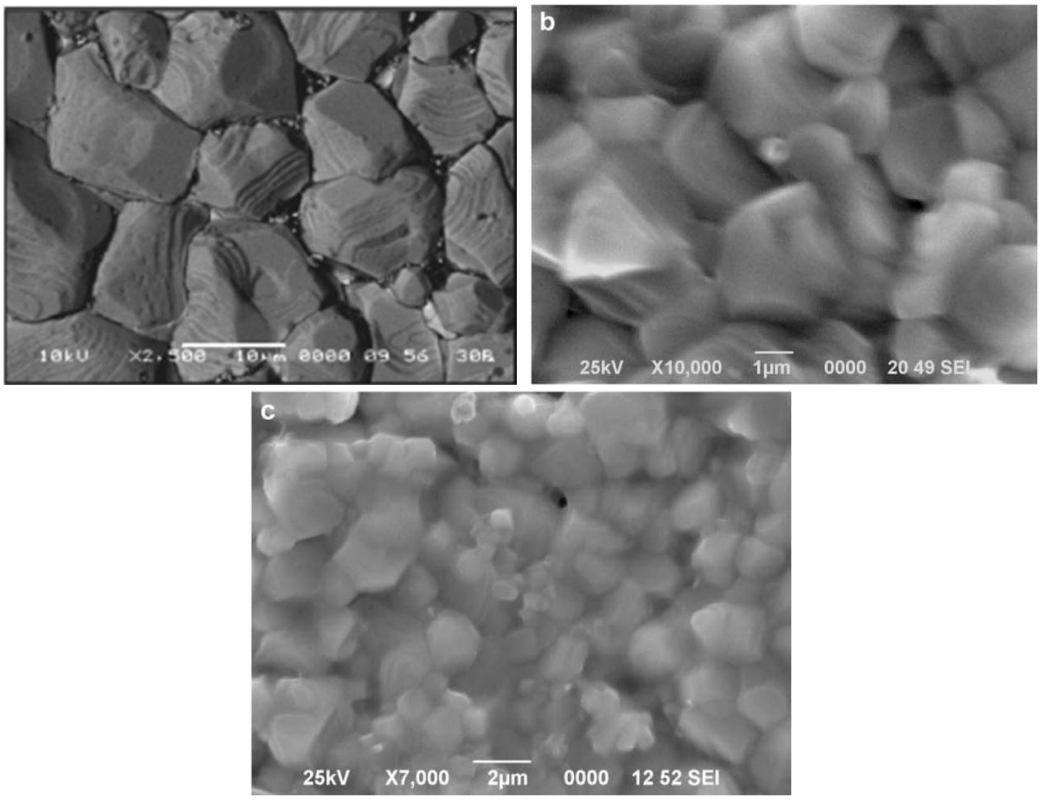

Figure 4.2 Microstructure of $Ba_{1-x}Bi_{2x/3}Ti_{0.75}Zr_{0.25}O_3$ ceramics **(a)** x = 0, **(b)** x = 0.025 and **(c)** x = 0.05

The influence of the Bi ion substitution on the microstructure of $BaZr_{0.25}Ti_{0.75}O_3$ compound is systematically investigated and the results are presented in this section. Figures 4.2 (a-c) shows the microstructures of the Bi^{3+} substituted

$BaZr_{0.25}Ti_{0.75}O_3$ ceramics. The ceramic with 2.5 atom% Bi^{3+} substitution resulted in the microstructure with smaller grain size distribution with irregular shaped grains. The size of grains is found to vary from 1 μm to 3 μm. As the Bi^{3+} substitution amount is increased, the grains are distributed evenly and the grain shape becomes nearly spherical with reduced grain size. All the ceramics have triple point porosity which is commonly observed in solid state oxide mixing route processed ceramic materials.

4.4.3 Dielectric Study

Figure 4.3 shows the temperature dependence of ε' and ε'' for $Ba_{1-x}Bi_{2x/3}Ti_{0.75}Zr_{0.25}O_3$ (x= 0.0, 0.025, 0.05) compositions at 1 *kHz*, 10 *kHz*, 100 *kHz* and 1 *MHz*. The value of ε' increases gradually to a maximum value (ε_m) with increase in temperature and then decreases smoothly indicating a phase transition. The maximum of dielectric permittivity (ε_m) and the corresponding temperature of dielectric permittivity (T_m) depend upon the measurement frequency for all the compositions.

The magnitude of dielectric constant decreases with increase in frequency and the maximum shifts to higher temperature. This indicates that the dielectric polarization is of relaxation type in nature. The dielectric constant of the composition $BaZr_{0.25}Ti_{0.75}O_3$ is higher than those ceramics substituted with heterovalent Bi ion. The results also show that the temperature T_m corresponding to the maximum value of the dielectric permittivity ε_m is decreased with increasing

heterovalent Bi content, implying, Bi substitution in $BaZr_{0.25}Ti_{0.75}O_3$ influences the transition temperature T_m.

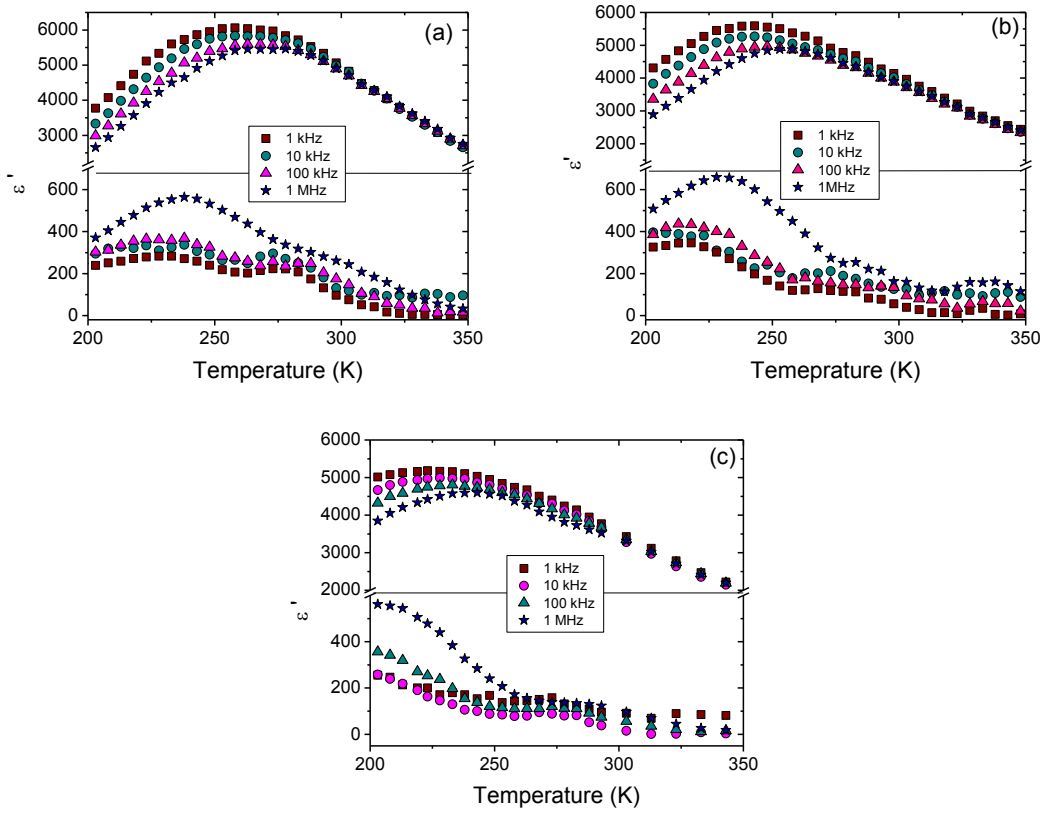

Figure 4.3 Temperature dependency ε' and ε'' of $Ba_{1-x}Bi_{2x/3}Ti_{0.75}Zr_{0.25}O_3$ at various frequencies; **(a)** x = 0.0, **(b)** x = 0.025 and **(c)** x=0.05

The decrease in maximum dielectric constant and transition temperature may be due to the decrease in grain size with increase in Bi content. Figure 4.4 shows the plot of inverse dielectric constant versus temperature at different frequencies. A clear deviation from Curie–Weiss law can be seen in all representative frequency. The parameter obtained at 100 *kHz* is shown in the Table 4.3.

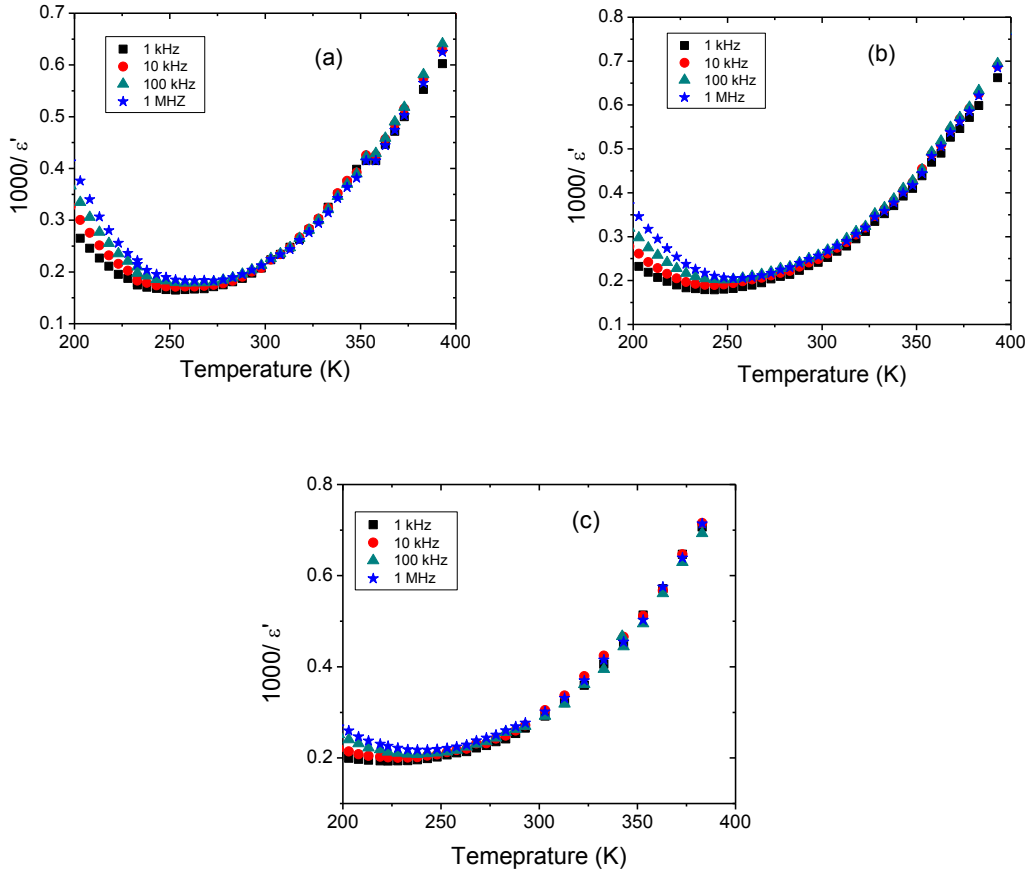

Figure 4.4 Temperature dependency of *1/ε* for $Ba_{1-x}Bi_{2x/3}\ Ti_{0.75}Zr_{0.25}O_3$ at various frequencies **(a)** x=0.0, **(b)** x=0.025, **(c)** x=0.05

Table 4.3 Parameters obtained from temperature dependency dielectric study on the composition $Ba_{1-x}Bi_{2x/3}Ti_{0.75}Zr_{0.25}O_3$ at 100 *kHz*

Parameters	x = 0	x = 0.025	x = 0.05
T_m(K)	273(±1)	257(±1)	238(±1)
T_o(K)	307(±1)	286(±1)	269(±1)
C (10^5 K)	1.54	1.72	2.25
ΔT_m	88(±2)	79(±2)	72(±2)
T_{cw}	361(±2)	337(±2)	310(±2)
ε_m	5572(±3)	4870(±3)	4829(±3)
γ	1.71	1.86	1.98

Figure 4.5 (a) shows the plot of log $(1/\varepsilon' - 1/\varepsilon_m)$ vs. log $(T - T_m)$ at 100 *kHz* for $Ba_{1-x}Bi_{2x/3}Ti_{0.75}Zr_{0.25}O_3$ (x = 0.0, 0.025 and 0.05) composition. Linear relationships are observed. The slopes of the fitting curves of modified curie wises law as explained in chapter 3(equation 3.1) are used to determine the parameter c and γ value. The values of γ and c are given in Table 4.3.

The values of the γ show that the material is highly disordered. The increased value of γ with Bi content indicates the increase in diffusivity. The broadened dielectric maximum (in ε' vs. temperature curve) and its deviation from Curie–Weiss law are the main characteristics of a diffuse phase transition of the material. The diffuse phase transition and deviation from Curie–Weiss type may be assumed due to disordering. Figure 4.5 (b) shows the temperature dependence of the relaxation frequency, plotted as $1/T_m$ vs *ln f.* The symbols are the experimental points and line is corresponding fitting to the Vogel–Fulcher relationship and the best of V-F equation to the experimental data are given in Table 4.4

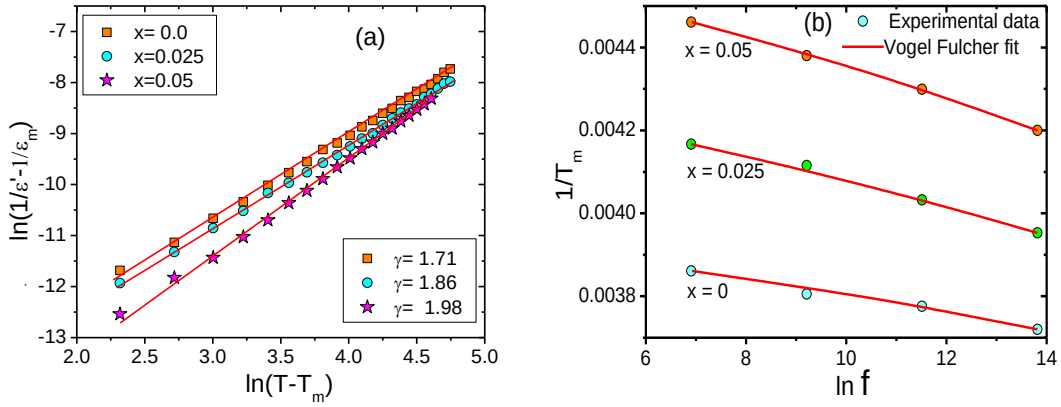

Figure 4.5 **(a)** log $(1/\varepsilon' - 1/\varepsilon_m)$ vs. log $(T - T_m)$ at 100 *kHz* and
(b) Plot of ln *f* as function of T_m for $Ba_{1-x}Bi_{2x/3}Ti_{0.75}Zr_{0.25}O_3$

Table 4.4 Volgel-Fulcher fitting parameters of $Ba_{1-x}Bi_{2x/3}Ti_{0.75}Zr_{0.25}O_3$

Sample	T_f (K)	f_o (Hz)	E_a (eV)
x = 0	207±3	5.915×10^{15}	0.081(3)
x = 0.025	189±3	5.955×10^{17}	0.149(5)
x = 0.05	177±3	1.33×10^{16}	0.122(5)

4.5 Impedance Spectroscopy

The detail studies of impedance spectroscopy of $Ba_{1-x}Bi_{2x/3}Ti_{0.75}Zr_{0.25}O_3$ (x = 0.025) (BBZT) ceramic are discussed.

4.5.1 Measurement of dielectric relaxation versus frequency

The angular frequency ω (=2$\pi\nu$) dependence of the dielectric constant ε' of $Ba_{1-x}Bi_{2x/3}Ti_{0.75}Zr_{0.25}O_3$ (x = 0.025) at various temperatures is shown in Figure 4.6 (a). The nature of the dielectric permittivity for free dipoles oscillating in an alternating field may be described in the following way. At very low frequencies ($\omega \ll 1/\tau$, τ=relaxation time), dipoles follow the field and we have $\varepsilon' = \varepsilon_s$ (value of the dielectric constant at quasistatic fields). As the frequency increases (with $\omega < 1/\tau$), dipoles begin to lag behind the field and ε' slightly decreases. When frequency reaches the characteristic frequency ($\omega = 1/\tau$), the dielectric constant drops (relaxation process). At very high frequencies ($\omega \gg 1/\tau$), dipoles can no longer follow the field and $\varepsilon' \approx \varepsilon_\infty$ (high-frequency value of ε'). Qualitatively this behavior has been observed in Figure 4.6 (a). The dielectric constant at low frequency is rather high, and is found to decrease with frequency at first and then becomes more or less stabilized. The high value of ε' at frequencies lower than 1 *kHz*, which

increases with decreasing frequency and increasing temperature, correspond to bulk effect of the system.

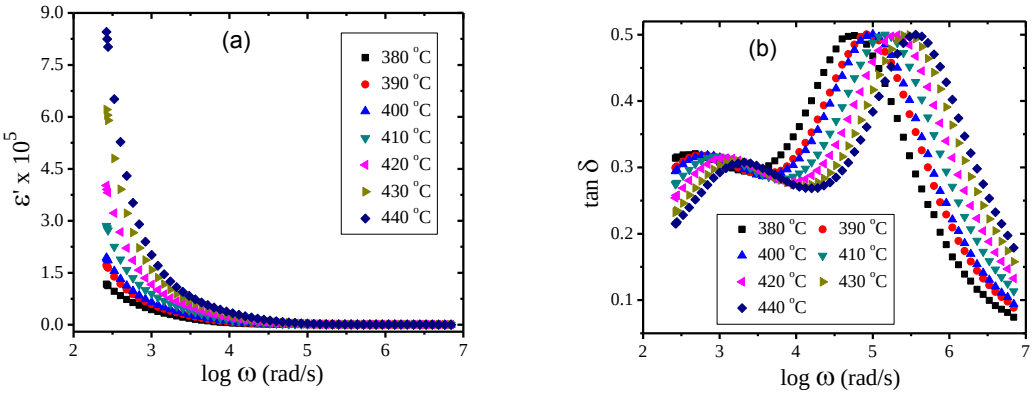

Figure 4.6 Angular frequency dependence of the dielectric constant **(a),** and loss tangent **(b)** at different temperatures of $Ba_{1-x}Bi_{2x/3}Ti_{0.75}Zr_{0.25}O_3$ (x = 0.025) (BBZT) ceramic

Figure 4.6 (b) shows the variation of dielectric loss (tanδ) with frequency at various temperatures. The positions of the peaks apparently shift toward higher frequency with the increase of the peak height when temperature increases. This characteristic indicates that these peaks are associated with a thermally activated relaxation process.

4.5.2 Impedance Study

The complex impedance plot (Figure 4.7) shows depressed semicircular arcs with their centers lying below the real axis rather than on the real axis. The angle by which the semicircle is depressed below the real axis and the amount of inclination of the straight line are related to the width of the distribution of the relaxation time. This suggests the poly-dispersive nature of the sample. Using the ZView commercial software, the impedance data were analyzed in order to obtain the bulk resistance (R_g) and grain boundary resistance (R_{gb}). The observed features

can be modeled by equivalent circuits (as shown in inset Figure 4.7) is given in Table 4.5. The impedance plot comprises two semicircular arcs. The assignment of the two semicircular arcs to the electrical response is due to grain interior and grain boundary *(MacDonald, 1987).* As the temperature increases, the radius of the arc corresponding to the bulk resistance of the sample decreases indicating an activated conduction mechanism. Figure 4.8 (a) shows the variation of grain and grain boundary resistance and Figure 4.8 (b) shows the variation of grain and grain boundary capacitance with varying temperature. The grain and grain boundary resistance decreases with temperature with Arrhenius dependence of the form

$$R = \beta \exp\left({E_a}/{k_B T}\right) \tag{4.1}$$

where, R is the resistance, β is the exponential component, Ea is the activation energy, k_B is the Boltzmann constant and T is the temperature. The experimental data of R_g and R_{gb} were fitted with equation 4.1 and a linear nature is obtained. The activation energy is calculated from the slope and found to be 0.44 eV for grain and 0.54 eV for grain boundary.

Figure 4.9 (a) shows the variation of the real part of impedance (Z') with frequency at various temperatures. The symbol represents the experimental data and the line represents the fitting of equation explained in chapter 3(equation 3.3). It is observed that the magnitude of Z' decreases with the increase in both frequency as well as temperature, indicate an increase in AC conductivity with the rise in temperature and frequency. The Z' values for all temperatures merge above 100 kHz. This may be due to the release of space charges as a result of reduction in the barrier properties of material with the rise in temperature and may be a

responsible factor for the enhancement of AC conductivity of material with temperature at higher frequencies. Further, at low frequencies the *Z'* values decrease with rise in temperature show negative temperature coefficient of resistance (NTCR) type behaviour like that of semiconductors.

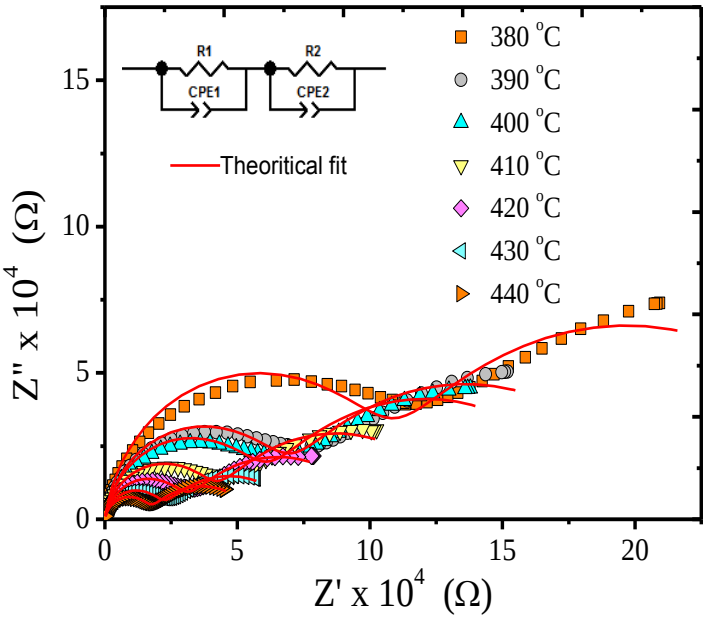

Figure 4.7 Nyquist plot of Complex impedance spectrum of $Ba_{1-x}Bi_{2x/3}Ti_{0.75}Zr_{0.25}O_3$ (x = 0.025) ceramic

Table 4.5 Grain and Grain boundary Resistance and Capacitance from Nyquist plot of $Ba_{1-x}Bi_{2x/3}Ti_{0.75}Zr_{0.25}O_3$ (x = 0.025) ceramic

Temperature ^oC	R_g $K\Omega$	CPE_g nF	R_{gb} $K\Omega$	CPE_{gb} nF
380	102.96	52.6	192.44	0.601
390	64.64	56.4	145.45	0.905
400	56.33	56.6	131.22	0.993
410	38.98	61.3	97.67	0.145
420	28.41	66.0	74.46	0.212
430	20.20	71.3	54.03	0.299
440	15.27	75.7	42.42	0.378

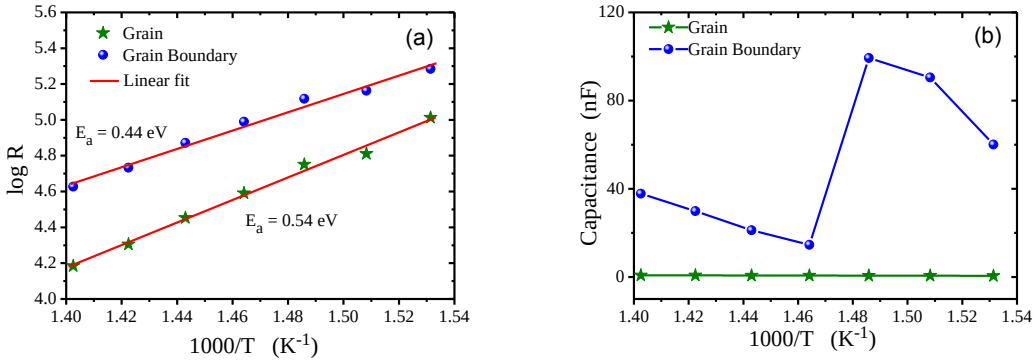

Figure 4.8 **(a)** Arrhenius behavior of Grain and Grain boundary Resistance and **(b)** Temperature dependence of Grain and Grain boundary Capacitance of $Ba_{1-x}Bi_{2x/3}Ti_{0.75}Zr_{0.25}O_3$ (x = 0.025) ceramic

Figure 4.9 (b) shows the variation of the imaginary part of impedance (*Z"*) with frequency at different temperature. The curves show that the *Z"* values reach a maxima peak ($Z"_{max}$) and the value of $Z"_{max}$ shifts to higher frequencies with increasing temperature. A typical peak broadening which is slightly asymmetrical in nature can be observed with the rise in temperature. The broadening of peaks in frequency explicit plots of *Z"* suggests that there is a spread of relaxation times, *i.e.*, the existence of a temperature dependent electrical relaxation phenomenon in the material *(Hosono et al 2001)*. The theoretical maximum frequency and experimental maximum frequency are given in Table 4.6.

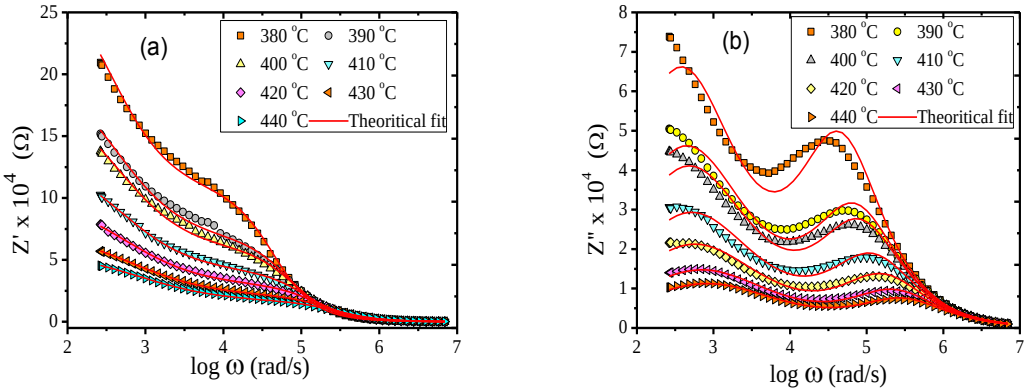

Figure 4.9 Real **(a)** and Imaginary **(b)** part of impedance spectrum with various frequencies at various temperatures of $Ba_{1-x}Bi_{2x/3}Ti_{0.75}Zr_{0.25}O_3$ (x = 0.025) ceramic

Table 4.6 Theoretical and experimental maximum frequency of $Ba_{1-x}Bi_{2x/3}Ti_{0.75}Zr_{0.25}O_3$ (x=0.05) ceramic

Temperature	Experimental data (log)		Calculated data (log)	
^oC	$\omega_{max}1$	$\omega_{max}2$	$\omega_{max}1$	$\omega_{max}2$
380	4.462	--	4.439	--
390	4.706	--	4.557	--
400	4.772	--	4.699	--
410	4.963	2.526	4.864	2.578
420	5.109	2.640	5.044	2.6718
430	5.27	2.778	5.204	2.775
440	5.441	2.887	5.374	2.865

Figure 4.10 shows the plot of scaled $Z''(\omega,T)$ versus log ω [i.e., $Z''(\omega, T)/Z''_{max}$ and $\log(\omega/\omega_{max})$], where ω_{max} corresponds to the peak frequency of the Z'' versus $log\ \omega$ plots. It can be seen that the Z'' data coalesced into a master curve. These observations indicate that the distribution function for relaxation times is nearly temperature independent with non-exponential conductivity relaxation. This phenomenon is well defined by a non-Debye type (polydispersive) relaxation governed by the relation,

$$\varphi(t) = exp\left[-\left(\frac{t}{\tau}\right)^{\beta}\right]; (0 < \beta < 1) \qquad (4.2)$$

where $\varphi(t)$ stands for time evaluation of electric field within sample and β is the Kohlrausch exponent. The smaller value of β indicates larger deviation of relaxation with respect to Debye type relaxation ($\beta = 1$). A non-exponential type relaxation governed by equation (4.2) suggests the possibility of ion migration that takes place via hopping accompanied by a consequential time dependent mobility of other charge carriers of the same type in the vicinity occurs *(Prasad et al 2005)*.

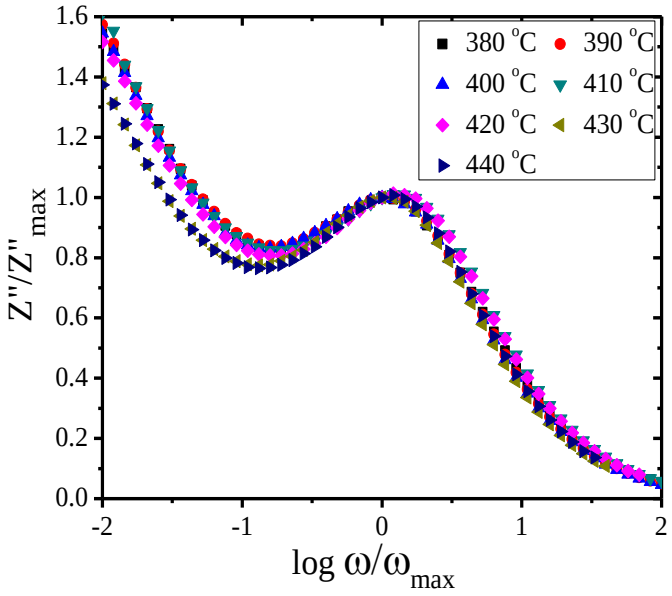

Figure 4.10 Scaling behavior of Imaginary part of Impedance spectrum of $Ba_{1-x}Bi_{2x/3}Ti_{0.75}Zr_{0.25}O_3$ (x = 0.025) ceramic

4.5.3 Modulus Spectroscopy

Figure 4.11 ((a) and (b)) displays the frequency (angular) dependence of *M'(ω)* and *M"(ω)* for $Ba_{1-x}Bi_{2x/3}Ti_{0.75}Zr_{0.25}O_3$ (x = 0.025) as a function of temperature. *M'(ω)* shows a dispersion tending toward M_∞ (the asymptotic value of *M'(ω)* at higher

frequencies (Figure 4.11(a))), while *M"(ω)* exhibits a maximum $M"_{max}$ (Figure 4.11(b)) centered at the dispersion region of *M'(ω).*

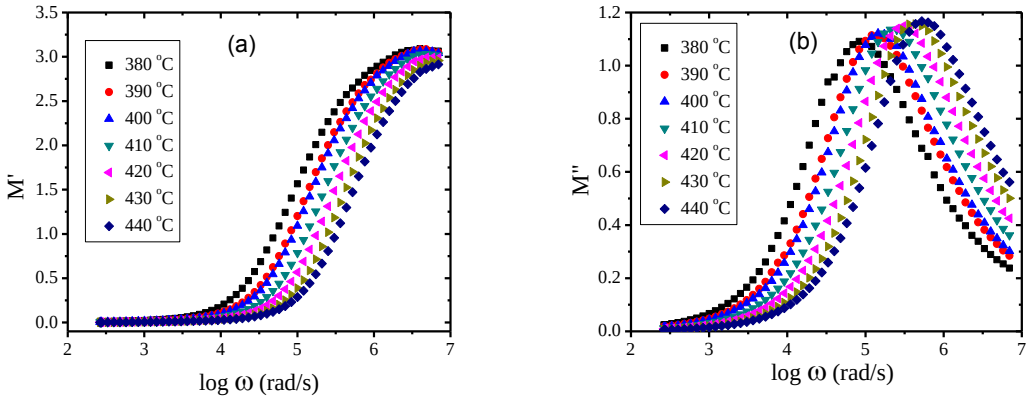

Figure 4.11 Real **(a)** and Imaginary **(b)** part of electric modulus spectrum with various frequencies at various temperatures of $Ba_{1-x}Bi_{2x/3}Ti_{0.75}Zr_{0.25}O_3$ (x = 0.025) ceramic

It may be noted from Figure 4.11(b) that the position of the peak $M"_{max}$ shifts to higher frequencies as the temperature is increased. The asymmetric broadening of the peak indicates the spread of relaxation with different time constant, and relaxation in the material is of non-Debye type. The frequency region below peak maximum *M"* determines the range in which charge carriers are mobile on long distances. At frequency above peak maximum *M"*, the carriers are confined to potential wells, being mobile on short distances. The frequency ω_m (corresponding to $M"_{max}$) gives the most probable relaxation time τ_m.

The most probable relaxation time follows the Arrhenius law, given by

$$\omega_m = \omega_0 \, exp\left(\frac{-E_a}{k_B T}\right) \tag{4.3}$$

where ω_o is the pre-exponential factor and E_a is the activation energy. Figure 4.12 shows a plot of the *log* ω_m versus *1/T*, where the circles are the experimental data

and the solid line is the least-squares straight-line fit. The activation energy E_a calculated from the least-squares fit to the points. From Figure 4.12 it can be seen that the activation energy calculated from Arrhenius relation E_a = 0.50 *eV* for relaxation of *M"* is found to be close to the activation energy E_a = 0.59 *eV* for *Z"*. We have scaled each *M"* by M''_{max} and each frequency by ω_{max} for different temperatures in Figure 4.13 (a). The coincidence of all curves/peaks at different temperatures exhibits temperature independent behavior of the dynamic processes *(Saha et al 2002)* occurring in the material. This might be due to the ion migration that takes place via hopping mechanism.

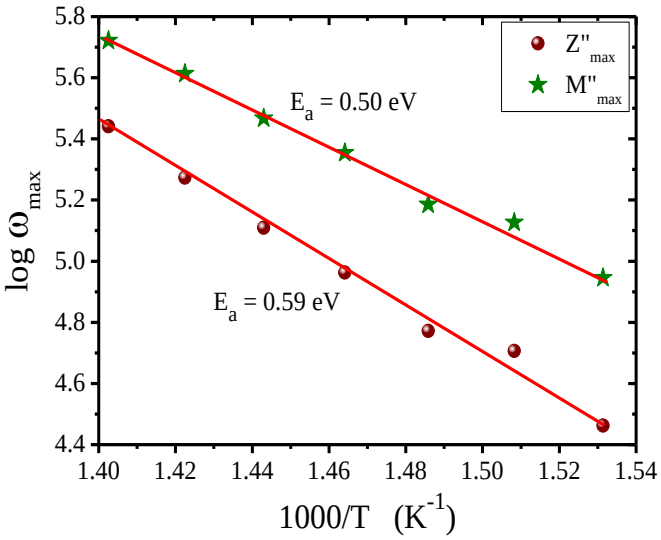

Figure 4.12 Relaxation behavior (Arrhenius plot) of maximum frequency from Imaginary part of Impedance and Electric Modulus spectrum (Relaxation time $\tau = 1/\omega$) of $Ba_{1-x}Bi_{2x/3}Ti_{0.75}Zr_{0.25}O_3$ (x = 0.025) ceramic

Going further in the description of experimental data, the variation of normalized parameters M''/M''_{max} and Z''/Z''_{max} as a function of logarithmic frequency measured at 440^oC for $Ba_{1-x}Bi_{2x/3}Ti_{0.75}Zr_{0.25}O_3$ (x = 0.025) are shown in Figure 4.13 (b). Comparison with the impedance and electrical modulus data allows the

determination of the bulk response in terms of localized, i.e., defect relaxation or non-localized conduction, i.e., ionic or electronic conductivity *(Gerhardt 1994)*.

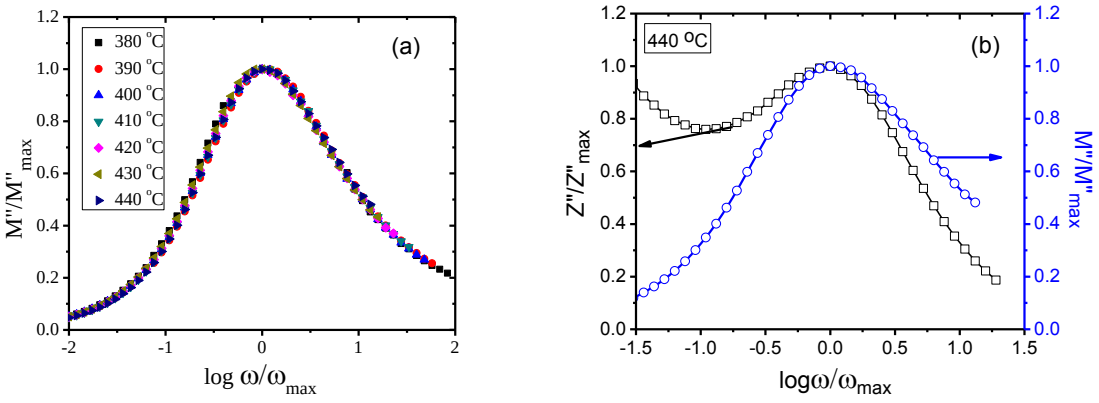

Figure 4.13 **(a)** Scaling behavior of Imaginary part of Electric Modulus spectrum and **(b)**The variation of normalized parameters M''/M''_{max} and Z''/Z''_{max} as a function of log frequency measured at 440 ^oC of $Ba_{1-x}Bi_{2x/3}Ti_{0.75}Zr_{0.25}O_3$ (x = 0.025) ceramic

The Debye model is related to an ideal frequency response of localized relaxation. In reality the nonlocalized process is dominated at low frequencies. In the absence of interfacial effects, the non-localized conductivity is known as the dc conductivity. Thus, the high dielectric loss, *tanδ*, is usually accompanied by rising $\varepsilon'(\omega)$ at low frequencies. It is possible to determine the type of the dielectric response by inspection of the magnitude of overlapping between the peaks of both parameters $Z''(\omega)$ and $M''(\omega)$ *(Gerhardt 1994)*. The overlapping peak position of M''/M''_{max} and Z''/Z''_{max} curves is evidence of delocalized or long-range relaxation *(Gerhardt 1994)*. However, for the present system the M''/M''_{max} and Z''/Z''_{max} peaks overlap but are very close suggesting the components from both long-range and localized relaxation. In order to mobilize the localized electron, the aid of lattice oscillation is required. In these circumstances electrons are considered not to move by themselves but by hopping motion activated by lattice oscillation. In

addition, the magnitude of the activation energy suggests that the carrier transport is due to the hopping conduction.

4.5.4 Conductivity studies

Figure 4.14 shows the variation of ac conductivity as a function of frequency at various temperatures for $Ba_{1-x}Bi_{2x/3}Ti_{0.75}Zr_{0.25}O_3$ (x = 0.025) ceramic. The plot shows conductivity increases with increase of temperature. Frequency independent behavior of the conductivity in the low frequency region is observed but that become sensitive at high frequency region, which generally known as hopping frequency, shifted towards higher frequency side with increase of temperature. In the higher frequency region where the conductivity increases is caused due to the hopping of charge carrier in finite clusters. Frequency independent AC conductivity has been observed in the high temperature indicates the long range movement of mobile charge carriers.

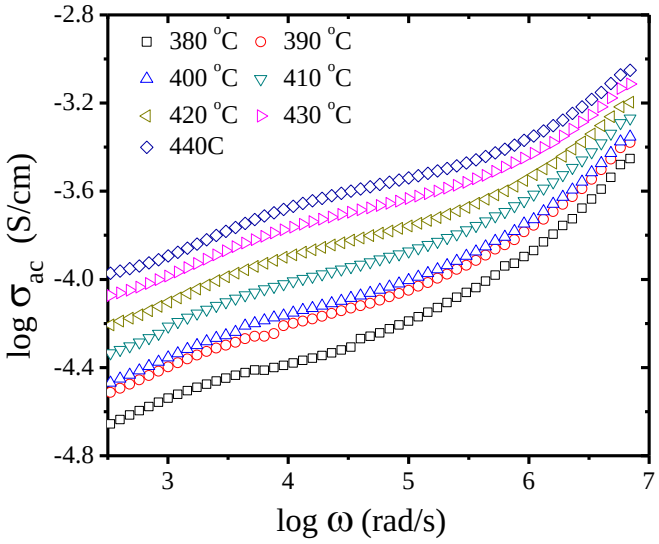

Figure 4.14 Frequency dependence of AC conductivity at various temperatures of $Ba_{1-x}Bi_{2x/3}Ti_{0.75}Zr_{0.25}O_3$ (x = 0.025) ceramic

Using correlated barrier hopping (CBH) model *(Mollah et al 1993)*, the binding energy has been calculated according to the following equation:

$$\beta = \frac{6K_BT}{W_m} \tag{4.4}$$

where, β = *1-n* and W_m is the binding energy, which is defined as the energy required to remove an electron completely from one site to the another site. The characteristic decrease in slope with the rise in temperature is due to the decrease in binding energy as illustrated in the Figure 4.15 (a) (inset). Using the values of the binding energy minimum hopping distance R_{min} is calculated *(Salam 1990)*,

$$R_{min} = \frac{2e^2}{\pi\varepsilon_0\varepsilon W_m} \tag{4.5}$$

where ε_o is the permittivity of free space and ε is the dielectric constant. Figure 4.15 (a) shows the variation of R_{min} with temperature at 100 *KHz*. In the hopping models AC conductivity behavior distinguishes different characteristic region of frequencies. In the low frequency region the constant conductivity shows that the charge transport takes place via infinite percolation path. In the higher frequency region where the conductivity increases the transport is dominated by contribution from hopping in finite clusters.

The AC conductivity data have been used to evaluate the density of states at Fermi level $N(E_f)$ using the relation *(Austin et al 1969)*,

$$\sigma_{AC}(\omega) = \frac{\pi}{3}e^2\omega k_BT\{N(E_f)\}^2\alpha^{-5}\left\{ln\left(\frac{f_o}{\omega}\right)\right\}^4 \tag{4.6}$$

where e is the electronic charge, f_o the photon frequency and α is the localized wave function, assuming f_o =1013 *Hz*, α=1010 m^{-1} at various operating frequencies

and temperatures. Figure 4.15 (b) shows the Frequency dependence of $N(E_f)$ at different temperature. It can be seen that the value of $N(E_f)$ decreases exponentially with the increase in frequency. The reasonably high values of $N(E_f)$ suggests that the hopping between the pairs of sites dominate the mechanism of charge transport in $Ba_{1-x}Bi_{2x/3}Ti_{0.75}Zr_{0.25}O_3$ (x = 0.025).

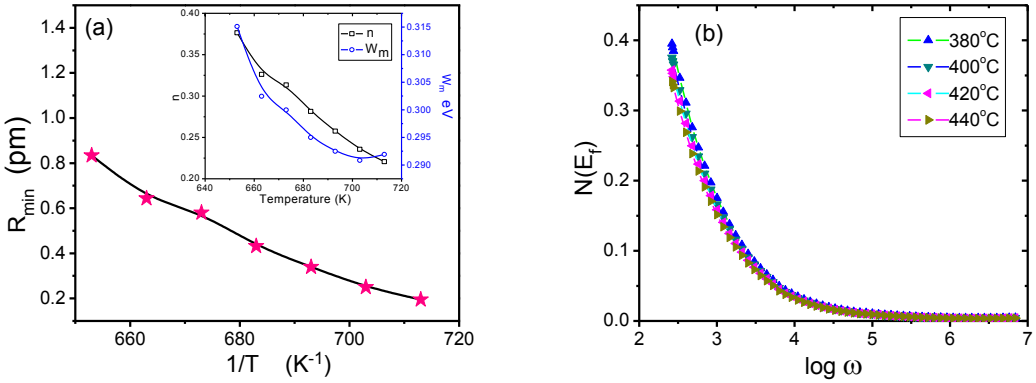

Figure 4.15 **(a)** Variation of Binding energy hopping mechanism (R_{min}) with temperature at 100*Hz* and **(inset)** Variation of Binding Energy and parameter *n* calculated from Jonscher's power law as a function of temperature and **(b)** Frequency dependence of Femi level ($N(E_f)$) at different temperature of $Ba_{1-x}Bi_{2x/3}Ti_{0.75}Zr_{0.25}O_3$ (x = 0.025) ceramic

Figure 4.16 (a) shows the variation of DC conductivity against the temperature. The value of bulk conductivity of the material is evaluated from the complex impedance plots of the sample at different temperatures. At higher temperature, the conductivity versus temperature response is more or less a straight line and can be explained by a thermally activated transport of Arrhenius type.

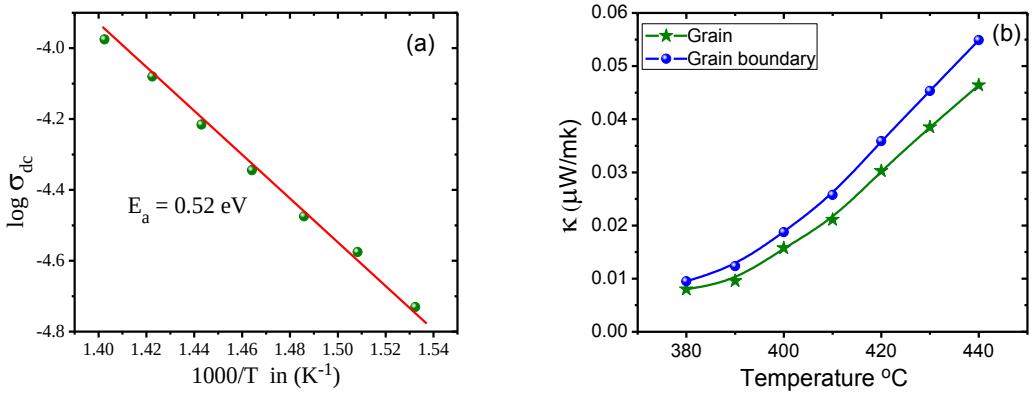

Figure 4.16 **(a)** Temperature dependence of DC conductivity obeys Arrhenius behavior and **(b)** Thermal conductivity behaviour of Grain and Grain boundary of $Ba_{1-x}Bi_{2x/3}Ti_{0.75}Zr_{0.25}O_3$ (x = 0.025) ceramic

At lower temperature, a small deviation from the linear behavior of conductivity has been noticed and can be attributed to Mott's hopping type phenomena *(Mott 1990)*. The DC activation energy of the material has been estimated to 0.52 *eV* in the temperature. The activation energy values for the Electric Modulus (0.50 *eV*) and for DC conductivity (= 0.52 *eV*) are almost identical suggesting a hopping mechanism for $Ba_{1-x}Bi_{2x/3}Ti_{0.75}Zr_{0.25}O_3$ (x = 0.025). This electronic thermal conductivity account for the total thermal conductivity *(E-Abd El-Wahabb 2000)* and is given by:

$$\kappa = L\sigma T\left[1 + \left(\frac{3}{4\pi^2}\right)\left\{\left(\frac{E_a}{k_B T}\right) + 4\right\}^2\right] \qquad (4.7)$$

where L is the Lorentz number. Figure 4.16 (b) shows that the thermal conductivity of grain as well as grain boundary increases with increasing temperature and it exhibits reasonably low thermal conductivity.

In perovskite ferroelectric materials oxygen vacancies are considered to be one of the mobile charge carriers and mostly in titanates, the ionization of oxygen

vacancies create conduction electrons, a process which is defined by Kroger-Ving notation *(Ang et al 2000)*. The excess electron and oxygen vacancies are formed in the reduction reaction, and they may

$$O_O^x \rightarrow \frac{1}{2}O_2 + (V_O^{\bullet}) + 2e^- \quad (4.8)$$

be bond to Ti^{4+} in the form $Ti^{4+} + e^- \leftrightarrow Ti^{3+}$. The formation of oxygen vacancies, can be due to the three different charge states: neutral (V_O^x) state, which it is able to capture two electrons and it is neutral in the lattice, singly ionized ($V_O^{\bullet}$) state and double ionized ($V_O^{\bullet\bullet}$) state, which it is not trap any electron and it is twofold positively, can be thermally activated, thus enhancing the conduction process. Double charge oxygen vacancies ($V_O^{\bullet\bullet}$) are considered to be most mobile charge in perovskite and play important role in conduction. In addition to this the chemical inhomogeneity, may be due to the difference in the ionic environment of Ba^{2+} and Bi^{3+} *(Zhu et al 2007, Simões et al 2007)*.

According to the Schottky barrier model, the grain boundary space charge potential $\Delta\Phi$ is related to the grain boundary and the bulk relaxation times, their ratio is given by *(Balaya et al 2006)*

$$\frac{\tau_{gb}}{\tau_g} = exp(e\Delta\phi/k_BT)/(2e\Delta\phi/k_BT) \quad (4.9)$$

where e is the elementary charge, k_B and T have their usual meanings. The peak of the semicircle allows us to calculate relaxation time with the relation $\omega_m\tau_m=1$. According to this, $\Delta\Phi$ is calculated to be ~0.093 eV by putting all the values in equation 4.13. From the Arrhenius plot above, we can easily find that the value of E_a (*Grain boundary*) – E_a *(Grain)* (from Figure 4.9 (a)) is equal to 0.1 eV, agreeing well with the grain boundary space charge potential $\Delta\Phi$ of 0.093 eV.

From the fitting results above, it is obvious that the activation energies for relaxations and conductivity are different from each other in the selected temperature range. The values of E_{relax} are always slightly higher than E_{cond} obtained from conductivity plots. This character suggests that the relaxation process does not govern the electrical conduction and indicates that the relaxation is a dipolar type. It should be considered that various types of conducting carriers all contribute to the electrical conduction at higher temperature region, although they may be not related to the dielectric relaxation/polarization. For instance, the electrons released from the oxygen vacancy which can be the source of the space charge polarization, are easy to thermally activate and become conducting electrons. Hence, the conductivity energy obtained is lower than the relaxation one. These dipoles related to oxygen vacancies and electrons may be driven to the grain boundaries and would be easily trapped. The grain boundaries thus block the ionic transport across them and then induce the lower electric conductivity than that in the grain. The accumulation of the space charges in the interfaces of the grain boundaries produces the space charge potential of 0.093 *eV*.

CHAPTER 5

INVESTIGATION OF DIELECTRIC PROPERTY AND GLASSY BEHAVIOUR OF DYSPROSIUM SUBSTITUTED $BaZr_{0.25}Ti_{0.75}O_3$ CERAMIC

5.1 Outline of the present study

In the present chapter, the influence of heterovalent Dy^{3+} ions substitution on structural and functional properties in $BaZr_{0.25}Ti_{0.75}O_3$ compound is reported. The samples were prepared by solid state reaction route and followed by characterization like X-Ray Diffraction, Scanning Electron Microscopy, Energy Dispersive X-Ray Spectroscopy, Dielectric, and impedance study. In this chapter we have mainly studied the effect of heterovalent ion on the dielectric behavior and the glassy nature of the samples.

5.2 Sample Preparation

The samples $Ba_{1-x}Dy_{2x/3}Ti_{0.75}Zr_{0.25}O_3$ (x=0.0, 0.01, 0.025, 0.05) were prepared through solid state reaction route. The compositions were prepared from $BaCO_3$ (E. Merck India Ltd.), Dy_2O_3 (Loba Chem., Mumbai), TiO_2 (E. Merck India Ltd.) and ZrO_2 (E. Merck India Ltd). All the chemicals were having more than 99% purity. The raw

powders were thoroughly mixed in agate mortar using IPA. The mixtures were ball milled for 12 hrs in acetone medium for proper mixing of the powder. The homogenous mixtures were calcinied successively at 1350^oC for 6hrs with intermediate mixing and grinding.

5.3 Characterization

The samples are characterized to study there structural and electrical behaviour and the results are discussed.

5.3.1 X- Ray diffraction

Figure 5.1 shows the XRD patterns of $Ba_{1-x}Dy_{2x/3}Ti_{0.75}Zr_{0.25}O_3$ (x = 0, 0.01, 0.025, 0.05) ceramics with different Dy content. The pattern shows that the compositions are of single phase cubic perovskite structure without the evidence of any additional phase. This indicates, Dy forms complete solid solution with $BaTi_{0.75}Zr_{0.25}O_3$ (BZT) in the studied composition range. There is a small shift towards the right in the X-ray diffraction patterns as the Dy content is increased. The increase in 2θ values is as expected because the ionic size of the $Dy^{3+}$is smaller than Ba^{2+}. Initially it is expected that Dy^{3+} substitutes both at Ba^{2+} and Ti^{4+} sites, as most of the rare earth ions do, in $BaTiO_3$. However, XRD study on the Dy substituted $BaTi_{0.75}Zr_{0.25}O_3$ has shown that all the Dy^{3+} goes in to Ba^{2+}.

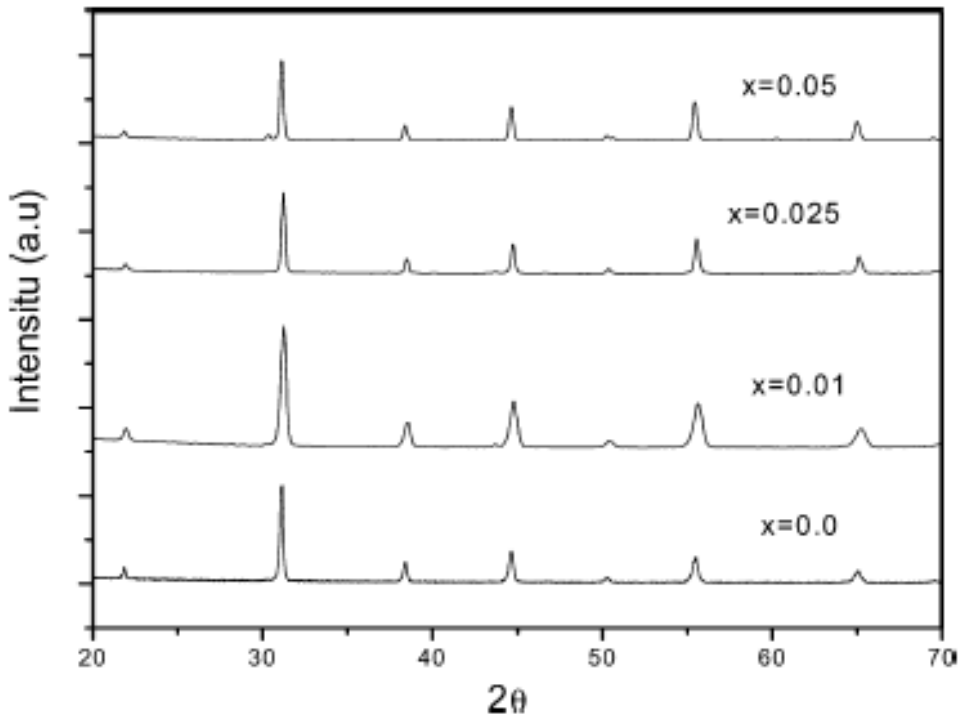

Figure5.1 The XRD pattern of $Ba_{1-x}Dy_{2x/3}Ti_{0.75}Zr_{0.25}O_3$ ceramics

5.3.2 Compaction and sintering

All the substituted $BaZr_{0.25}Ti_{0.75}O_3$ powders were compacted with the parameters optimized for the compaction of $BaZr_{0.25}Ti_{0.75}O_3$ powders prepared using solid state mixed oxide route. This is because of expected similarity in the size and morphological characteristics of powders due to the identical preparation routes. All the green compacts were sintered at different temperatures and the optimized sintering temperature was found to be 1450^oC for 4hrs. The density of the substituted $BaZr_{0.25}Ti_{0.75}O_3$ compounds did not vary significantly with the amount of substituent for a sintering temperature and sintering duration. Hence, all the substituted compounds were sintered at 1450^oC for 4 hrs. Electroding was done (as explained in chapter 2) for electrical measurement.

5.3.3 Compositional Stoichiometry

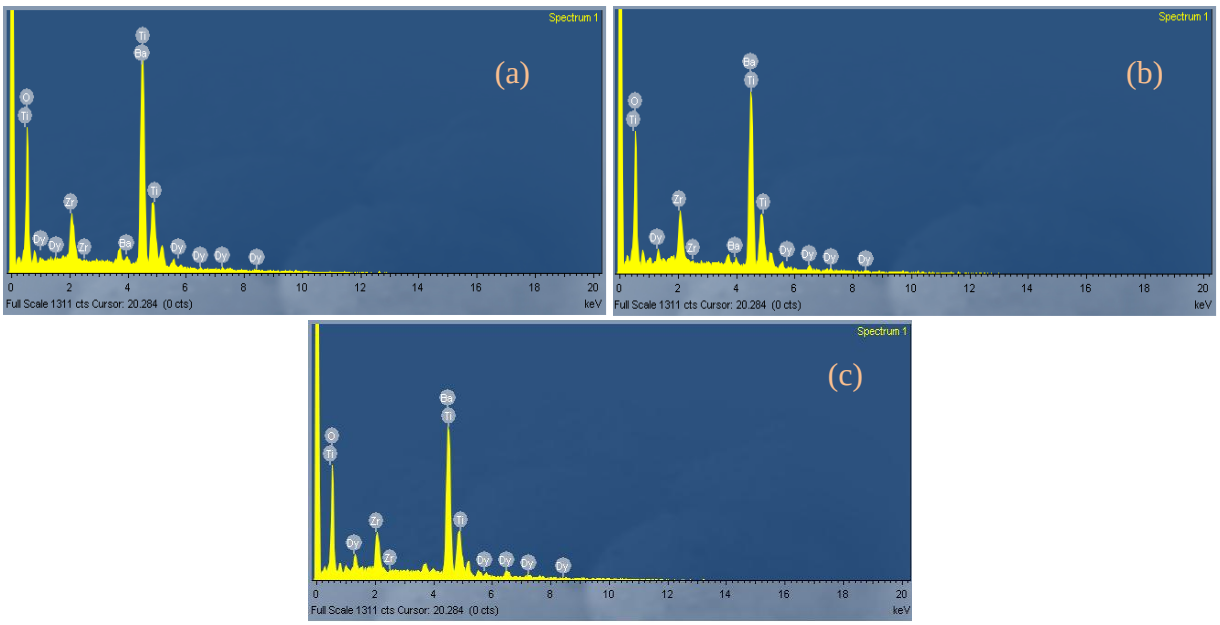

Figure 5.2 Energy Dispersive X-Ray Spectroscopy compositional patterns of the Dy doped $BaTi_{0.75}Zr_{0.25}O_3$ ceramics. **(a)** x = 0.01, **(b)** x = 0.025 and **(c)** x = 0.05

The compositional characterization of substituted Dy doped $BaZr_{0.25}Ti_{0.75}O_3$ powders was done using Energy Dispersive X-Ray Spectroscopy analysis. Figures 5.2 shows the Energy Dispersive X-Ray Spectroscopy compositional patterns of the Dy substituted $BaTi_{0.75}Zr_{0.25}O_3$ ceramics and their corresponding Energy Dispersive X-Ray Spectroscopy derived compositions are given in Table 5.1. From these figures it can be seen that the substituent is within the compound, without any loss either during the processing or during the sintering of the substituted $BaTi_{0.75}Zr_{0.25}O_3$ ceramic. The small deviations from the calculated compositions could be explained by considering the loss of oxygen during the sintering of these compounds at such high temperatures (1450^oC).

Table 5.1 Compositional analysis of $Ba_{1-x}Dy_{2x/3}Zr_{0.25}Ti_{0.75}O_3$ ceramics from Energy Dispersive X-Ray Spectroscopy

Composition	Element	Wt % Calculated	Wt% from EDAX
$BaZr_{0.25}Ti_{0.75}O_3$ x=0.0	Ba	55.87	55.91
	Zr	9.46	9.66
	Ti	15.01	14.94
	O	19.66	19.49
$Ba_{1-x}Dy_{2x\backslash 3}Zr_{0.25}Ti_{0.75}O_3$ x=0.01	Ba	55.77	55.90
	Dy	0.47	0.42
	Zr	9.35	9.16
	Ti	14.72	14.99
	O	19.69	19.53
$Ba_{1-x}Dy_{2x\backslash 3}Zr_{0.25}Ti_{0.75}O_3$ x=0.025	Ba	55.03	55.15
	Dy	1.13	1.55
	Zr	9.37	9.10
	Ti	14.75	14.82
	O	19.72	19.38
$Ba_{1-x}Dy_{2x\backslash 3}Zr_{0.25}Ti_{0.75}O_3$ x=0.05	Ba	53.78	53.10
	Dy	2.23	2.85
	Zr	9.42	9.49
	Ti	14.79	15.04
	O	19.78	19.52

5.3.4 Microstructure

The effect of substitution of heterovalent ion Dy^{3+} (x = 0.01, 0.025 and 0.05) on the microstructure of the $BaTi_{0.75}Zr_{0.25}O_3$ceramic is shown in Figures 5.3. Secondary electron images of the thermally etched surfaces indicated a uniform morphology consisting of smooth, rounded grains with no evidence of any secondary inter-granular phases. All the compositions (x = 0.01, 0.025 and 0.05) of Dy^{3+} substituted $BaTi_{0.75}Zr_{0.25}O_3$) displayed similar morphology and grain size distribution. A decrease in the grain size is observed with increase in Dy^{3+} content. It can also be observed that Dy^{3+} substitution resulted in drastically modified microstructure of $BaTi_{0.75}Zr_{0.25}O_3$ compound. The grain size of the $BaTi_{0.75}Zr_{0.25}O_3$ ceramic is

significantly reduced from ~ 10 μm in $BaTi_{0.75}Zr_{0.25}O_3$ ceramic to 2-5 μm in the Dy^{3+} substituted $BaTi_{0.75}Zr_{0.25}O_3$ ceramic. It is reported that substitution of heterovalent rare earth in $BaTiO_3$ significantly refined the grain size by the formation of an intermediate phase which inhibits the grain growth *(Park et al 2009)*. This also prevented proper sintering of the samples. This is because the dominant mechanism during sintering is diffusion leading to grain growth in ceramic materials. Because the grain growth is inhibited and diffusion is slowed down, the densification of the ceramic becomes difficult and the resultant microstructure is high in pores. The maximum densities achieved even after sintering at 1450^oC for 4hrs is in the range of 96% to 98% of theoretical density of the ceramic. It is also reported that rare earth doping in $BaTiO_3$ reduced the sinterability of $BaTiO_3$ and resulted in low dense ceramics. All the ceramics have triple point porosity.

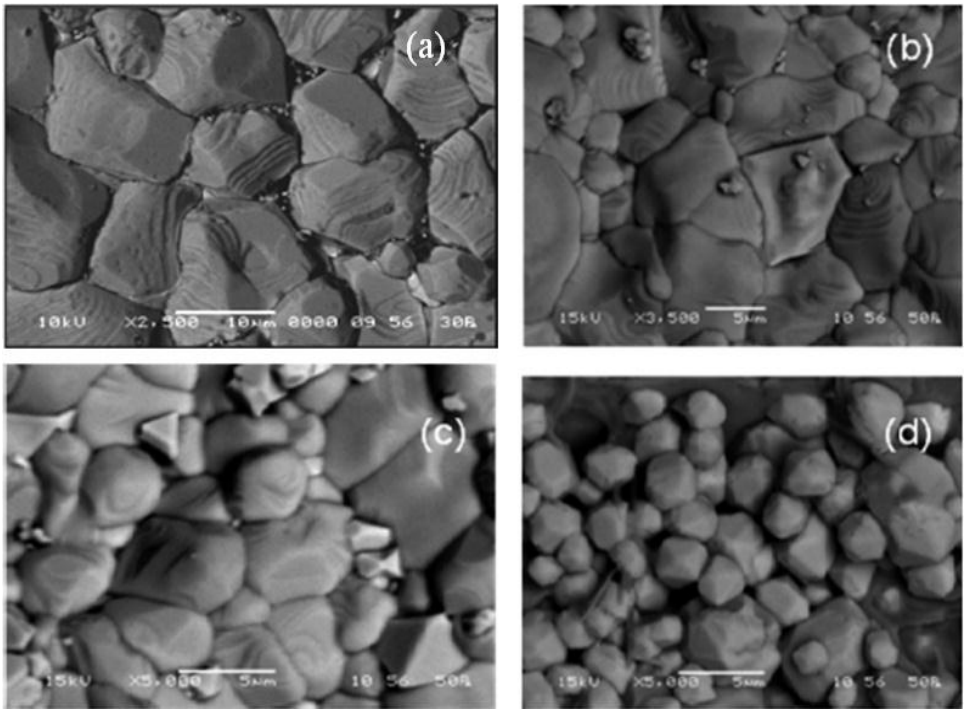

Figure 5.3 Microstructures of $Ba_{1-x}Dy_{2x/3}Ti_{0.75}Zr_{0.25}O_3$ceramics
(a) x=0.0 **(b)** x=0.01 **(c)** x=0.025 **(d)** x=0.05

5.3.5 Dielectric study

Figure 5.4 shows the temperature dependency of the dielectric constant and dielectric loss of $Ba_{1-x}Dy_{2x/3}Ti_{0.75}Zr_{0.25}O_3$ (x = 0.0, 0.01, 0.025 and 0.05) ceramics at different frequency. The figure shows, the value of ε_m increases gradually to a maximum value (ε_m) with increase in temperature up to the transition temperature and then decreases smoothly indicating a phase transition.

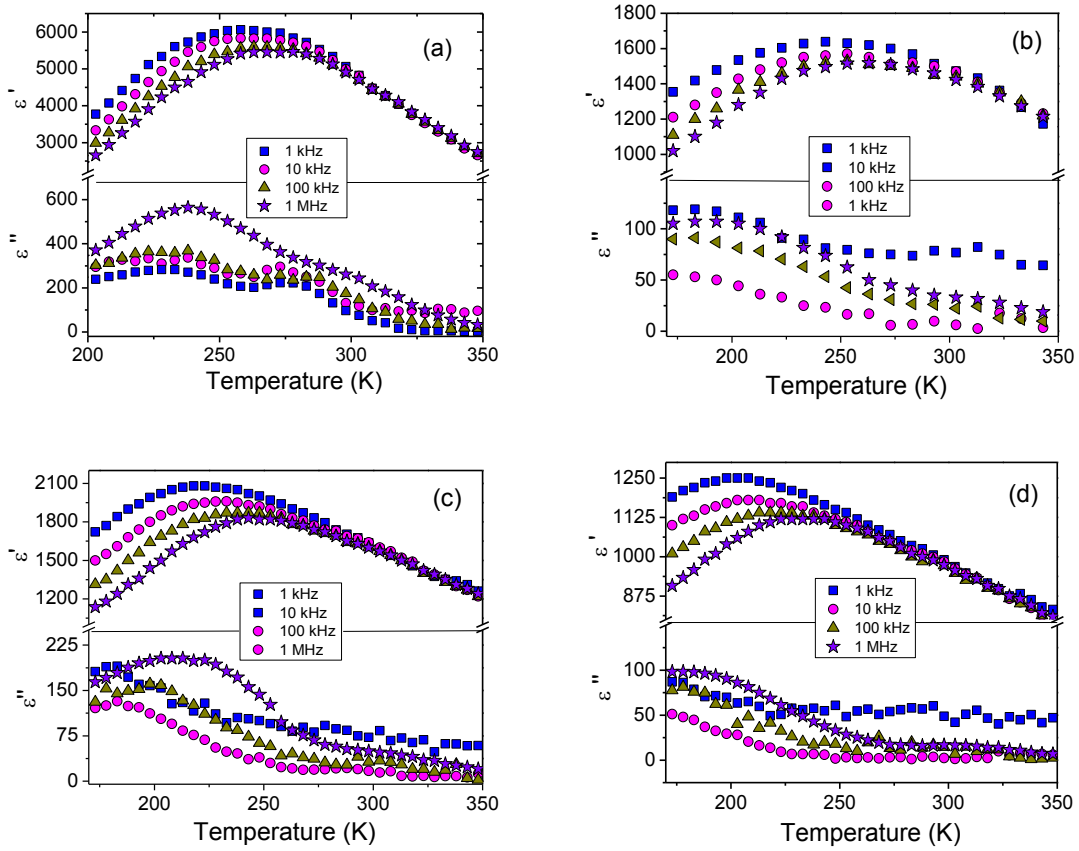

Figure 5.4 Temperature dependency ε' and ε'' of $Ba_{1-x}Dy_{2x/3}Ti_{0.75}Zr_{0.25}O_3$ at various frequencies; **(a)** x = 0.0, **(b)** x = 0.01, **(c)** x = 0.025, **(d)** x = 0.05.

The maximum of dielectric permittivity, ε_m and the corresponding temperature maximum T_m, depends upon the measurement frequency for all the compositions. The magnitude of dielectric constant decreases with increase in frequency and the

maxima is shifting to higher temperature. As shown in the figures, the dielectric loss values of the ferroelectric phase were reduced substantially at room temperature in the paraelectric phase (above T_m). The observed lower temperature (below T_m) frequency dispersion may also have some contribution from the space charge effect.

The high value of dielectric loss at 1 kHz is due to the presence of all types of polarization and may be due to the contribution from the finite resistivity of the materials. An increase in the values of ε_m at lower temperature region may also be due to the increase in ionic conductivity resulting from the disordering of mobile cations in the oxygen octahedral skeleton *(Martirena et al 1974)*. The spectrums show there is an increase in dielectric loss peak temperature with increase in frequency. This indicates that the dielectric polarization is of relaxation type in nature such as dipolar glasses.

In analogy with spin glasses, such a behavior of the dynamic susceptibility in disordered ferroelectric is supposed to be concerned with the existence of the broad spectrum of relaxation times. It is generally considered that the Debye model is based on the assumption of a single relaxation time. The model fails because of the existence of a distribution of relaxation times. Such a distribution of relaxation time implies that the local environment seen by individual dipoles differs from site to site. As a rule, this relaxation occurs in disorder ionic structures, particularly in solid solution. Within the curie range of temperature, dielectric permittivity achieves very high value and displays very large dispersion, which is reminiscent of that found for orientational glasses *(Weber et al 2001)*. It can be also noticed from the figures, that the transition temperatures (T_m) are also shifting towards low temperature with increase in Dy content. This decrease in the Curie temperature can be explained on

the basis of modified Landau–Ginzburg–Devonshire (LGD) phenomenological theory, which is described by the following equation: $T_c/T_{c0} = (1 - K)/D$, where K is the material constant ($K = 2S_oD_o/3R$), T_c is the size dependent Curie temperature, D is the crystal diameter, S_o is the transition entropy, D_o is the critical particle size where the ferroelectric phase does not exist and R is the ideal gas constant. It is reported *(Tang et al 2004)* as the grain size decreases, the maximum dielectric constant and transition temperature decreases. The effect of grain size originates from the higher surface tension in smaller grains *(Uchono et al 1989)*, which acts in the same manner as hydrostatic pressure thus decreasing the Curie point *(Samara 1966)*. In addition the force experienced by the atoms and ions in the vicinity of, or far from, the surfaces of grains are not similar. These considerations suggest that a quadraticity gradient may exist between the surface and the bulk of grains. For smaller grain sizes however, the superficial layers of the grains represent a significant fraction and may dominant the structural and the dielectric measurement. The diffuse nature of the transition in the case of ferroelectric ceramics is usually attributed to a distribution of grain sizes and/or to a gradient of quadraticity which lead to a distribution of transition temperature. Here the observed decrease in transition temperature may be due to the decrease in grain size.

Modified Curie–Weiss law (equation 3.1) has been proposed by many research groups to describe the diffuseness of a phase transition. The plot of log $(1/\varepsilon'-1/\varepsilon_m)$ vs log $(T-T_m)$ at 100 *kHz* for composition is shown in Figure 5.5. Linear relationships are observed. The values of the γ show that the material is highly disordered. The increased value of γ with Dy content indicates the increase in diffusivity. The diffuse

phase transition and deviation from Curie–Weiss type may be assumed due to disordering. The broadness or diffusiveness occurs mainly due to compositional fluctuation and structural disordering in the arrangement of cation in one or more crystallographic sites of the structure. This suggests a microscopic heterogeneity in the compound with different local Curie points. The nature of the variation of dielectric constant and non polar space group suggests that the material may have ferroelectric phase transition.

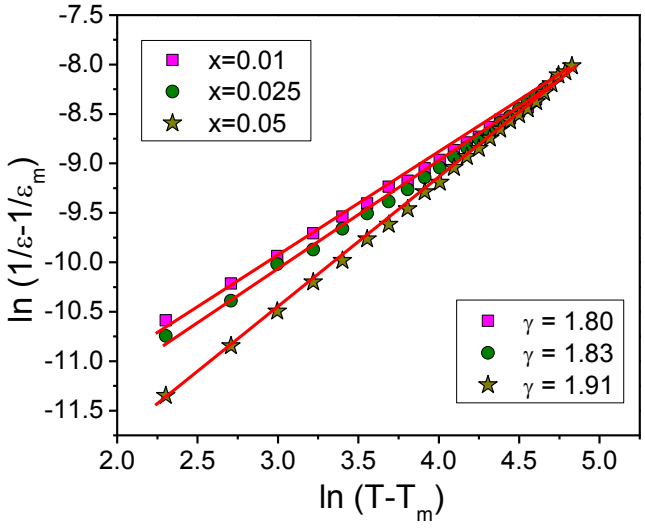

Figure 5.5 log $(1/\varepsilon - 1/\varepsilon_m)$ vs log $(T - T_m)$ plots of $Ba_{1-x}Dy_{2x/3}Ti_{0.75}Zr_{0.25}O_3$ at 100 *kHz*

In the studied compositions of solid solutions $Ba_{1-x}Dy_xTi_{0.75}Zr_{0.25}O_3$, Ba and Dy ions occupy the A-sites of the ABO_3 perovskite structure and Zr and Ti ions occupy the B-site. As previously mentioned both Ti and Zr are ferroelectrically active and these cations are off-centered in the octahedral site, gives rise to a local dipolar moment *(Uchono et al 1989)*. In perovskite type compounds, the relaxor behavior appears when at least two cations occupy the same crystallographic site A or B. The ionic radius of Zr^{4+} (0.98 *Å*) is larger than that of Ti^{4+} (0.72 *Å*). Therefore, an inhomogeneous distribution results at the B-site of the structure. A cationic disorder

induced by B-site substitution is always regarded as the main derivation of relaxor behavior. However, according to our present results, it implies that the observed higher relaxation strength should attribute to a cationic disorder induced by both A-site and B-site substitutions. The different effects of A-site substitution on cation ordering and the stability of the polar region are considered to be based on the polarizability of cations and the tolerance factor of the perovskite structure. For perovskites with the general formula of ABO_3, the following equation can be used to calculate the tolerance factor (t) *(Guo et al 2004)*,

$$t = (R_A + R_O)/\sqrt{2}\,(R_B + R_O) \qquad (5.1)$$

where R_A is the radius of A-site atom, R_B the radius of B-site atom and R_O is the radius of O atom. As the t increases, the normal ferroelectric phase becomes stabilized. So Ba^{2+}cations can stabilize the normal ferroelectrics due to the larger ionic diameter and the higher polarizability. While Dy cations in A-sites behave as a typical destabilizer against normal ferroelectrics and induces paraelectric behavior due to smaller ionic diameter and lower polarization. In this case, more macrodomains (long-range ordered regions) in Dy substituted ceramics will breakup into micropolar regions than that in pure BTZ ceramics. A cationic disorder induced by B-site substitution is always regarded as the main derivation of relaxor behavior. However, the occurrence of relaxation in Dy substituted barium Zirconium titanate should been attributed to the existence of a nano-polar region. The replacements of Ba^{2+} by Dy^{3+} ions leads to the formation of dipolar impurities and defects that have a profound influence on the static and dynamic properties of this material. In $BaTi_{0.75}Zr_{0.25}O_3$ ceramic, the dipolar entities form polar nanodomains and these domains can interact leading to complex relaxational behavior. The

quantitative characterization and comparison of the relaxor behavior based on empirical parameters confirm this. The observed high value of γ and relaxation strength are may be due to the large difference in ionic radius of Ba^{2+} (2.78 Å) and Dy^{3+} (1.75 Å) at the A-site of the perovskite structure.

5.3.6 Investigation of glassy nature in $Ba_{1-x}Dy_{2x/3}(Zr_{0.25}Ti_{0.75})O_3$ relaxors

In the previous section, it has been observed that $Ba_{1-x}Dy_{2x/3}(Zr_{0.25}Ti_{0.75})O_3$ (BDZT) ceramic behaves as a strong relaxor ferroelectrics. It is widely accepted that the behavior of polar region in the material is a key to the behavior of the Relaxor Ferroelectric (RFE) *(Yao et al., 1983; Cross, 1987; Randall and Bhalla, 1990; Cheng et al., 1996)*. Therefore, it will be interesting to study the behavior of the polar regions in the present material. In this context, this section aims to study the glassy nature of the $Ba_{1-x}Dy_{2x/3}(Zr_{0.25}Ti_{0.75})O_3$ relaxor using some theoretical models (Debye and V-F law). The temperature dependence of the dielectric constant and the frequency dependence of the dielectric constant of the REFs at temperatures higher than T_m as well as lower than T_m have been analyzed using *Cheng's model (1996, 1997)*.

5.3.6.1 Frequency dependence of T_m

The polar micro regions are suggested to be thermally unstable and flip in all possible directions *(Cross, 1987)*. Consequently Debye relation should govern the frequency dependence of the T_m. The experimental results of T_m for all the samples

at different frequencies are given in Table 5.2 (a). For the Debye medium, the relation between and T_m can be described by the following the equation

$$\omega = \omega_o \exp\left(-\frac{T_o}{T_m}\right) \tag{5.2}$$

where, ω is the applied or probing frequency, ω_o is the attempt frequency of a dipole or Debye frequency. T_o is the equivalent temperature of activation energy for the relaxation process. The experimental data are fitted to the above equation (Figure. 5.6) and the fitting parameters are given in Table 5.2 (b).

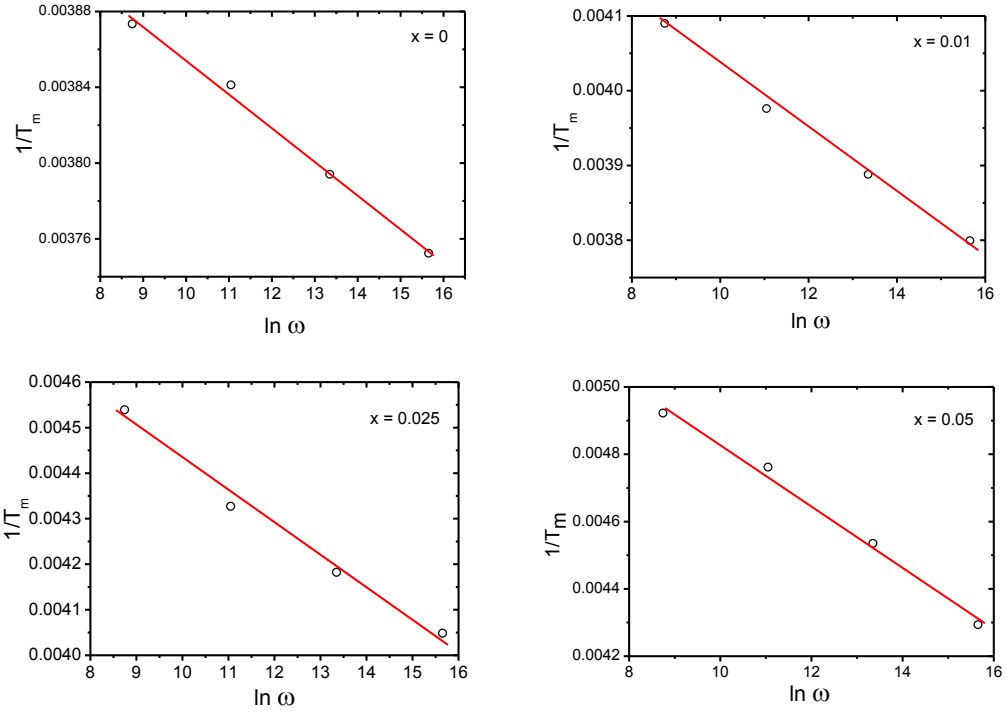

Figure 5.6 The fittings to the Debye relation of $Ba_{1-x}Dy_{2x/3}(Zr_{0.25}Ti_{0.75})O_3$

To analyze the frequency dependence of T_m, one can use Vogel-Fulcher law, which is given by:

$$\omega = \omega_o \exp\left(-\frac{T_o}{T_m - T_f}\right) \tag{5.3}$$

Where T_f is the freezing temperature of the polar regions in the material. The fitting curves are shown in Figure 5.7 and the fitting parameters ω_o, T_o and T_f are given in

Table 5.3. For all the compounds studied, the T_o values (temperature equivalent activation energies) for all the compositions are high and erroneous for a thermally activated system. This indicates that all the polar clusters in these systems do not freeze at the same temperature rather a range of temperatures. Similar contradiction has also been observed by *Cheng et al (1996)*.

Table 5.2 **(a)** Frequency dependence of T_m and **(b)** T_o and ω_o from the fitting parameters of Debye relation for $Ba_{1-x}Dy_{2x/3}(Zr_{0.25}Ti_{0.75})O_3$ relaxors

a)

Frequency	T_m (K)			
	x = 0	x = 0.01	x = 0.025	x = 0.05
1 KHz	258(±1)	244(±1)	218(±1)	203(±1)
10 KHz	263(±1)	251(±1)	226(±1)	210(±1)
100 KHz	273(±1)	257(±1)	237(±1)	220(±1)
1 MHz	283(±1)	263(±1)	248(±1)	232(±1)

b)

Sample	ω_o	T_o
x = 0	5.895×10^{97}	5.58×10^{4}
x = 0.01	1.9×10^{52}	2.7×10^{4}
x = 0.025	2.48×10^{31}	1.4×10^{4}
x = 0.05	1.025×10^{27}	1.08×10^{4}

The pre-exponential factor ω_o gives an idea about the size and the degree of interaction between the polar clusters in RFEs. Larger the size of the polar clusters, stronger the interaction between them and hence smaller is the value of ω_o. Thus, the dielectric behavior of RFEs below T_m may be governed by the rate of growth of

polar clusters with temperature. Therefore, it is essential to study the dielectric behavior at temperatures much higher and lower than that of T_m to visualize the relaxation mechanism in the present system.

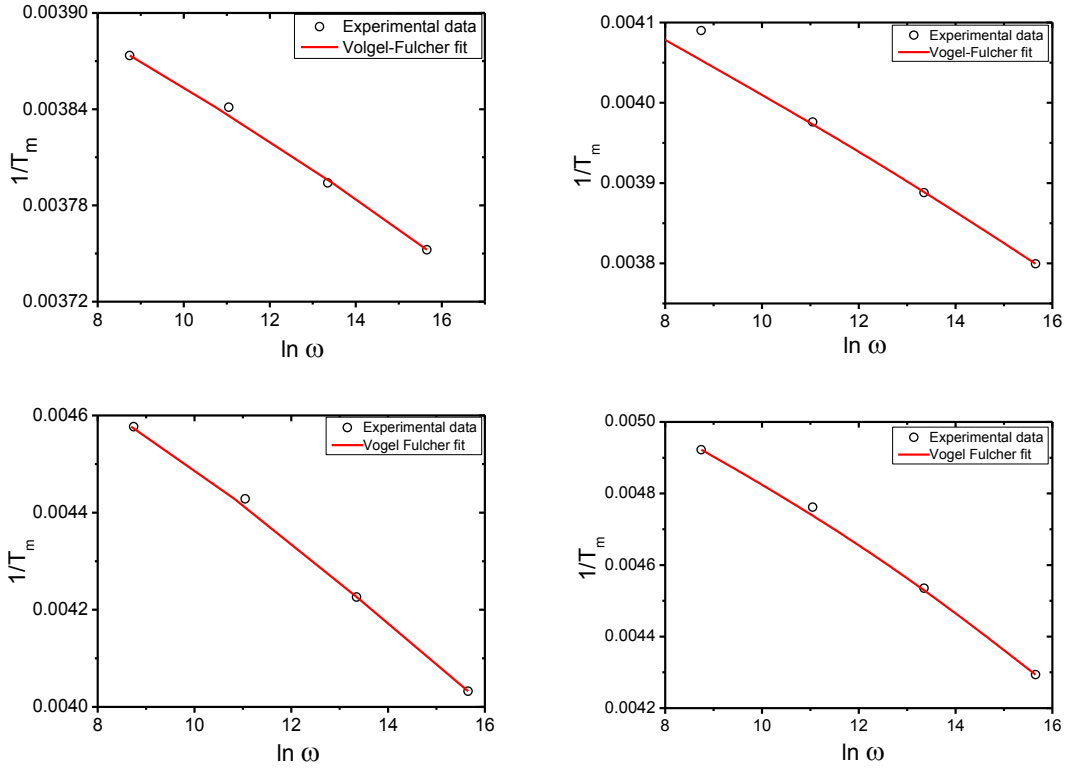

Figure 5.7 The frequency dependence T_m fit to V- F law. The line represents the fitting curve of $Ba_{1-x}Dy_{2x/3}(Zr_{0.25}Ti_{0.75})O_3$

Table 5.3 The values of ω_o, T_o and T_f from Debye and V-F law

Sample	ω_o (Hz)	T_o (K)	T_f (K)
x = 0	3.84 x 10^{25}	2617(±1)	207(±1)
x = 0.01	1.58 x 10^{24}	4503(±1)	150(±1)
x = 0.025	3.18 x 10^{21}	5857(±1)	142(±1)
x = 0.05	5.04 x 10^{13}	1563(±1)	134(±1)

5.3.6.2 Dielectric behavior above T_m

The dielectric behavior at temperature much higher than T_m is investigated through the exponential relation proposed by *Cheng et al (1996, 1997)* which is given below

$$\varepsilon_H(T) = \varepsilon_\infty + exp(\alpha_H - \beta_H T) \quad (5.4)$$

where, α_H (>0) and β_H (>0) are constants and ε_H is the dielectric constant at high temperature. From the dielectric theory, ε_H should be the static dielectric constant and is associated with the dipole moment of the polar regions in the materials. ε_H is generally much higher than that of ε_∞, so the above relation can be expressed as

$$\varepsilon_H(T) \approx exp(\alpha_H - \beta_H T) \quad (5.5)$$

The experimental data have been fitted to the equation. 5.5 (Figure. 5.8) and the fitting parameters are listed in Table 5.4. The value of α_H is associated with the highest possible concentration of the polar regions while β_H is associated with the production rate of the polar regions with decreasing temperature.

Table 5.4 The values of α_H and β_H from equation 5.5

Sample	α_H	β_H
x = 0	8.874(8)	0.0129(2)
x = 0.01	7.751(3)	0.0049(4)
x = 0.025	7.533(8)	0.0056(8)
x = 0.05	6.945(3)	0.0031(2)

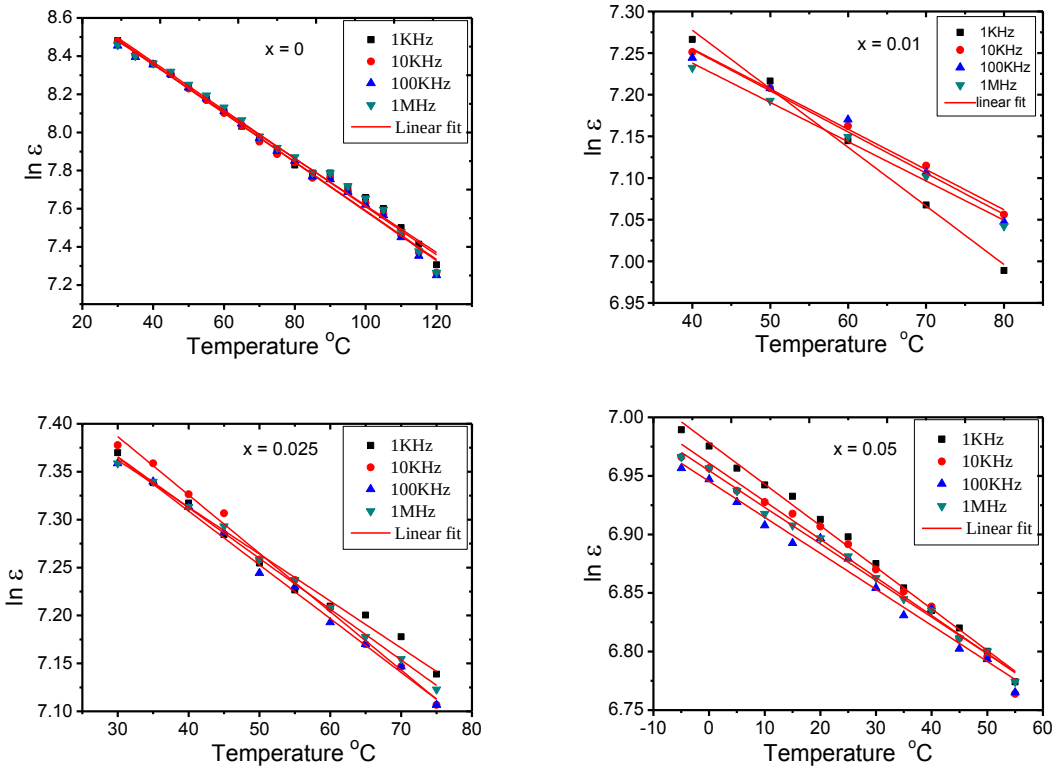

Figure 5.8 Plot of ln(ε) vs temperature at different frequencies for $Ba_{1-x}Dy_{2x/3}(Zr_{0.25}Ti_{0.75})O_3$

5.3.6.3 Dielectric behavior below T_m

It has been mentioned earlier that there is a broad distribution of freezing temperatures of the polar regions in the low temperature region. It is worthy to have a qualitative analysis of the behavior of polar clusters at temperature much below T_m. It has been reported that below T_m the relation between dielectric constant and frequency can be expressed as

$$\varepsilon_L(\omega) = \varepsilon_\infty + A(ln\omega_o - ln\omega) \quad (5.6)$$

where A is an intrinsic parameter that depends on temperature and is independent of frequency, ω_o is relaxation frequency, which is independent of temperature.

Thus, the low temperature dielectric response depends mainly on the temperature dependence of *A* and hence on the freezing process of the polar regions.

Equation (5.6) can be modified as

$$\varepsilon_L(\omega) = B(T) + A(T)\, ln\omega \tag{5.7}$$

where B(T) is given by

$$B(T) = \varepsilon_\infty + A(T)\, ln\omega_o \tag{5.8}$$

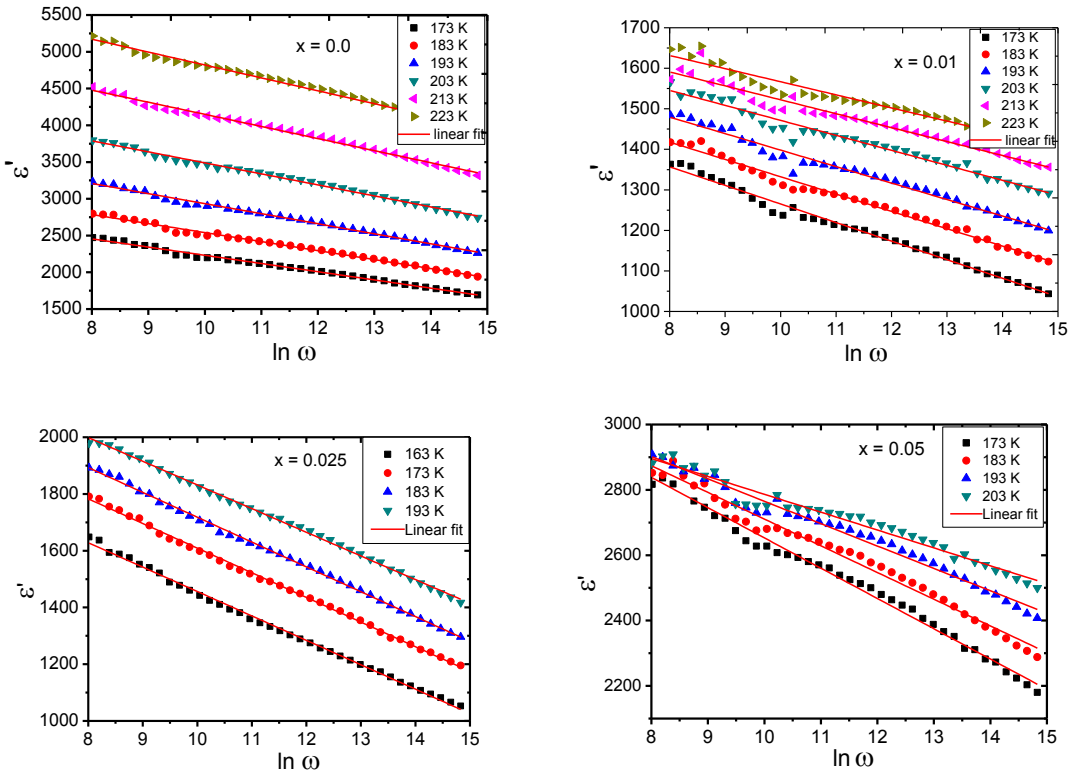

Figure 5.9 Frequency dependence of dielectric constant of $Ba_{1-x}Dy_{2x/3}(Zr_{0.25}Ti_{0.75})O_3$ ceramics

The values of *A* and *B* are obtained by fitting frequency dependence of ε at different temperatures using equation (5.7) (Figure. 5.9). Again by fitting *A* and *B* to equation.

5.8, we obtain the values ε_o and ω_o are given in Table 5.5 (Figure. 5.10). The ε_∞ values of all the samples studied are of the order of 10^3, which is very close to that for the typical perovskite type ferroelectrics. The temperature dependence of the parameter A, which reflects the degree of dispersion of the dielectric constant at temperatures much lower than T_m, can be fitted to the following empirical super exponential relation

$$A(T) = \exp\left[\alpha_L + \left(\frac{T}{\beta_L}\right)^{1+\delta}\right] \tag{5.9}$$

where α_L, β_L and δ (0 ≤δ≤ 1) are positive constants. Figure 5.11 shows the fit of *A(T)* vs *T* and it is clear that equation. (5.9) can indeed express the temperature dependence of *A(T)* at low temperature. The fitting parameters are listed in Table 5.5.

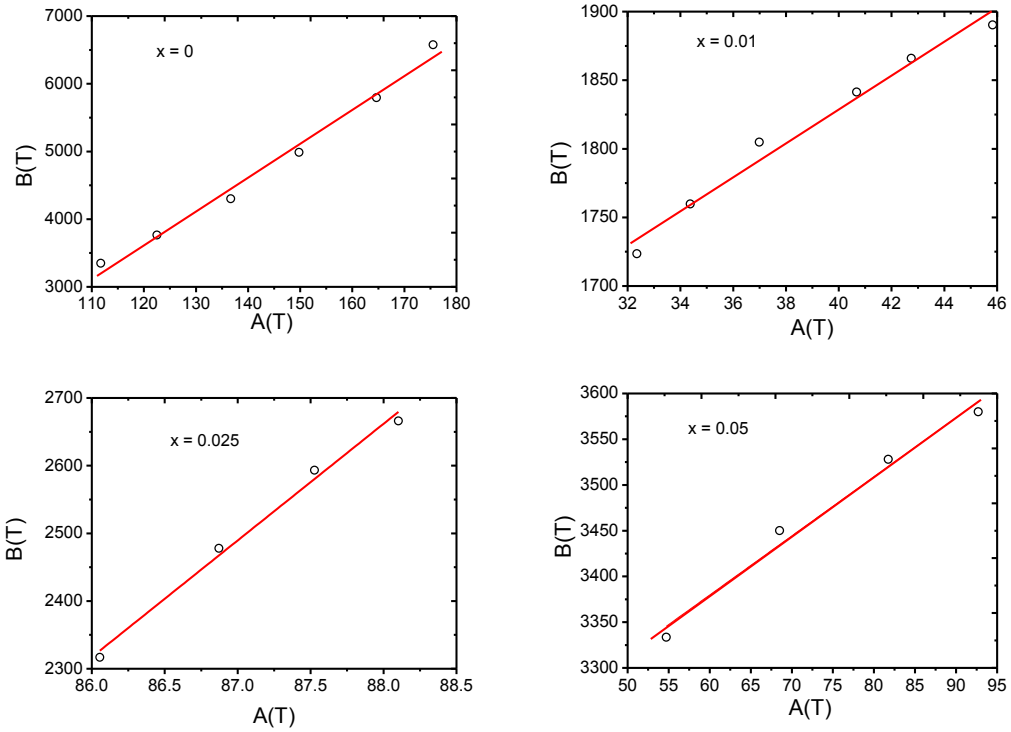

Figure 5.10 Linear relation between the A and B for $Ba_{1-x}Dy_{2x/3}(Zr_{0.25}Ti_{0.75})O_3$ ceramics

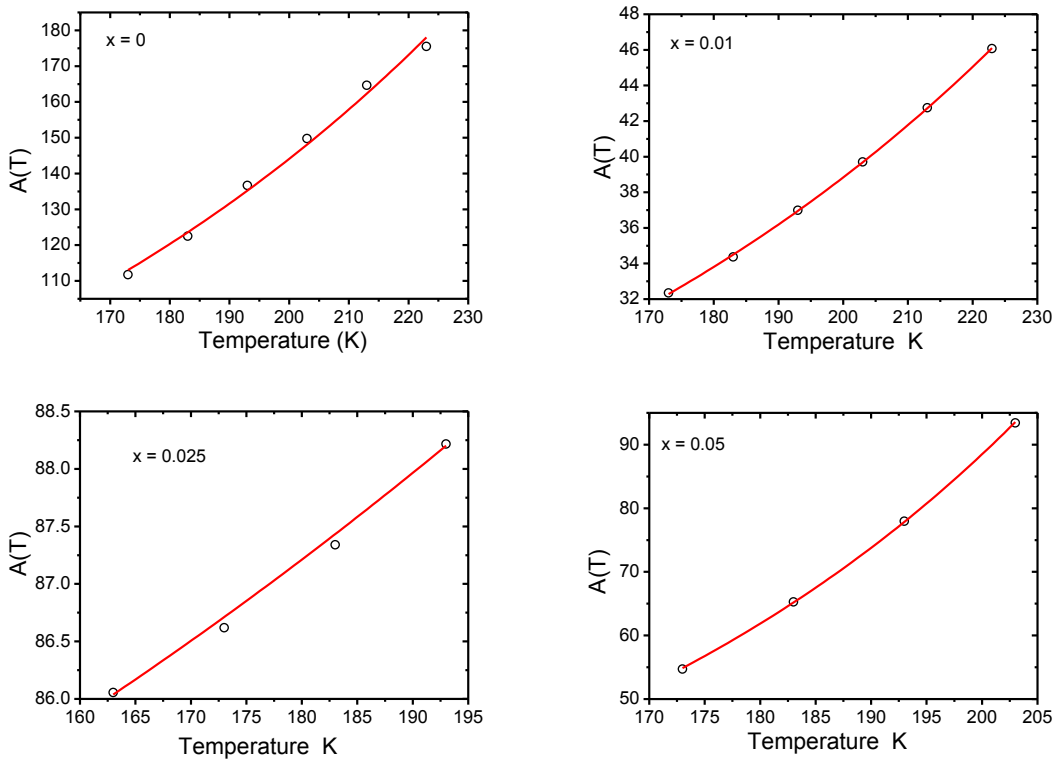

Figure 5.11 Fit of temperature dependence of A for $Ba_{1-x}Dy_{2x/3}(Zr_{0.25}Ti_{0.75})O_3$ ceramics

Table 5.5 The value of ω_o, ε_∞, α_L, β_L and δ from equation 5.8 and equation 5.9

Samples	ω_o	ε_∞	α_L	β_L	δ
x = 0	4.6×10^{21}	2372.8	1.88(7)	442.40(2)	0.891(6)
x = 0.01	2.25×10^{5}	1337.8	2.80(9)	219.50(7)	0.678(1)
x = 0.025	6.7×10^{74}	1250.6	4.39(4)	748.10(5)	0.640(3)
x = 0.05	640.2	2992.3	2.17(2)	118.73(1)	0.602(4)

5.3.7 Impedance Spectroscopy

Figure 5.12 (a) shows the complex impedance plot (Nyquist plot) of $Ba_{1-x}Dy_{2x/3}(Zr_{0.25}Ti_{0.75})O_3$ (x = 0.05) at different temperatures between 340 and 400^oC.

The symbol represents the experimental data and the line represents the theoretical fitting shown in Chapter 3 (equation 3.3). Characteristically, two semicircular arcs have been observed, although there is a lack of data to complete the semicircle in the lower frequency region especially at lower temperatures. At higher temperatures, there is a clear indication of second semicircle. It is observed that with the increase in temperature the radius of the semicircles decreases. It can be also seen from this figure that the complex impedance data are represented by depressed semicircle (i.e., centres of semicircle lie below the real axis) and at lower frequencies the values increases. The values of bulk resistivity, *(R_b),* and grain- boundary resistivity, *(R_{gb}),* can be estimated from the related intercepts on the real axis *(Z')* axis and the associated capacitance, obtained from equivalent circuit analysis by *ZView*. The capacitance values estimated at the maximum frequency using the relation $\omega_{max}RC = 1$ is shown in the Table 5.6. The experimental data of capacitance indicates that the high-frequency semicircle can be attributed to the electrical processes through the bulk (i.e. grain interior) of the material *(Irvine et al 1990)*. The low frequency second dispersion curve has been assigned to the grain boundary (blocking core) conduction. The value of bulk resistance *(R_b)* and grain boundary resistance *(R_{gb})* has been obtained from the intercept of the semicircular arc on real axis (*Z'*). Further, it appears from Figure 5.12 (a) and Table 5.6 that both grain and grain boundary resistance decreases with rise in temperature. It indicates that the grain boundary effect have assisted in lowering the barrier to the motion of charge carriers paving the way for increased electrical transport with rise in temperature.

The value of grain boundary resistance (R_{gb}) at different temperatures was estimated from the complex impedance spectrum (Figure5.12 (a)). This plot

indicates the changes in grain boundary resistance at elevated temperatures representing the role of grain boundaries in electrical conduction process of the material. The decrease in grain boundary resistance with rise in temperature may be due to the lowering of barrier favoring the increase of mobility of charge carriers that adds to the conduction process. The conduction mechanism for grains and grain boundaries are different. A hopping mechanism through various defect sites contributes the intergrain conduction whereas the interface barrier potential plays the major role for intragrain boundary condition *(Victor et al 2003)*. In both cases, resistance of grain and grain boundary decreases with increase in temperature showing the negative temperature coefficient of resistance (NTCR) behavior like that of a semiconductor.

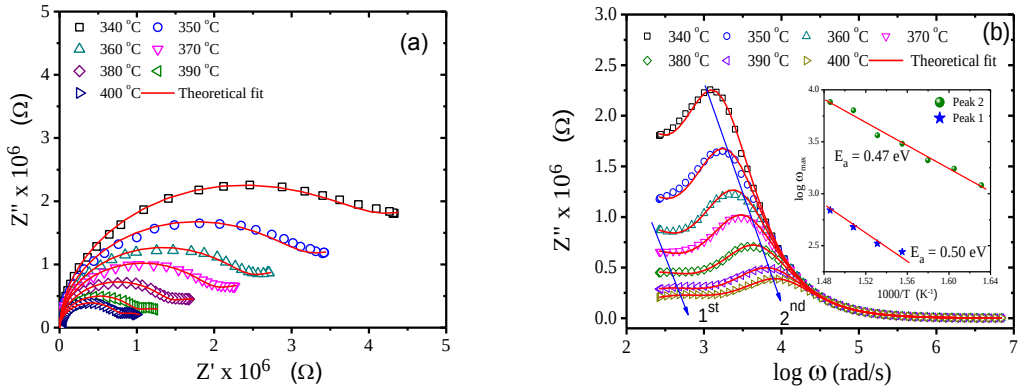

Figure 5.12 **(a)** Cole–Cole plots between Z' and Z'' for $Ba_{1-x}Dy_{2x/3}(Zr_{0.25}Ti_{0.75})O_3$ (x = 0.05) ceramic measured at various temperatures, **(b)** Variation of imaginary part Z'' of $Ba_{1-x}Dy_{2x/3}(Zr_{0.25}Ti_{0.75})O_3$ ceramic with frequency at different temperatures and **(inset)** Arrhenius plot of log ω_{max} from imaginary part of impedance

Figure 5.12 (b) shows the variation of the imaginary part of impedance (Z'') with frequency at different temperature. The curves show that the Z'' values reach a maxima peak (Z''_{max}) and the value of Z''_{max} shifts to higher frequencies with

increasing temperature. A typical peak broadening which is slightly asymmetrical in nature can be observed with the rise in temperature. The broadening of peaks in frequency explicit plots of *Z"* suggests that there is a spread of relaxation times, *i.e.*, the existence of a temperature dependent electrical relaxation phenomenon in the material *(Wieczorek et al 1998)*. The merger of *Z"* values in the high frequency region may possibly be an indication of the accumulation of space charge in the material. The relaxation process may be due to the presence of immobile species at low temperature and defects at higher temperature. In such a situation, one can determine the most probable relaxation time τ_m *(= 1/*ω_m*)* from the position of the peak in the *Z"* versus log ω plots. The most probable relaxation time follows the Arrhenius law (Figure 5.12 (b) (inset)). The activation energy E_a calculated from the least-squares fit to the points are 0.50*eV* and 0.47 *eV* for peak1 and peak2 respectively.

Table 5.6 Parameters obtained from temperature dependent impedance spectroscopy data for the $Ba_{1-x}Dy_{2x/3}(Zr_{0.25}Ti_{0.75})O_3$ (x = 0.05) ceramic

T ^oC	CPE_g nF	R_g $M\Omega$	CPE_{gb} nF	R_{gb} $M\Omega$	ω_{max} rad/s	σ_g S/cm	σ_{gb} S/cm
340	0.20	4.22	3.46	3.79	1180	0.23	0.26
350	0.19	3.22	4.77	2.32	1570	0.31	0.43
360	0.19	2.47	5.66	1.63	2070	0.40	0.61
370	0.19	1.99	6.94	1.21	2590	0.50	0.82
380	0.19	1.41	9.00	0.86	3750	0.70	1.15
390	0.18	0.96	11.6	0.60	5600	1.03	1.65
400	0.18	0.75	12.1	0.45	7300	1.32	2.19

5.3.8 Modulus Spectroscopy

Figure 5.13 displays the frequency (angular) dependence of *M'(ω)* and *M"(ω)* for $Ba_{1-x}Dy_{2x/3}(Zr_{0.25}Ti_{0.75})O_3$ (x = 0.05) as a function of temperature. *M'(ω)* (Figure 5.13 (a)) shows a dispersion tending toward M_∞ (the asymptotic value of M'(ω) at higher frequencies), while *M"(ω)* exhibits a maximum $M"_{max}$ centered at the dispersion region of *M'(ω).* It may be noted from Figure 5.13 (b) that the position of the peak $M"_{max}$ shifts to higher frequencies as the temperature is increased. The frequency region below peak maximum *M"* determines the range in which charge carriers are mobile on long distances. At frequency above peak maximum, the carriers are confined to potential wells, being mobile on short distances. The frequency ω_m (corresponding to $M"_{max}$) gives the most probable relaxation time τ_m from the condition $\omega_m\tau_m = 1$. Figure 5.13 (b) (inset) shows that the most probable relaxation time also obeys the Arrhenius relation and the corresponding activation energy E_a = 0.50 *eV* for relaxation is found to be close to the activation energy E_a for 2nd peak of $Z"_{max}$. The activation energy values for the electric modulus (= 0.50 *eV*) and for DC conductivity (= 0.48 *eV*) are almost identical suggesting a hopping mechanism for $Ba_{1-x}Dy_{2x/3}(Zr_{0.25}Ti_{0.75})O_3$ (x = 0.05). We have scaled each $M"/M"_{max}$ and each frequency by ω_{max} for different temperatures in Figure 5.14. The overlap of the curves for all the temperatures indicates that the dynamical processes are nearly temperature independent.

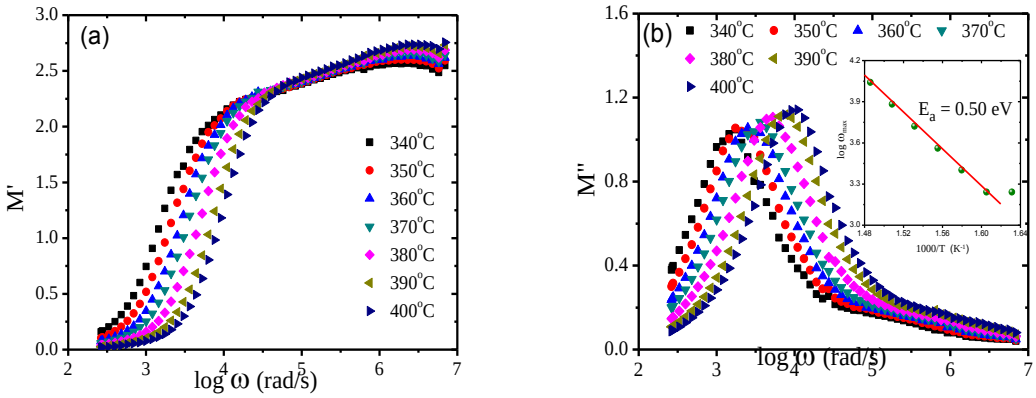

Figure 5.13 Variation of real part *M'* **(a)**, imaginary part *M"* **(b)** of $Ba_{1-x}Dy_{2x/3}(Zr_{0.25}Ti_{0.75})O_3$ (x = 0.05) ceramic with frequency at different temperatures and **(inset)** Arrhenius plot of *log* ω_{max} from imaginary part of Modulus

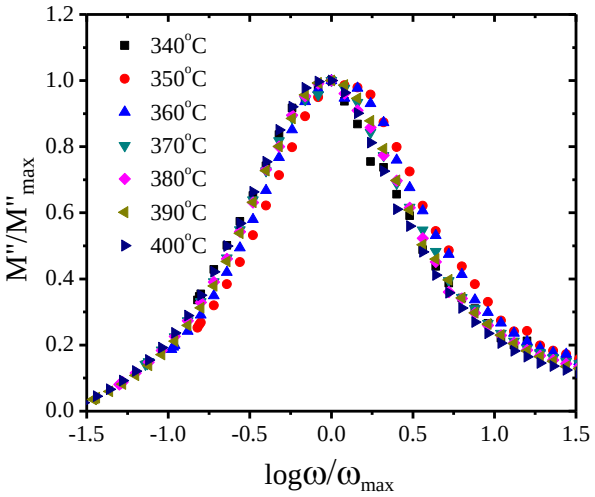

Figure 5.14 Scaling behaviour of *M"* at various temperatures for $Ba_{1-x}Dy_{2x/3}(Zr_{0.25}Ti_{0.75})O_3$ (x = 0.05) ceramic

5.3.9 AC and DC conductivity

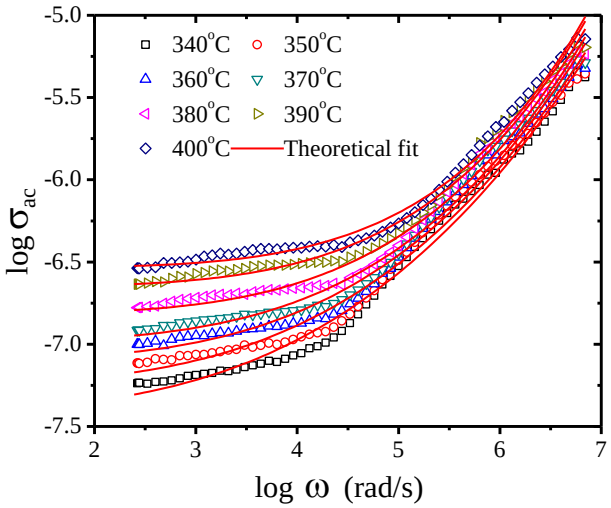

Figure 5.15 Frequency dependence of the AC conductivity of $Ba_{1-x}Dy_{2x/3}(Zr_{0.25}Ti_{0.75})O_3$ (x = 0.05) ceramic at various temperatures

The log–log plot of electrical conductivity versus frequency at different temperature is shown in Figure 5.15. To account for the high frequency dispersion, the conductivity spectra can be modeled by the form predicted by *Jonscher's (1977)* universal law

$$\sigma(w) = \sigma(0) + A\omega^n \qquad (5.10)$$

According to *Jonscher (1977)*, the origin of the frequency dependence of conductivity lies in the relaxation phenomena arising due to mobile charge carriers. When a mobile charge carriers hope to a new site from its original position, it remains in a state of displacement between two potential energy minima, which includes contributions from other mobile defects. After a sufficiently long time, the defect could relax until the two minima in lattice potential energy coincide with the lattice site. Also, the conduction behavior of the materials obeys the power law $\sigma\ (\omega)\ \alpha\ \omega^n$ with a slope change governed by n in the low temperature region. The ac

conductivity data are fitted to the *Jonscher's* equation and the fitting parameters A and n at various temperatures are given in Table 5.7. The solid lines are the fitted curves to the experimental ac conductivity data at different temperatures and the goodness of the fitting is satisfactory. The frequency exponent n is found to increase slightly with decreasing temperature.

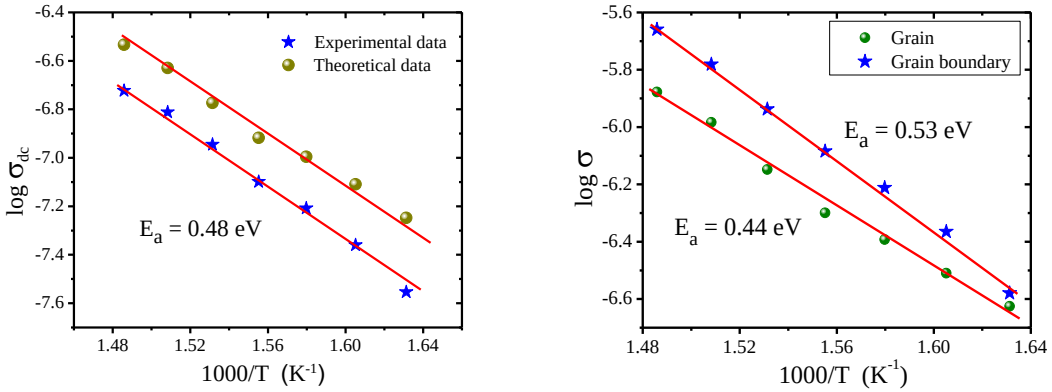

Figure5.16 **(a)** Temperature dependence of the DC conductivity and **(b)** Temperature dependence of the grain and grain boundary conductivity for $Ba_{1-x}Dy_{2x/3}(Zr_{0.25}Ti_{0.75})O_3$ (x = 0.05) ceramic

Table 5.7 Fitting parameters of AC conductivity by Jonscher's universal law of $Ba_{1-x}Dy_{2x/3}(Zr_{0.25}Ti_{0.75})O_3$ (x = 0.05) ceramic

Temperature (^0C)	*A*	*n*
340	1.26E-08	0.26538
350	2.09E-07	0.07383
360	1.24E-06	0.02197
370	3.85E-06	0.00918
380	8.79E-06	0.00567
390	8.55E-06	0.0088
400	7.10E-06	0.01344

The DC conductivity (σ_b) of the material has been evaluated from the complex impedance plots of the sample at different temperatures and is also recorded in Table 5.6 The DC conductivity estimated from the bulk response of the material has been observed as a function of temperature as shown in the Figure 5.16 (a). At higher temperatures, the conductivity versus temperature response is linear and can be explained by a thermally activated transport of Arrhenius type. The activation energy was found to be $0.48eV$. We have attempted to separately evaluate the grain and grain boundary conductivity as a function of temperature from impedance spectrum. The variation of electrical conductivity due to grain and grain boundary is shown in Figure 5.16 (b) showing linear behaviour and the activation energy is found to be $0.44eV$ and $0.53eV$ respectively.

CHAPTER 6

STRUCTURAL, ELECTRICAL AND OPTICAL STUDY OF HETEROVALENT YTTRIUM ION (Y^{3+}) SUBSTITUTED $Ba_{1-x}Y_{2x/3}Ti_{0.75}Zr_{0.25}O_3$ CERAMIC

6.1 Outline of the present work

The influence of substitution of heterovalent Y^{+3} ion at A site on the structural, micro-structural, electrical and optical behavior of the $BaZr_{0.25}Ti_{0.75}O_3$ has been studied in this chapter.

6.2 Sample Preparation

In the process of investigation on the doping effect of Y^{+3} in the $BaZr_{0.25}Ti_{0.75}O_3$ ceramic, the composition studied were represented by the general formula $Ba_{1-x}Y_{2x/3}Zr_{0.25}Ti_{0.75}O_3$ (BYZT) with x=0.0, 0.01, 0.025, 0.05. The raw powders $BaCO_3$, ZrO_2, TiO_2, Y_2O_3 were mixed in stoichiometric ratio with isopropyl alcohol as a medium by means of agate motar. The mixed powders were ball milled for 12 hours using acetone as a medium. The calcination and sintering temperatures are optimized to be 1350^oC for 6 hrs and 1450^oC for 4 hrs respectively.

6.3 Characterization

The samples were characterized by X-Ray Diffraction, Scanning Electron Microscopy, Energy Dispersive X-Ray Spectroscopy, X-ray absorption near-edge spectroscopy analyses, Ultraviolet visible spectroscopy, Photoluminescence, dielectric study and impedance study. The results are discussed in detail.

6.3.1 Structural Study

Figure 6.1 (a) shows the x-ray diffraction pattern of $Ba_{1-x}Y_{2x/3}Zr_{0.25}Ti_{0.75}O_3$, (x= 0.0, 0.01, 0.025, 0.05) ceramics confirms the single phase formation. The X-Ray diffraction patterns showed that all ceramics have perovskite type cubic structure with space group Pm3m, in agreement with the respective Joint Committee on Powder Diffraction Standards (JCPDS) card no. 36-0019. In addition, diffraction peaks corresponding to the secondary phases (Y_2O_3) were not detected, indicating that the Y^{3+} ions were incorporated into the $BaZr_{0.25}Ti_{0.75}O_3$ matrix. It has been reported in the literature that the x-ray diffraction patterns can be employed as structural characterization tool in order to evaluate the crystallinity or degree of order–disorder at long-range of the materials *(Cavalcante et al 2008).* Considering this supposition, the intense and well-defined diffraction peaks observed in Figure 6.1(a) suggest that these ceramics are structurally ordered at long-range. Figure 6.1(b) shows the lattice parameter as well as the unit cell volume results of $Ba_{1-x}Y_{2x/3}Zr_{0.25}Ti_{0.75}O_3$ ceramics. These data were estimated through the UNITCELL-97 program using the regression diagnostics combined with nonlinear least squares.

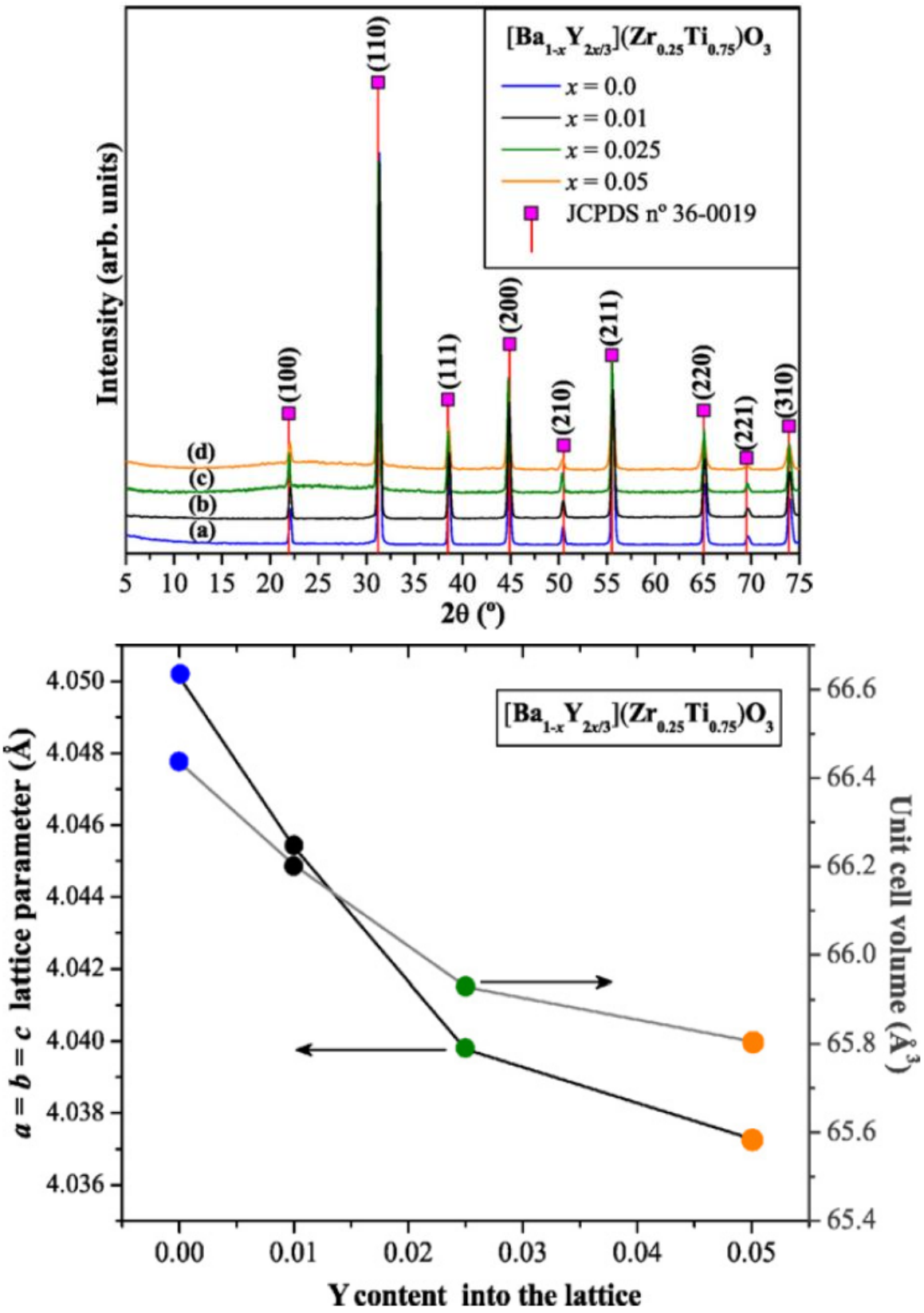

Figure 6.1 **(a)** X-Ray Diffraction patterns of $Ba_{1-x}Y_{2x/3}Zr_{0.25}Ti_{0.75}O_3$ ceramics and **(b)** The lattice parameter values and unit cell volume of $Ba_{1-x}Y_{2x/3}Zr_{0.25}Ti_{0.75}O_3$ ceramics

As it can be seen in this figure, the results indicated that the addition of Y^{3+} ions into the $BaZr_{0.25}Ti_{0.75}O_3$ phase slightly reduced the lattice dimensions. Recently, *Shan et al. (2007)* explained that the substitution of Ba atoms by those of Y^{3+} is able to induce distortions into the $BaZr_{0.25}Ti_{0.75}O_3$ phase because of the differences between the atomic radii. According to *Shan et al (2007), Watnable et al (1998)*, the ionic radius of Ba^{2+} ions is 0.161 *nm*, while that of Y^{3+} is 0.086 nm. On the basis of these assumptions, it is possible to conclude that the substitution of B-sites commonly occupied by Ba^{2+} ions by those of Y^{3+} tends to promote an electronic compensation into the matrix. It can be described by the following Kröger–Vink equation:

$$Y_2O_3 \rightarrow 2Y_{Ba}^{\bullet} + V_{Ba}^{''} + 3O_0^x \qquad (6.1)$$

This equation implies that for every two Y^{3+} ions positioned on the A-site, one cationic vacancy $V_{Ba}^{''}$ is necessary to promote the charge neutrality. In this case, the concentration of vacancies is higher, when there is an increase of Y^{3+} content into the lattice.

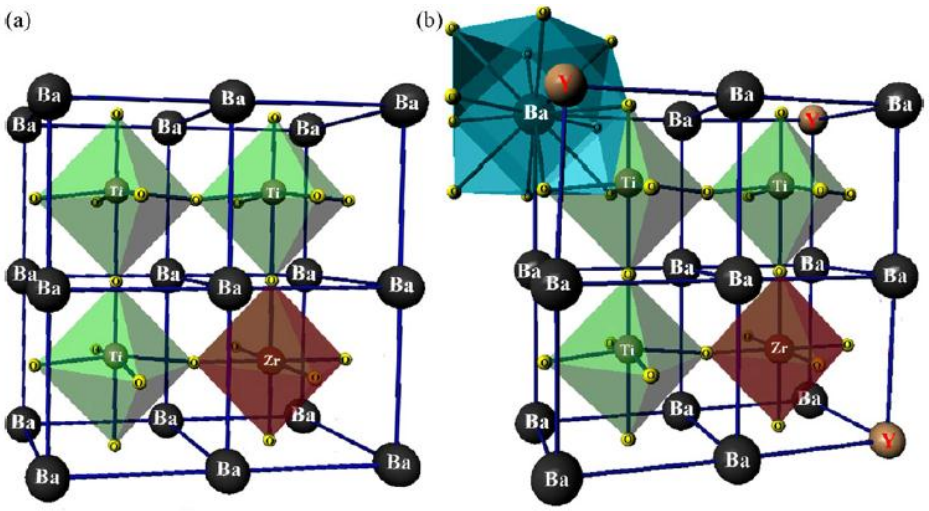

Figure 6.2 Schematic representation of **(a)** pure and **(b)** Y-doped $BaZr_{0.25}Ti_{0.75}O_3$ supercells, illustrating the $[TiO_6]$, $[ZrO_6]$ and $[BaO_{12}]$ clusters

Figure 6.2 shows the schematic representation of crystalline (a) pure and (b) Y-doped $BaZr_{0.25}Ti_{0.75}O_3$ supercells (1 × 2 × 2). In both supercells, the Ti and Zr atoms (lattice formers) are bonded to six oxygens in an octahedral configuration, i.e., forming the [TiO_6] and [ZrO_6] clusters. In the non-polar [ZrO_6] clusters, the Zr atoms occupy a centrosymmetric position into the octahedral, while in the polar [TiO_6] clusters, the Ti atoms are slightly displaced along the [0 0 1] direction *(Maiti et al 2006)*. This displacement or distortion is supposed to be caused by the covalent character between the O–Ti–O bonds (directional orientations) into the perovskite-type structure *(Maiti et al 2006).* On the other hand, the Ba atoms (lattice modifiers) are bonded to twelve oxygens, resulting in a dodecahedron-type geometry known as [BaO_{12}] clusters (ionic bond with radial orientation) (Figure 6.2 (b)). Therefore, the structural order–disorder as well as the polarization mechanisms into the cubic $BaZr_{0.25}Ti_{0.75}O_3$ phase are caused by the existence of polar [TiO_6] clusters close to those of [BaO_{12}]. In the crystalline Y-doped $BaZr_{0.25}Ti_{0.75}O_3$ supercell, the Y^{3+} atoms are able to substitute the sites occupied by Ba atoms, resulting in the formation of [YO_6] clusters *(Duan et al 2005)*. In principle, future investigations will be performed by means of X-Ray Absorption Near-Edge Structure (XANES) and extended X-ray absorption fine structure spectroscopies to understand the influence of Y^{3+} ions on the number coordination and local non-centro-symmetry of $BaZr_{0.25}Ti_{0.75}O_3$ ceramics.

6.3.2 Microstructure

Figure 6.3 shows the Scanning electron micrographs of $Ba_{1-x}Y_{2x/3}Zr_{0.25}Ti_{0.75}O_3$ ceramics prepared with different concentrations. A closer examination of the Scanning electron micrographs revealed that the Y^{3+} content strongly modifies the microstructure of the material. Initially, when the $BaCO_3$ TiO_2, ZrO_2 and Y_2O_3 powders are mixed and milled, its particle sizes are reduced to favor the matter transport mechanism during the sintering process. However, mainly due to the milling stages, probably the particles have irregular spherical shapes. When the powders are submitted to the sintering process performed at 1450^oC for 4 h, the movement of atoms or molecules is driven by differences in curvature between the particles in contact *(Rahaman 2008)*. In order to reduce surface free energy, atoms supposedly move from particles with smaller radius to those with larger radius. Particularly, for the $Ba_{1-x}Y_{2x/3}Zr_{0.25}Ti_{0.75}O_3$ ceramics with concentrations of x = 0 (pure phase) and x = 0.01, it is possible that the matter transport between several aggregated particles and the high anisotropy in the grain boundary energies induced the formation of compact and irregular polyhedral particles (Figure 6.3 (a) and (b)). The addition of Y (x = 0.025 and 0.05) into the matrix intensified the shrinkage and densification rates, resulting in a mass more dense (Figure 6.3 (c) and (d)). This phenomenon suggests that the formation of $[YO_6]$ clusters is able to influence in the microstructural stability. Possibly, it promoted a rapid inter-diffusion movement via grain-boundary, favoring the formation of necks between the grains as well as its growth.

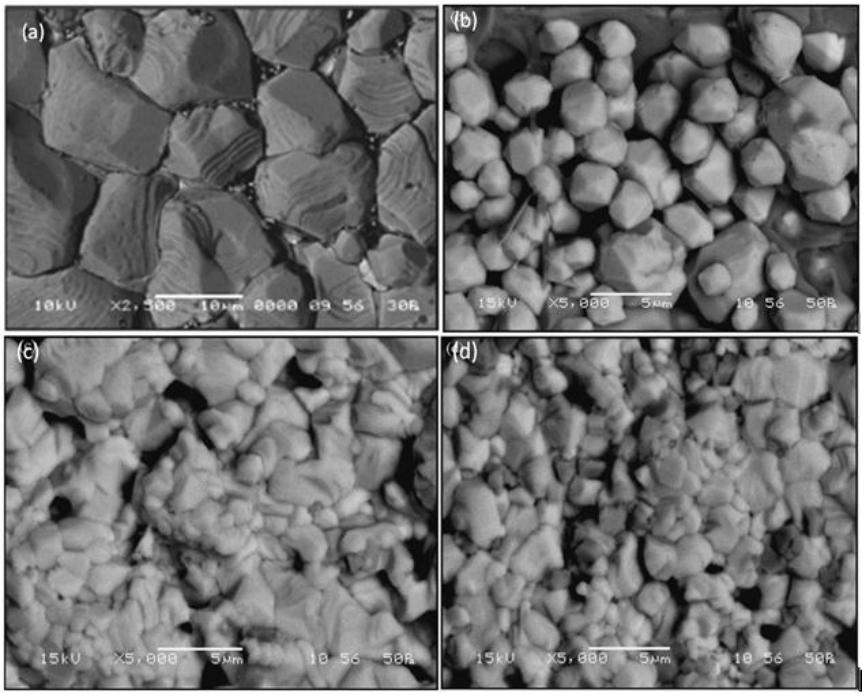

Figure 6.3 Scanning electron micrographs of $Ba_{1-x}Y_{2x/3}Zr_{0.25}Ti_{0.75}O_3$ ceramics **(a)** x = 0, **(b)** 0.01, **(c)** 0.025 and **(d)** 0.05

6.3.3 Fourier transforms infrared spectroscopy analyses

From the Fourier transforms infrared spectra (Figure 6.4) one get information about the role of $[YO_6]$ clusters in $BaZr_{0.25}Ti_{0.75}O_3$ crystal lattice *(Majli 2003).* The pure $BaZr_{0.25}Ti_{0.75}O_3$ crystal phase is characterized by the absorption band at 536 cm^{-1} due to anti-symmetric stretching vibrations of metal oxygen bonds $[TiO_6]$ and $[ZrO_6]$ clusters. The substitution of $[BaO_{12}]$ by $[YO_6]$ clusters creates not only V_{Ba}^{x}, $V_{Ba}^{\prime}$ or $V_{Ba}^{"}$ vacancies but also internal stresses on the octahedral sites $[TiO_6]$ and/or $[ZrO_6]$ clusters *(Wang et al 2002, Karan et al 2008)*. The substitution process can then modify the interaction forces between the O-Ti-O and O-Zr-O bonds, what can lead to considerable displacement of the absorption band to high wave number region (568 cm^{-1} and 570 cm^{-1}).

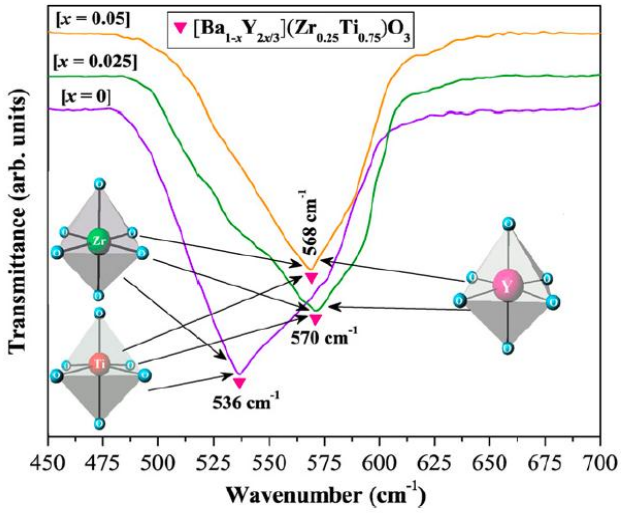

Figure 6.4 Fourier transforms infrared spectra of $Ba_{1-x}Y_{2x/3}Zr_{0.25}Ti_{0.75}O_3$ (x = 0, 0.025 and 0.05)

6.3.4 Fourier transforms Raman scattering spectroscopy analyses

Figure 6.5 shows the Fourier transforms Raman scattering spectra of $Ba_{1-x}Y_{2x/3}Zr_{0.25}Ti_{0.75}O_3$ powders (x = 0, 0.025 and 0.05). Although the powders $Ba_{1-x}Y_{2x/3}Zr_{0.25}Ti_{0.75}O_3$ (x = 0, 0.025 and 0.05) crystallize in a cubic phase, the Fourier transforms Raman scattering spectra indicated the presence of seven Raman-active modes. This fact can be due to the structural order-disorder induced by the successive milling cycles and/or because of the distortions caused by the substitution of [BaO_{12}] clusters by those of [YO_6]. According to the literature *(Crocombette et al 1994, Domenico et al 1968),* these Raman-active modes can be divided into longitudinal (LO) and transverse (TO) components, as a consequence of the long-range electrostatic forces responsible for the lattice ionicity. A closer analysis of the Fourier transforms Raman scattering spectrum for the pure $BaZr_{0.25}Ti_{0.75}O_3$ phase indicated the presence of $A_1(TO_1)$ and $A_1(TO_3)$ modes at around 180 cm^{-1} and 514 cm^{-1}, respectively. The $A_1(TO_1)$ mode is ascribed to the O-

Ti-O symmetric stretching vibrations, while the $A_1(TO_3)$ mode is due to the asymmetric vibrations *(Chaves et al 1974, Kreisel et al 2004)* .In addition, the $E(TO_1)$ and $E(TO_2)$ modes detected at around 114 cm^{-1} and 305 cm^{-1} correspond to the phase transition from tetragonal to cubic crystal structure *(Dobala et al 2005).* Actually, for the $BaZr_{0.25}Ti_{0.75}O_3$ phase, these modes indicate a high concentration of polar $[TiO_6]$ distorted clusters into a predominantly cubic matrix. The $E(TO_2)$ stretching mode is particularly observed in Fourier transforms Raman scattering spectra because of the existence of polar $[TiO_6]$ clusters into the perovskite-type structure. Moreover, the intensity exhibited by this mode in the $BaZr_{0.25}Ti_{0.75}O_3$ phase is lower when compared to the $BaTiO_3$ *(Begg et al 1996)*. A plausible explanation for this phenomenon has been reasoned in the assumption that the distribution of non-polar $[ZrO_6]$ clusters into the lattice reduces the dipolar interactions between the polar $[TiO_6]$ clusters *(Dixit et al 2004).*

Also, these kinds of clusters are responsible for the $A_1(LO_3)$ mode observed at 718 cm^{-1} . The other Raman-active modes detectable in the Fourier transforms Raman scattering spectra are arising from lattice vibrations along the LO and TO directions. Also, when the Y atoms were incorporated into the Ba $(Zr_{0.25}Ti_{0.75})O_3$ structure, some Raman-active modes presented a subtle displacement [$A_1(TO_1)$, $E(TO_2)$, $A1(LO_3)$ and $E(LO)$] or disappearance $A_1(TO_1)$ in the Fourier transforms Raman scattering spectra (Figure 6.5). This observation can be correlated with the increase in the degree of symmetry of the cubic structure (O_h) and/or because of the contraction in the unit cell volume by the $[YO_6]$ clusters. In particular, the overlap between the $A_1(TO_2)$ and $E(TO_2)$ modes can be due to a reduction in the electronic density around the $[YO_6]$ clusters.

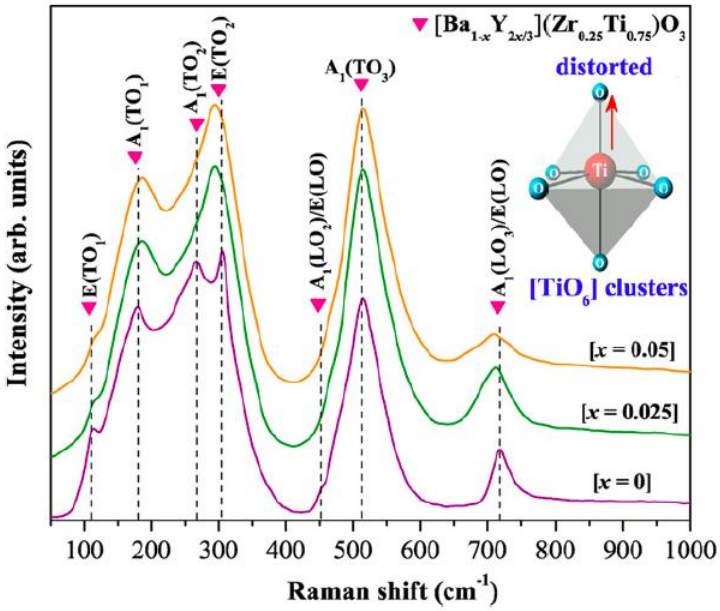

Figure 6.5 Fourier transforms Raman scattering spectra of $Ba_{1-x}Y_{2x/3}Zr_{0.25}Ti_{0.75}O_3$ powders (x = 0, 0.025 and 0.05). The vertical dashed lines indicate the positions and relative intensities of Raman-active modes

6.3.5 X-ray absorption near-edge spectroscopy analyses

Figure 6.6 (a) shows the general Ti K-edge XANES spectra both $BaTiO_3$ and $Ba_{1-x}Y_{2x/3}Zr_{0.25}Ti_{0.75}O_3$ powders (x = 0, 0.025 and 0.05). The XANES technique became a powerful tool in the description of electronic structures of amorphous and crystalline compounds (*Menard et al 2009*). Moreover, the XANES spectra are very efficient to obtain information on the structural order at short-range of the materials, such as: coordination environment (tetrahedral, octahedral, dodecahedral), oxidation state and subtle lattice distortions *(Lazaro et al 2007)*. In Figure 6.6 (a), it was detected a small peak located at around 4970 *eV* (●) known as pre-edge region, which corresponds to the 1s → 3d electronic transitions (*Lazaro et al 2007, Raval et al 1999)*.

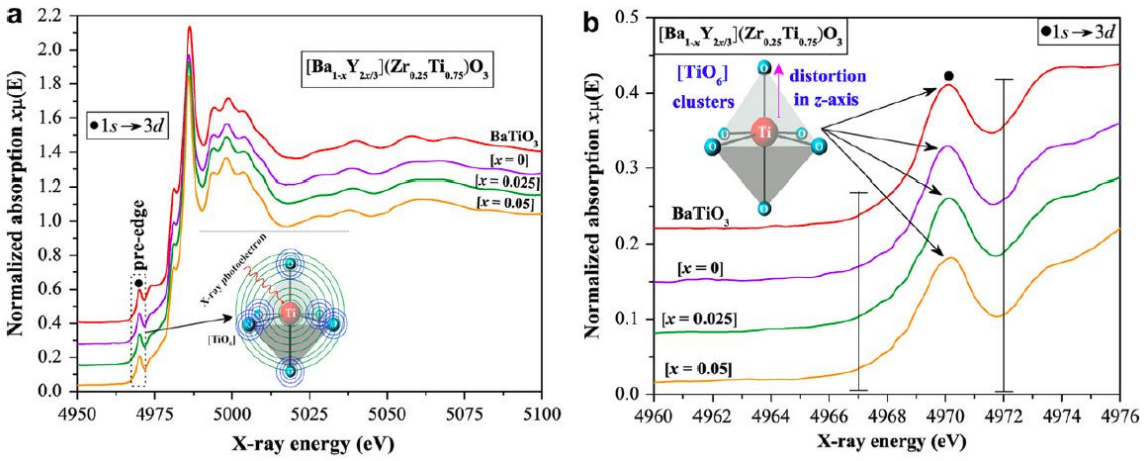

Figure 6.6 **(a)** XANES spectra of $BaTiO_3$ and $Ba_{1-x}Y_{2x/3}Zr_{0.25}Ti_{0.75}O_3$ powders (x = 0, 0.025 and 0.05). The inset illustrates the X-ray photoelectron scattering, where the photoelectron excited at the atomic absorption site (Ti atoms) is scattered by the neighbor O atoms and **(b)** Pre-edge peak located in the range from 4960 to 4976 *eV*. The vertical lines indicate the positions where it was performed the baseline in order to calculate the pre-edge peak area.

Normally, there is a probability of this forbidden electronic transition to be allowed because of a mixture between the occupied O 2p orbitals and empty Ti 3d orbitals *(Vedrinskii et al 1998)*. The intensity variations of the pre-edge peaks (●) are caused by the degree of hybridization associated to the O 2p and Ti 3d states of the $[TiO_6]$ clusters (Inset Figure 6.6(a)). The literature *(Frenkel et al 2005)* explains that the local Ti displacement (non-centrosymmetric) into the $[TiO_6]$ clusters leads to progressive increase in the pre-edge peak intensities. In fact, *Farges et al (1997)* reported that the energy and intensity associated to this peak for the titanate-based perovskite oxides can be classified into three distinct groups, depending on the coordination number of Ti-O bonds (four, five and six). As it can be seen in Figure 6.6 (b), practically there are not modifications on the relative positions of the pre-edge peaks, suggesting only the existence of hexa coordinated Ti atoms (TiO_6

clusters). In order to qualitatively estimate the displacement presented by the Ti atoms into the [TiO_6] clusters, it was employed the method proposed by *Frenkel et al (2007)*. According to these authors, the pre-edge peak area (A) in perovskite-type titanates is proportional to the square of the off center Ti displacement (d_{Ti}), which is described by the following equation:

$$A = \frac{\gamma_i}{3} d_{Ti}^2 \qquad (6.2)$$

where γ_i is a constant ($BaTiO_3$= 11.2 *eV/A*)

Based on this equation, the area of each pre-edge peak (●) was estimated (from 4967 *eV* to 4972.2 *eV*) by means of integration. In the calculus, the XANES spectrum of $BaTiO_3$ phase was adopted as reference for those of $Ba_{1-x}Y_{2x/3}Zr_{0.25}Ti_{0.75}O_3$ (x = 0, 0.025 and 0.05), since the distortion of Ti atoms along the [001] direction is well-known for this material in the literature *(Orhan et al 2005, Gurgel et al 2007)*. On the other hand, mechanical calculations based on the Density Functional Theory (DFT) *(Zhang etal2006)* showed that all four phases (cubic, tetragonal, orthorhombic and rhombohedral) of $BaTiO_3$ ferroelectrics have local Ti distortions toward [111] (octahedral face). In our case, taking into consideration just the lattice modifiers, the $BaTiO_3$ phase was assumed to present 100% [TiO_6] clusters. However, the $Ba_{1-x}Y_{2x/3}Zr_{0.25}Ti_{0.75}O_3$ (x=0, 0.025 and 0.05) is not composed only of [TiO_6] clusters, but also by those of [ZrO_6]. Hence, the calculated pre-edge peak area for all compositions in this structure was subtracted from 25% (equivalent to the quantity of [ZrO_6] clusters). These area data were used in equation (6.2) in order to estimate the off-center Ti displacements (d_{Ti}).

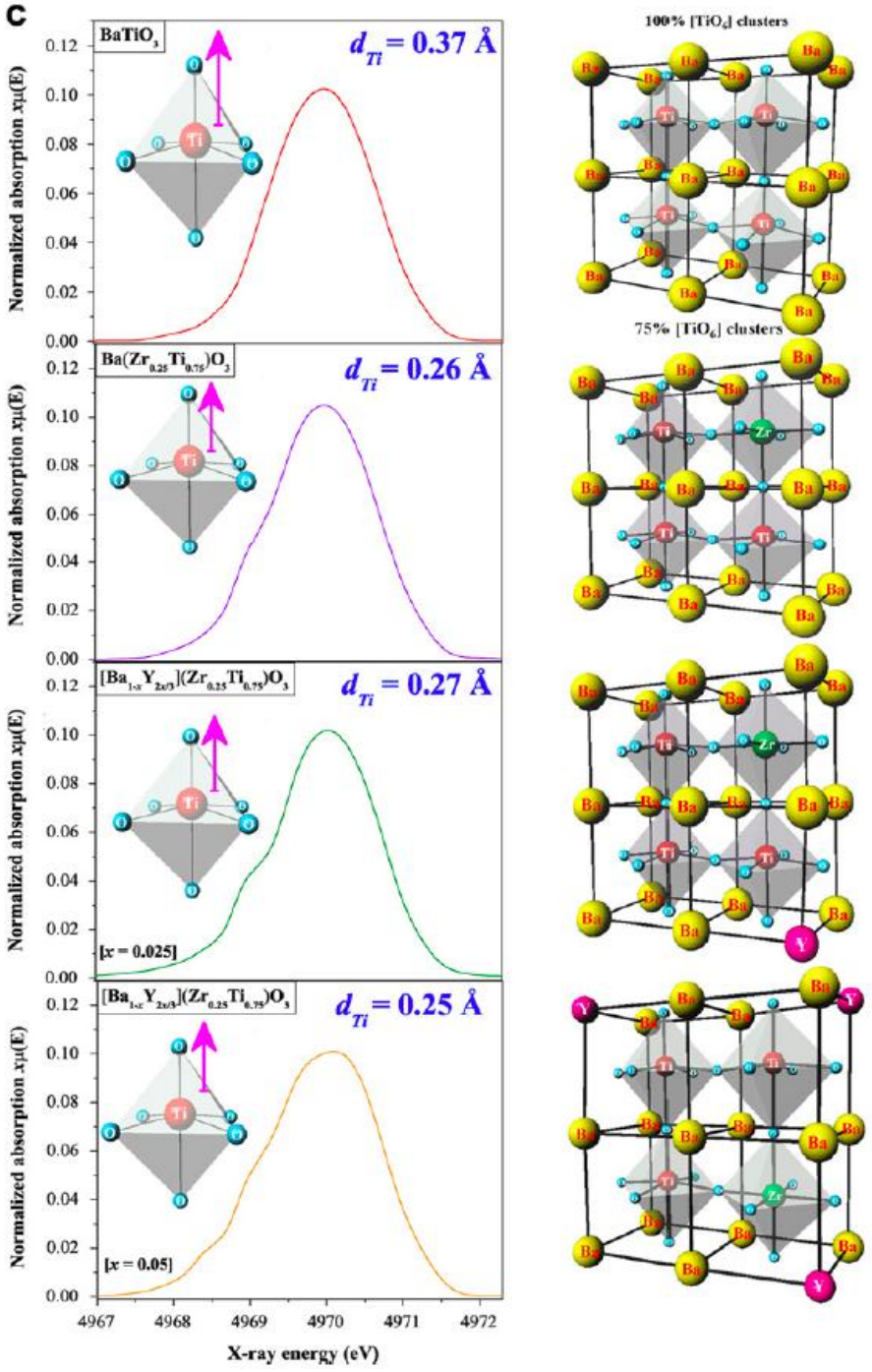

Figure 6.6 **(c)** The calculated pre-edge area. The insets illustrate the off-center Ti displacement for the octahedral sites and **(d)** Percentages of distorted [TiO_6] clusters.

The d_{Ti} results and its respective supercells with the off-center Ti sites along the [001] direction are shown in Figure 6.6 (c) and (d), respectively. Thus, it was obtained the following d_{Ti} values: d_{Ti} ($BaTiO_3$) = 0.37$\AA$ > d_{Ti} = 0.27$\AA$ > d_{Ti} = 0.26$\AA$ > d_{Ti}

= 0.25$\AA$. In principle, the low d_{Ti} value suggests that the addition of Zr atoms into the $BaTiO_3$ matrix reduces the structural disorder (Figure 6.6). Also, it was noted that the Y^{3+} concentration does not strongly influenced in the distortion of Ti^{4+} sites. In the literature, some studies have been reported on the structural modifications caused by the concentration of Y^{3+} ions into the perovskite-based materials. For example, *Potrepka et al (2002) and Shanthakumar et al (2006)* showed through XANES measurements that the addition of Y^{+3} ions into the $(Ba_{0.60}Sr_{0.40})TiO_3$ lattice does not affect the average Ti displacement from the octahedron center.

6.3.6 Ultraviolet visible absorption spectroscopy analyses

Figure 6.7 (a-c) shows the UV-vis absorption spectra of $Ba_{1-x}Y_{2x/3}Zr_{0.25}Ti_{0.75}O_3$ powders (x = 0, 0.025 and 0.05). The optical band gap energy (E_{gap}) was estimated by the method proposed by *Wood and Tauc (1972)*. According to these authors the optical band gap is associated with the absorbance and photon energy by the following equation:

$$h\nu\alpha \propto \left(h\nu - E_{gap}\right)^n \tag{6.3}$$

where α is the absorbance, h is the Planck constant, υ is the frequency, E_{gap} is the optical band gap and n is a constant associated to the different types of electronic transitions (n = 0.5, 2, 1.5 or 3 for direct allowed, indirect allowed, direct forbidden and indirect forbidden transitions, respectively). Thus, the E_{gap} values of $Ba_{1-x}Y_{2x/3}Zr_{0.25}Ti_{0.25}O_3$ powders were evaluated extrapolating the linear portion of the curve or tail. In our work, the UV-vis absorbance spectra indicated an indirect allowed transition and, therefore, the value of n = 2 is used in equation (6.3).

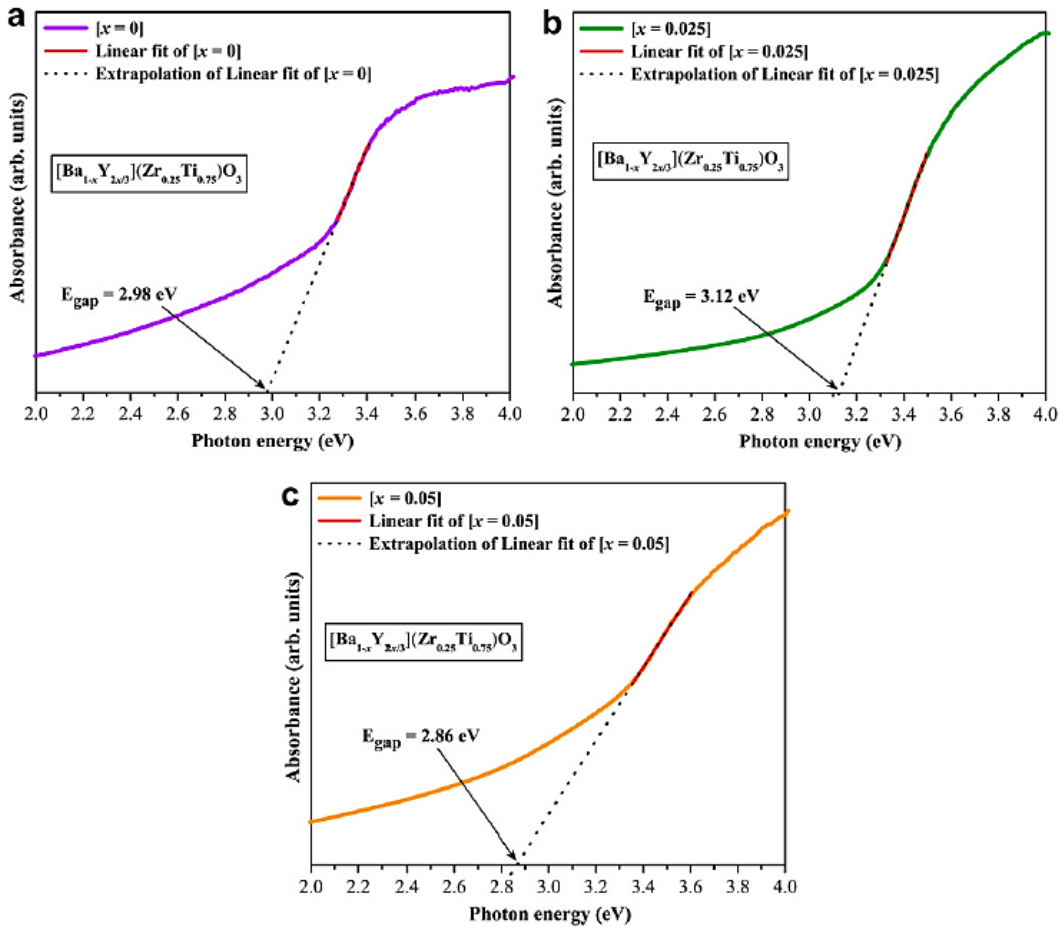

Figure 6.7 UV-vis absorption spectra of $Ba_{1-x}Y_{2x/3}Zr_{0.25}Ti_{0.75}O_3$ powders **(a)** x = 0, **(b)** 0.025 and **(c)** 0.05)

The literature (*Cavalcante et al 2007*) describes that the band gap energy is indirect when the electronic transitions occur from maximum-energy states located near or in the valence band (VB) to minimum-energy states below or in the conduction band (CB), but in different regions in the Brillouin zone. The distinct E_{gap} calculated from the UV-vis absorption spectra indicated the existence of intermediary energy levels within the optical band gap (Figure 6.7 (a-c)).We believe in these results, since the excitation energy (λ= 350 *nm* or 3.54 *eV*) is higher than the E_{gap} presented for all powders. The highest E_{gap} value was verified for the powders with *Y* content up to *x* = 0.025, suggesting a different conformation or low concentration of energy states

within the band gap. It is possible to conclude that these energy states are basically composed of O 2p orbitals (near the VB) as well as Ti 3d orbitals, Y and Zr 4d orbitals (below the CB) *(Anicete-Santos et al 2005)* . The origin of these orbitals or energy levels is directly related to the presence of structural order-disorder into the random lattice, as a consequence of symmetry break between the O-Zr-O, O-Ti-O and/or O-Y-O bonds (oxygen vacancies) and/or distortions on the [TiO_6] clusters.

6.3.7 Photoluminescence properties and wide band model based on the electronic transitions

Figure 6.8 (a) shows the PL spectra of $Ba_{1-x}Y_{2x/3}Zr_{0.25}Ti_{0.75}O_3$ powders synthesized with different *Y* concentrations (x = 0, 0.025 and 0.05). A model based on electronic transitions between different intermediary energy levels within the band gap is illustrated in Figure 6.8 (b). The broad PL spectra are optical phenomena caused by diverse electronic transitions occurring in different energy levels (deep or shallow holes) within the band gap *(Longo et al 2008).*The literature *(Cavalcante et al 2009)* reports that the deep holes are origin states for the green, yellow, orange and red PL emissions at room temperature, while the shallow holes are responsible for the violet and blue emissions. In our case, using an excitation source of 350 *nm* wavelength, the pure $BaZr_{0.25}Ti_{0.75}O_3$ phase exhibited a weak PL emission, where the maximum point was detected at around 467 *nm* (blue emission) (Figure 6.8 (a)). Therefore, it is an indicative that the charge transference process as well as the trapping of electrons occurs because of a greater contribution of the shallow holes than the deep holes. In addition, for the $Ba_{1-x}Y_{2x/3}Zr_{0.25}Ti_{0.75}O_3$ powders (x = 0.025 and 0.05), the PL spectra revealed a slightly displacement from 467 *nm* to 460 *nm* as

well as an increase in the intensity. This result suggests that when the Y atoms occupied the Ba sites into the perovskite, it contributed to the reorganization and formation of new energy levels (Y *4d* orbitals). Also, the existence of hexa-coordinated Y atoms ([YO_6] clusters) is able to promote the creation of Ba vacancies (V_{Ba}^{x}, V_{Ba}' or $V_{Ba}^{"}$) into the host matrix.

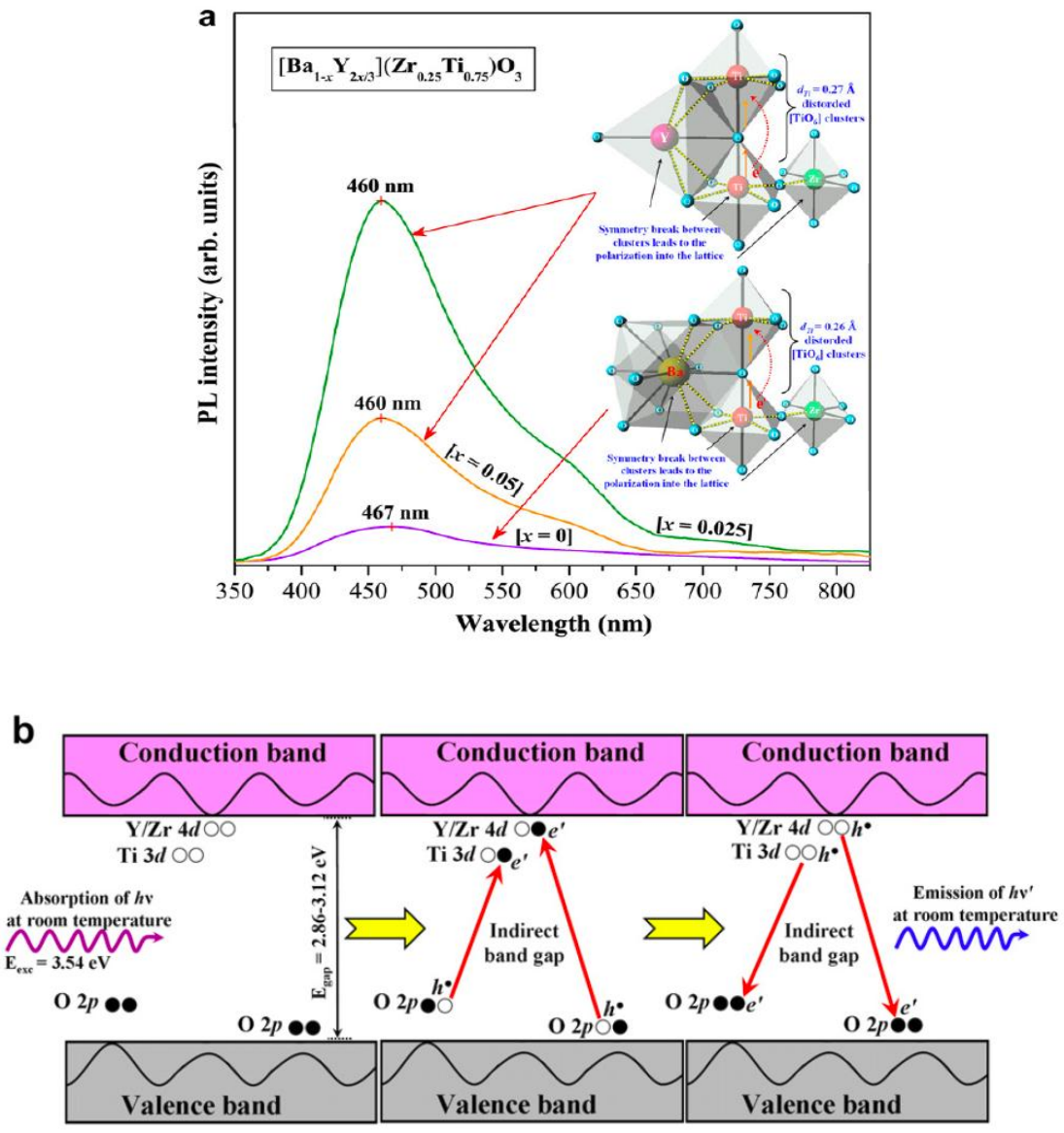

Figure 6.8 **(a)** PL spectra at room temperature of $Ba_{1-x}Y_{2x/3}Zr_{0.25}Ti_{0.75}O_3$ powders (x = 0, 0.025 and 0.05). The insets show two possible charge transference processes between the distorted [TiO_6] clusters. **(b)** Wide band model based on the electronic transitions between the O 2p, Ti 3d, Zr and Y 4d orbitals.

When compared both the Y-doped $BaZr_{0.25}Ti_{0.75}O_3$ powders, the PL spectra indicated a low intensity for those with Y content up to x = 0.05. In this case, this composition certainly formed a high concentration of structural defects, mainly Ba vacancies, actuating as extinction centers of PL emission. Insets in Figure 6.8 (a) illustrate two examples of charge transference processes via distorted $[TiO_6]$ clusters for the pure and Y-doped $BaZr_{0.25}Ti_{0.75}O_3$ phases. As it was previously described in the text, the $Ba_{1-x}Y_{2x/3}Zr_{0.25}Ti_{0.75}O_3$ phase is probably formed by O 2p orbitals (near the VB) as well as Ti 3d orbitals, Y and Zr 4d orbitals (below the CB). Thus, it was proposed a wide band model based on the electronic transitions between these intermediary energy levels in order to explain the origin of the PL emissions for this system (Figure 6.8 (b)). In the first stage, also known as excitation process, the electrons situated in the O 2p orbitals absorb the photon energies (hυ) arising from incident wavelength (λ= 350 *nm* or 3.54 *eV*). Afterward, the energetic electrons are promoted to Ti *3d* and/or Zr/Y 4d orbitals (higher energy states). Finally, when the electrons fall back again to lower energy states via radiative decays, the energies arising from these electronic transitions are converted in photons (*hυ'*). In this case, the several photons (*hυ'*) originated during the multiple radiative electronic transitions are responsible by the PL emissions (Figure 6.8(b)).

6.3.8 Dielectric Characterization

The temperature dependence of the relative permittivity for Y-doped $BaZr_{0.25}Ti_{0.75}O_3$ ceramics for various frequencies is shown in Figure 6.9. The value of ε' increases gradually to a maximum value (ε_m) with increasing in temperature and then decreases smoothly indicating a phase transition. The maximum of the dielectric

permittivity (ε_m) and the corresponding temperature maximum (T_m) depend upon the measurement frequency for all compositions. The magnitude of dielectric constant decreases with increasing frequency and the maximum shifts to higher temperature. This indicates that the dielectric polarization has a relaxation type nature. The Curie temperature is increased for at 1 atom% of Y and decreased for higher values of Y content. The Curie temperatures and T_m for different Y content is given in Table 6.1. The decrease in Curie temperature may be due to a decrease in grain size.

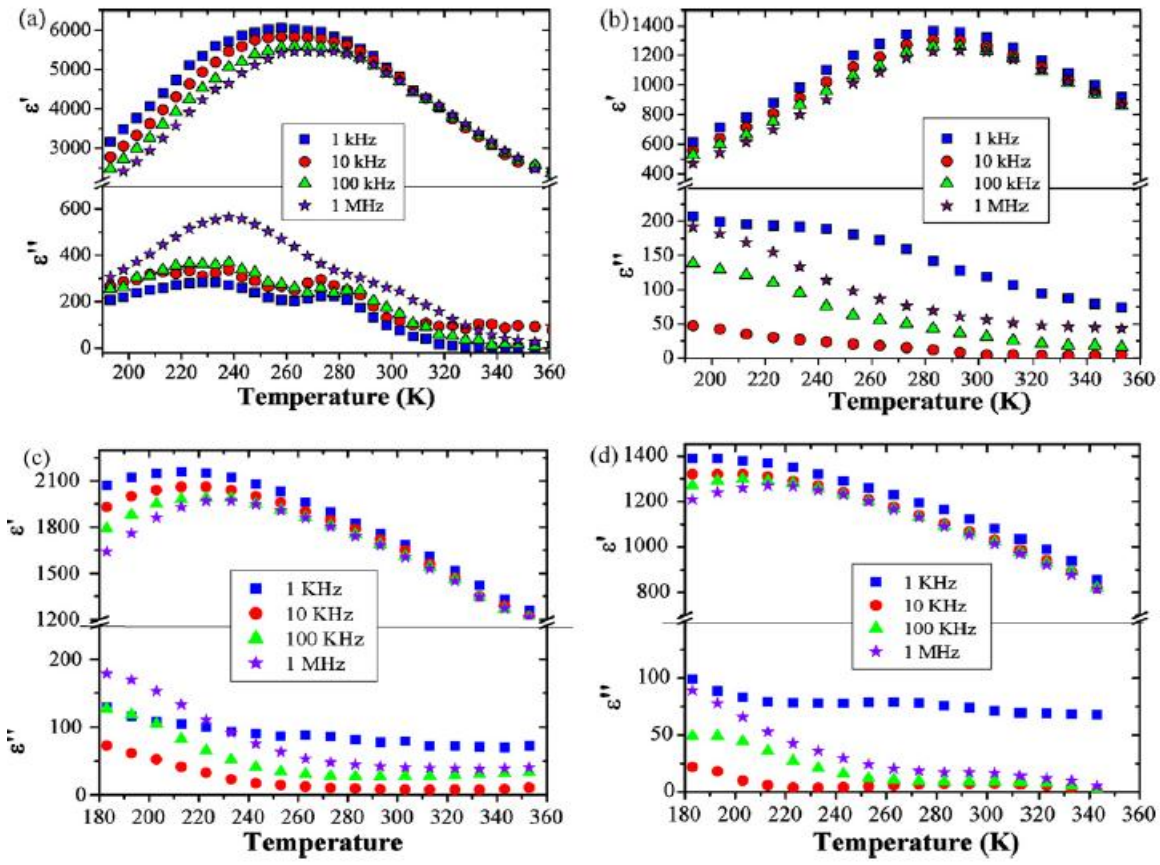

Figure 6.9 Temperature dependence of ε' and ε" at different frequencies for the $Ba_{1-x}Y_{2x/3}Zr_{0.25}Ti_{0.75}O_3$ ceramics **(a)** x = 0, **(b)** 0.01, **(c)** 0.025 and **(d)** 0.05

Figure 6.10 shows a plot of the inverse dielectric constant versus temperature at different frequencies. A clear deviation from the Curie-Weiss law can be seen at all

representative frequencies. The Curie temperature was determined from the graph by extrapolation of the reciprocal of the dielectric constant of the paraelectric region and the values obtained are given in Table 6.1.

Table 6.1 Parameters obtained from temperature dependent dielectric studies at 100 *kHz* on the composition of $Ba_{1-x}Y_{2x/3}Zr_{0.25}Ti_{0.75}O_3$ ceramics with different *Y* content.

$Ba_{1-x}Y_{2x/3}Zr_{0.25}Ti_{0.75}O_3$	x = 0	x = 0.01	x = 0.025	x = 0.05
T_m (K)	273(±1)	297(±1)	228(±1)	210(±1)
T_o (K)	308(±1)	319(±1)	265(±1)	241(±1)
C (10^5 K)	2.1	1.5	2.5	2.8
ΔT_m	88(±2)	70(±2)	79(±2)	87(±2)
T_{cw}	361(±2)	367(±2)	307(±2)	297(±2)
ε_m	5572(±3)	1262(±3)	2004(±3)	1297(±3)
γ	1.72	1.65	1.77	1.83

Modified Curie-Weiss law has been describe for diffuseness of a phase transition as explained in Chapter 3. Plots of log ($1/\varepsilon' - 1/\varepsilon_m$) vs $log\ (T - T_m)$ at 100 *kHz* for various $Ba_{1-x}Y_{2x/3}Ti_{0.75}Zr_{0.25}O_3$ compositions are shown in Figure 6.11 (a) Linear relationships are observed. The slopes of the fitting curves are used to determine the parameters γ and are given in Table 6.2. The high values of γ show that the materials are highly disordered. The increased value of γ with higher *Y* content indicates an increase in diffusivity. The broadened dielectric maximum (in the ε' vs temperature curve) and its deviation from the Curie-Weiss law are the main characteristics of a diffuse phase transition of a material.

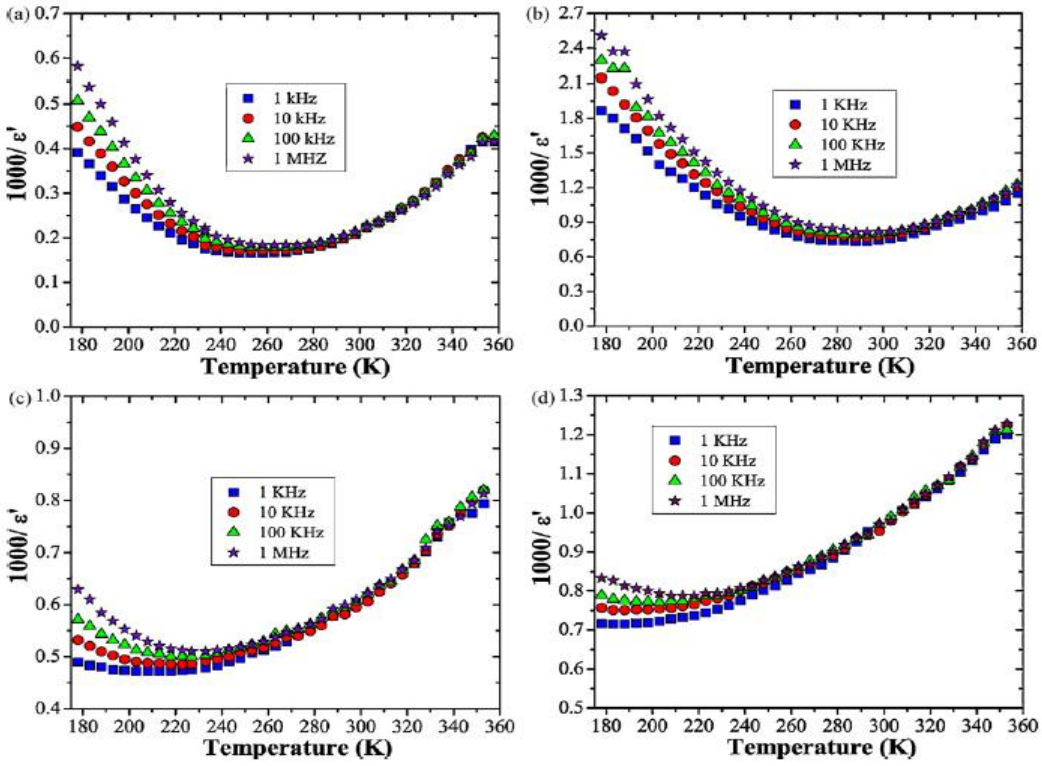

Figure 6.10 Inverse dielectric permittivity as a function of temperature (from 1 *kHz* to 1*MHz*) for the $Ba_{1-x}Y_{2x/3}Zr_{0.25}Ti_{0.75}O_3$ ceramics **(a)** x = 0, **(b)** 0.01, **(c)** 0.025 and **(d)** 0.05

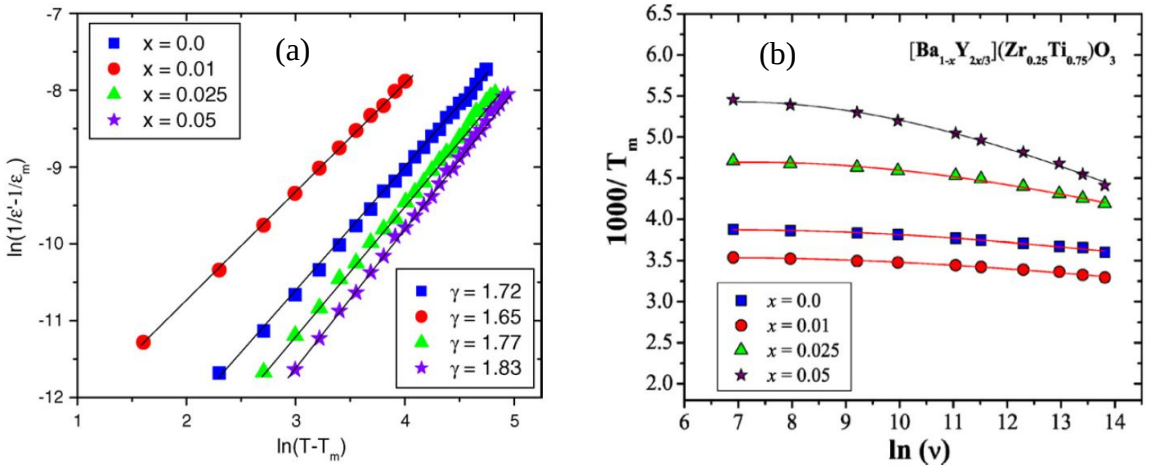

Figure 6.11 **(a)** $\log((1/\varepsilon') - (1/\varepsilon_m))$ as a function of $\log(T - T_m)$ performed at 100 *kHz* for the different compositions and **(b)** $(1/T_m)$ as a function of ln(f) for the $Ba_{1-x}Y_{2x/3}Zr_{0.25}Ti_{0.75}O_3$ceramics. The symbols are experimental points, while the line is obtained by the Vogel–Fulcher relation.

Table 6.2 Fitting parameters obtained by the Vogel–Fulcher equation for the different compositions of $Ba_{1-x}Y_{2x/3}Zr_{0.25}Ti_{0.75}O_3$ ceramics.

$Ba_{1-x}Y_{2x/3}Zr_{0.25}Ti_{0.75}O_3$	x = 0	x = 0.01	x = 0.025	x = 0.05
T_f (K)	128(±1)	143(±1)	108(±1)	93(±1)
E_a (eV)	0.1538(4)	0.1837(1)	0.0932(9)	0.0853(5)
υ_o $(10^{15}\ Hz)$	1.03 x 10^{11}	1.23 x 10^{11}	0.0924 x 10^{10}	0.0861 x 10^{10}

Figure 6.11 (b) shows the graph of $(1/T_m)$ as a function of ln(f) for the $Ba_{1-x}Y_{2x/3}Zr_{0.25}Ti_{0.75}O_3$ ceramics. The nonlinear nature indicates that the data cannot be fitted by the simple Debye equation. Therefore, the relaxation time of these ceramics must be expressed by the Vogel–Fulcher equation. The fitting parameters are displayed in Table 6.2. In this table, the fitting parameters are in good agreement with the Vogel–Fulcher equation, suggesting that the relaxor behavior of some materials is analogous to those observed in dipolar glasses with polarization fluctuations above the static freezing temperature. Another important point is that the activation energy and the pre-exponential factor are both consistent with thermally activated polarization fluctuations.

6.3.9 Electrical conductivity studies

6.3.9.1 Impedance Study

Figure 6.12 ((a) and (b)) shows impedance (Nyquist) plot of $Ba_{1-x}Y_{2x/3}Zr_{0.25}Ti_{0.75}O_3$ (x=0.025, 0.05) at different temperatures. The impedance plot shows depressed semicircular arcs with their centers lying below the real axis rather than on the real axis. The angle by which the semicircle is depressed below the real axis and the amount of inclination of the straight line are related to the width of the distribution

of the relaxation time. This suggests the poly-dispersive nature of the sample. Using the ZView commercial software, the impedance data were analyzed in order to obtain resistance and the capacitance. The observed features can be modeled by equivalent circuits as shown in chapter 3.

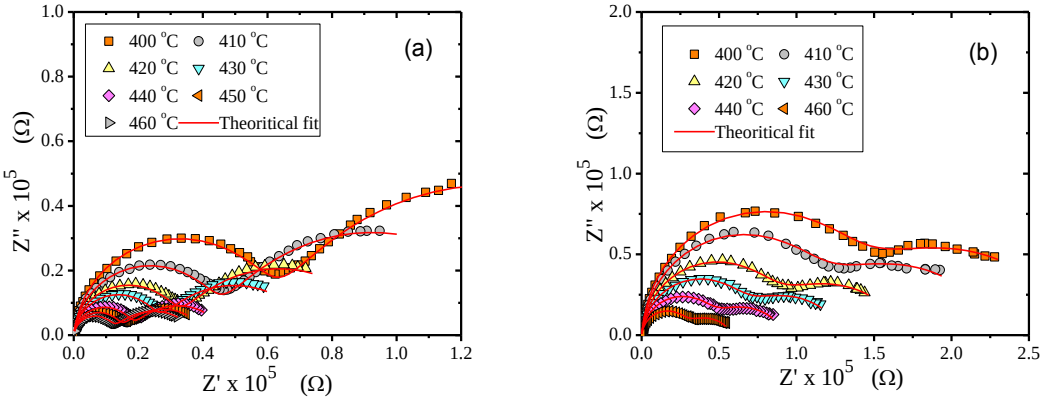

Figure 6.12 Nyquist plot of $Ba_{1-x}Y_{2x/3}Zr_{0.25}Ti_{0.75}O_3$ at different temperatures, **(a)** x = 0.025 and **(b)** x = 0.05

Table 6.3 Parameters obtained from temperature dependent impedance spectroscopy data for the $Ba_{1-x}Y_{2x/3}Zr_{0.25}Ti_{0.75}O_3$ ceramic sintered.

T	x = 0.025				x = 0.05			
^oC	CPE_g nF	CPE_{gb} nF	R_g KΩ	R_{gb} KΩ	CPE_g nF	CPE_{gb} nF	R_g KΩ	R_{gb} Ω
400	0.26	74	59.4	141.7	0.30	47.3	128.4	152.6
410	0.25	98	42.6	100.3	0.33	52.5	106.2	125.3
420	0.25	126	30.6	66.4	0.36	63.7	79.5	91.1
430	0.27	145	25.0	49.9	0.40	67.0	61.5	69.3
440	0.29	195	17.4	29.8	0.41	79.2	42.4	50.6
450	0.30	251	13.8	27.8	--	--	--	--
460	0.29	289	11.4	26.9	0.42	107	26.7	31.8

The impedance plot comprises two semicircular arcs to the electrical response due to grain interior and grain boundary polycrystalline material *(MacDonald, 1987)*. The symbol represents the experimental data and the solid line represents the

theoretical fitting. The R_g (bulk resistance) and R_{gb} (grain boundary resistance) from this fitting is shown in Table 6.3. The R_g and R_{gb} decreases with temperature indicating a typical Negative Temperature Coefficient of Resistance (NTCR) behavior, a property of a semi-conducting material.

6.3.9.2 AC and DC conductivity

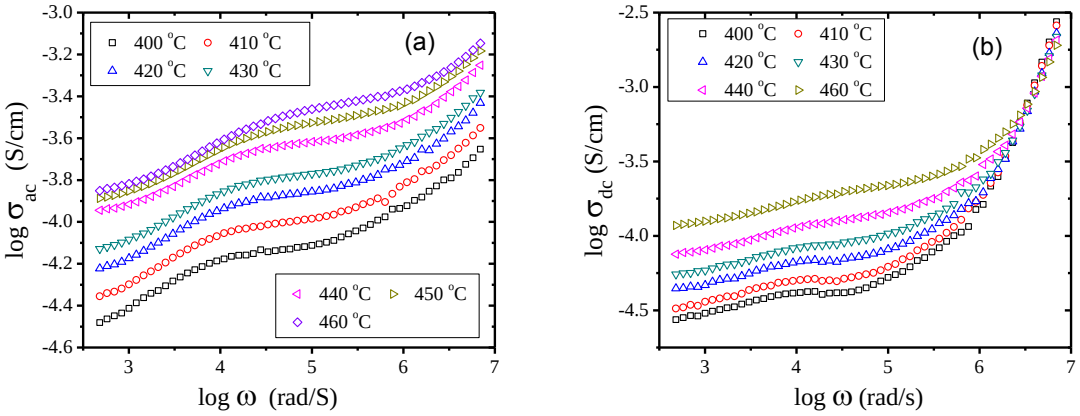

Figure 6.13 Frequency dependence of AC conductivity at different temperatures of $Ba_{1-x}Y_{2x/3}Zr_{0.25}Ti_{0.75}O_3$ ceramic, **(a)** x = 0.025 and **(b)** x = 0.05

Figure 6.13 shows the variation of conductivity as a function of frequency at various temperatures for $Ba_{1-x}Y_{2x/3}Zr_{0.25}Ti_{0.75}O_3$ ceramic. In the present work the DC conductivity at different temperatures has been extracted from the extrapolation of frequency independent plateau region from log σ versus log ω plot. Figure 6.14 shows the temperature dependence of DC conductivity. It shows a slope by a flat region and the slope obeys Arrhenius relation. The activation energy is found to be 0.49eV for x = 0.025 and 0.52eV for x = 0.05 of the $Ba_{1-x}Y_{2x/3}Zr_{0.25}Ti_{0.75}O_3$ from Arrhenius law fitting in DC conductivity. This may be due to the existence phase

transitions in the sample. The flat region is appearing just above the FE phase transition.

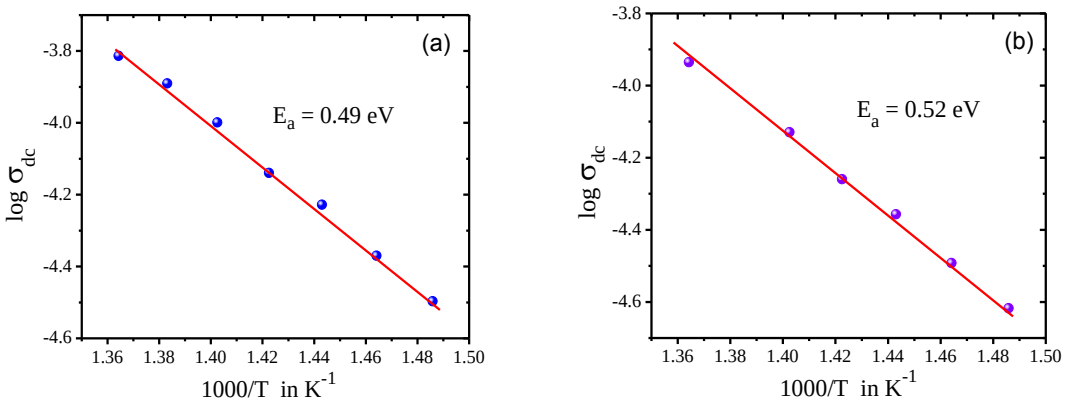

Figure 6.14 Arrhenius plot of DC conductivity for $Ba_{1-x}Y_{2x/3}Zr_{0.25}Ti_{0.75}O_3$ **(a)** x=0.025 and **(b)** 0.05

CHAPTER 7

CONCLUSION

The composition $BaZr_xTi_{1-x}O_3$ *(x=0.0, 0.05, 0.1, 0.15, 0.2, 0.25)* ceramic was prepared by the solid state reaction method. The substitution of Zr^{+4} [*R* (Zr^{4+})*=86 pm, R* (Ti^{4+})*=74.5 pm*] to Ti^{+4} increases the *d* spacing yielding the shift of (e.g. 110 type plane) diffraction peaks towards lower 2θ angle. This is a clear indication that Zr^{+4} is systematically dissolved in $BaTiO_3$ lattice in the studied composition range. The detailed structural study of $BaZr_{0.25}Ti_{0.75}O_3$ (BZT) has been done by Reitveld refinement which shows a cubic structure with space group *Pm*3*m*. The SEM micrograph indicated that this ceramic present large grain with irregular shape and its grain growth is related due to the matter transport mechanisms via grain boundary during the sintering process. The dielectric study of the composition shows relaxor behavior. The relaxor behavior is observed in BZT ceramics can be induced by many reasons such as a microscopic composition fluctuation, the merging of micro polar regions into macro polar regions, or a coupling of order parameter and local disorder mode through the local strain. In the solid solution of $BaZr_xTi_{1-x}O_3$, *Ba* ions occupy the A sites of the ABO_3 perovskite structure. *Zr* and *Ti* ions occupy the B sites, as the ionic radius of Zr^{4+} is larger than that of Ti^{4+} therefore inhomogeneous distribution of *Zr* ions in the *Ti* sites occurs and also mechanical stress in the grain. Stress was introduced into the lattice during cooling after the

sintering process, which is due to the transition from a cubic to rhombohedral phase below the Curie temperature.

The compound $(Ba_{1-x}Re_{2x/3}Zr_{0.25}Ti_{0.75})O_3$ with *Re= Bi, Dy, Y* has been synthesized by solid state reaction method. The single-phase formation of all the samples with in the studied range has been confirmed by x-ray diffraction technique. A distortion in the crystalline lattice is produced due to the substitution of Ba^{2+} by Re^{3+} ions. Based on the A-site vacancy defect compensation model, this substitution implies that for every two Re^{3+} ions put onto the A-site, one cationic vacancy must be created in order to maintain the charge neutrality of the perovskite structure. The distortion of the lattice structure may cause an increase in the short range harmonic restoring force in *Re* doped BZT ceramics. The scanning electron microscopy shows that the grain size decreases with increase in *Re* content in BZT. The dielectric study of heterovalent BZT ceramics shows relaxor behavior with decrease in dielectric constant and Curie temperature. The decrease in curie temperature may be due to the number of cationic vacancies increases with the increase of Re^{3+} content and higher distortion of the BZT lattice structure. Relaxor behaviour and the diffuseness of the ferroelectric phase transition in those materials can be explained as a consequence of Re^{3+} substitution for A-site Ba^{+2} ions in $Ba_{1-x}Re_{2x/3}Zr_{0.25}Ti_{0.75}O_3$ compounds. According to Krögere Vink equation, for every two Re^{+3} ($Re_{Ba}^{\bullet}$) substituting for Ba^{2+} ions only one A-site vacancy ($V_{Ba}^{''}$) is created, producing compositional fluctuation on a microscopic scale. The degree of relaxor behavior and diffuseness increases with increase in heterovalent ion doping in BZT ceramic

because ($Re^{\bullet}_{Ba}$) and ($V^{''}_{Ba}$) increase with increasing Ln^{3+} which increases the compositional inhomogeneity and distortion of the lattice.

The impedance spectroscopy study of $(Ba_{1-x}Re_{2x/3}Zr_{0.25}Ti_{0.75})O_3$ ceramics shows that the dielectric relaxation is of poly-dispersive non-Debye type. This happen may due to the presence of distributed elements in the material electrode system those results in the deviation from the pure semicircle in complex impedance plots. The Cole-Cole plots shows both grain and grain boundary effect It been observed that both grain and grain boundary resistance decreases with rise in temperature may be due to the lowering of barrier favoring the increase of mobility of charge carriers that adds to the conduction process. It indicates that the grain boundary effect have assisted in lowering the barrier to the motion of charge carriers paving the way for increased electrical transport with rise in temperature. There is increase in AC conductivity with heterovalent substitution in BZT ceramic with temperature at high frequencies which may be due to the release of space charge as a result of reduction in barrier properties of the material with rise in temperature.

The detailed structural study of $(Ba_{1-x}Y_{2x/3}Zr_{0.25}Ti_{0.75})O_3$, $x(=0.0,0.01,0.025,0.05)$ is done by super cell model, Fourier transform infrared spectroscopy , Fourier transform Raman scattering spectroscopy, X-ray absorption near-edge spectroscopy , Ultra-violete visible absorption spectroscopy and Photoluminescence. In the super cell, both Ti and Zr atoms (lattice formers) are bonded to six O atoms, forming the [TiO_6] and [ZrO_6] clusters. In the non-polar [ZrO6] clusters, the Zr atoms are located in a centro-symmetric position into the octahedron. On the other hand, in the polar [TiO_6] clusters, the Ti atoms are slightly displaced along the [001] direction (z-axis).

This displacement or distortion can be arising from the covalent character between the O-Ti-O bonds (directional orientations). FT-RS spectra, suggesting the occurrence of structural distortions on the polar [TiO_6] clusters at short-range. Also, the displacement and disappearance of some Raman-active modes were associated to the structural modifications induced by the [YO_6] clusters into the lattice. XANES spectra indicated that the Zr atoms minimize the structural disorder, while the Y atoms do not considerably contribute for the average Ti displacement into the polar [TiO_6] clusters. UV-vis spectra suggested an indirect allowed transition with the existence of intermediary energy levels (shallow or deep holes) within the band gap. These energy states are formed of O 2p, Ti 3d, Zr and Y 4d orbitals. Finally, the origin of the blue PL emission was related to the several radiative electronic transitions between these different energy levels. In addition, the Y-doped Ba ($Zr_{0.25}Ti0.75)O_3$ powders exhibited a high PL intensity when compared to the pure $Ba(Zr_{0.25}Ti_{0.75})O_3$. This result was attributed the formation and reorganization of Y 4d orbitals within the band gap.

CHAPTER 8

SUMMARY AND FUTURE WORK

The thesis work mainly deals with the investigation of dielectric properties of Barium Zirconium Titanate pervoskite. For the present study, all the samples were prepared in single phase by solid state reaction technique. Different experiments were carried out and the results were carefully analyzed to monitor the changes in the structure, electrical and optical properties of Barium Zirconium Titanate due to the substitution of heterovalent ion Bi^{+3}, Dy^{+3}, Y^{+3} on Ba site. This chapter presents a concise summary based on the results and discussions presented in the previous chapters on Barium Zirconium Titanate based ceramics, in four different sections. It also provides a brief note on the scope for the future work.

8.1 Phase formation and dielectric study of $BaZr_xTi_{1-x}O_3$ ceramics

The $BaZr_xTi_{1-x}O_3$ ceramic was prepared by the solid state reaction method. The X-ray diffraction patterns reveal that the peak shifts towards the lower angle with increasing Zr content in $BaTiO_3$ ceramic indicating increase in lattice parameter. In the present study the parent composition $BaZr_{0.25}Ti_{0.75}O_3$ is chosen due to its relaxor

behavior, high dielectric constant at room temperature and the transition temperature closed to room temperature. X-ray diffraction patterns and Rietveld refinement confirmed that $BaZr_{0.25}Ti_{0.75}O_3$ ceramic shows a cubic structure with space group *Pm*3*m*. EDXS spectra showed that the chemical compositional of $Ba[Zr_{0.25}Ti_{0.75})O_3$ ceramic without the presence of deleterious phases. The SEM micrograph indicated that this ceramic present large grains with irregular shapes and its grains growth is related due to the matter transport mechanisms via grain boundary during the sintering process. The dielectric measures showed a typical relaxor-like behavior. The experimental T_m data indicated a good agreement with the Vogel-Fulcher equation. The empirical parameters (ΔT_m, ΔT_{res} and ΔT_{cw}) confirmed the relaxor behavior for the $Ba(Zr_{0.25}Ti_{0.75})O_3$ ceramic The value of grain boundary resistance (R_{gb}) at different temperatures was estimated from the complex impedance spectrum. This plot indicates the changes in grain boundary resistance at elevated temperatures representing the role of grain boundaries in electrical conduction process of the material. The decrease in grain boundary resistance with rise in temperature may be due to the lowering of barrier favoring the increase of mobility of charge carriers that add to the conduction process. The higher value of activation energy due to grain boundary then grain contribution suggests that the grain boundaries require more activation energy for hopping than the grains. The conduction mechanism for grains and grain boundaries are different.

8.2 Frequency and temperature dependence study of heterovalent Bismuth substituted $BaZr_{0.25}Ti_{0.75}O_3$ ceramic

The polycrystalline $Ba_{1-x}Bi_{2x/3}Zr_{0.25}Ti_{0.75}O_3$ (x=0.025, 0.05) ceramic has been prepared by solid state reaction route. The samples are found to be well crystallized in single phase. The SEM micrographs suggest that materials comprise of polycrystalline microstructure and the concentration of dopant affects the microstructure. The sample shows well developed and relatively equal shaped grains. The size of the grains decreases with the increase in Bi concentration. The dielectric response indicates relaxor behavior with decrease in transition temperature, dielectric constant (ε') and loss tangent ($tan\delta$) as Bi content increases in the $BaZr_{0.25}Ti_{0.75}O_3$ ceramics. The decrease in transition temperature may be due to the decrease in grain size. The diffusivity increases as the Bi content increases in the $BaZr_{0.25}Ti_{0.75}O_3$ ceramics. The electrical properties of the $Ba_{1-x}Bi_{2x/3}Zr_{0.25}Ti_{0.75}O_3$ (x = 0.025) samples have been studied by impedance spectroscopy which shows polydispersive nature of the samples. Two semicircles are shown at higher temperature, the high frequency semicircle attributed to the bulk (grain) property where as the low frequency one attributed to the presence of grain boundary. This typical behavior suggests the presence of hopping mechanism between the allowed sites. The sample shows negative temperature coefficient of resistivity (NTCR) effect as the bulk resistance decreases with increase in temperature. The electrical relaxation process occurring in the material has been found to be temperature dependent. Modulus analysis has established the possibility of hopping mechanism for electrical transport processes in the system. The plateau region of the conductivity at higher frequency and temperature may be related to the space

charge. An increase in dc conductivity (i.e., bulk and grain boundary) with rise in temperature is also observed. The temperature dependence DC conductivity obeys Arrhenius relation. The comparison of frequency dependence plots of *M"* and *Z"* show that the conductivity relaxation is non –Debye in nature and activation energy responsible for relaxation was found to be almost the same as that of activation energy obtained from the conductivity data. The *ac* conductivity data were used to evaluate the density of states at Fermi level binding energy and thermal conductivity.

8.3 Investigation of Dielectric property and Glassy behavior of Dysprosium doped $BaZr_{0.25}Ti_{0.75}O_3$ Ceramic

The polycrystalline $Ba_{1-x}Dy_{2x/3}Zr_{0.25}Ti_{0.75}O_3$ (x= 0.01, 0.025, 0.05) ceramic has been prepared by solid state reaction route. The samples are found to be well crystallized in single phase and there is decrease in lattice parameter. The SEM micrographs suggest that materials comprise of polycrystalline microstructure and the size of the grains decreases with the increase in Dy concentration. The dielectric study reveals that the material shows relaxor behavior with in the studied range with decrease in magnitude of dielectric constant (ε') and loss tangent ($tan\delta$) as Dy content increases. The quantitative characterization and comparison of the relaxor behavior based on empirical parameters confirmed the diffusivity increases as the Dy content increases. The observed high value of γ and relaxation strength are may be due to the large difference in ionic radius of Ba^{2+} (2.78 $\AA$) and Dy^{3+} (1.75 $\AA$) at the A-site of the perovskite structure. The experimental T_m data points are in good agreement

with the Vogel–Fulcher relation. The quantitative characterization of the relaxor behavior based on empirical parameters (ΔT_m, ΔT_{res}, and ΔT_{cw}) confirms the relaxor behavior of the Composition $Ba_{1-x}Dy_{2x/3}Ti_{0.75}Zr_{0.25}O_3$. The experimental data are fitted with theoretical equations and the parameters are reported.

8.4 Structural, Electrical and Optical study of heterovalent Yttrium (Y^{3+}) doped $BaZr_{0.25}Ti_{0.75}O_3$ ceramics

$Ba_{1-x}Y_{2x/3}Zr_{0.25}Ti_{0.75}O_3$ powders with different Y concentrations (x = 0, 0.025 and 0.05) were prepared by solid state reaction under heat treatment conditions performed at 1350^0C for 6 *h*. X-ray diffraction patterns showed that all powders have a cubic structure with space group Pm3m. Secondary phases were not detected in the diffractograms, thus indicating that the Y atoms were incorporated into the $Ba(Zr_{0.25}Ti_{0.75})O_3$ matrix. Moreover, it was observed that the addition of Y leads to a slight contraction of the unit cell volume. The SEM micrographs revealed that the Y content induced a rapid matter transport by means of grain-boundary, resulting in the formation of necks between the grains. In spite of the cubic structure, it was detected seven Raman-active modes in the FT-RS spectra, suggesting the occurrence of structural distortions on the polar [TiO_6] clusters at short-range. Also, the displacement and disappearance of some Raman-active modes were associated to the structural modifications induced by the [YO_6] clusters into the lattice. The displacement verified in the absorption band corresponding to the O-Ti-O and O-Zr-O bonds was correlated to the stresses induced on the [TiO_6] and [ZrO_6] clusters, as a consequence of the substitution of Ba atoms by those of Y. XANES spectra indicated

that the Zr atoms minimize the structural disorder, while the Y atoms do not considerably contribute for the average Ti displacement into the polar [TiO_6] clusters. UV-vis spectra suggested an indirect allowed transition with the existence of intermediary energy levels (shallow or deep holes) within the band gap. These energy states are formed of O 2p, Ti 3d, Zr and Y 4d orbitals. Finally, the origin of the blue PL emission was related to the several radiative electronic transitions between these different energy levels. In addition, the Y-doped $Ba(Zr_{0.25}Ti_{0.75})O_3$ powders exhibited a high PL intensity when compared to the pure $Ba(Zr_{0.25}Ti_{0.75})O_3$. This result was attributed the formation and reorganization of Y 4d orbitals within the band gap. In terms of electric measurements, the reduction in the dielectric permittivity magnitude and the shifting of ε_m values to higher temperatures suggested a relaxor behavior for this material. The quantitative analysis based on the empirical parameters (T_m, T_{res} and T_{cw}) confirmed the relaxor nature of $Ba_{1-x}Y_{2x/3}(Zr_{0.25}Ti_{0.75})O_3$ ceramics. The impedance plot shows that at higher temperatures, there is a contribution from grain boundary to the total impedance of the system.

FUTURE DIRECTIONS

The scope of the thesis may be strengthened further by the follows;

- To provide further, an in depth analysis of the structural and microstructure of the compounds. The temperature variation of X-ray diffraction study to observe the changes in the crystal structure, Transmission Electron Microscopy (TEM) study to understand the domain wall motion and High Resolution Transmission Electron Microscopy (HRTEM) to observe the degree of order, X-ray Photoelectron Spectroscopy (XPS) for compositional analysis. The necessity of X-ray Photoelectron Spectroscopy arises because of the Energy Dispersive X-ray spectroscopy is not a proper experimental tool for the present situation and temperature variation of Raman spectroscopy will be carried out to extract further information to understand the relaxor behaviour.

- For application point of view, piezoelectric and pyroelectric measurement should be carried out. Research can be further extended to enhance the piezoelectrcity in the system by suitable cation substitution.

- It will be interesting to grow thin film of the substituted $BaZr_{0.25}Ti_{0.75}O_3$ compositions to realize epitaxial/nano structured films to study the ferroelectric behaviour. It is proven in case of lead based ferroelectric materials that the oriented/epitaxial thin films are superior in functional properties compared to their bulk counterparts. Hence, the functional properties of substituted $BaZr_{0.25}Ti_{0.75}O_3$ compositions can be significantly increased by fabricating thin films which could find applications in microwave and memory storage devices.

REFERENCES

1. Aliouane. K, Guehria-Laidoudi. A, Simon. A, Ravez. J, (2005) *"Study of new relaxor materials in $BaTiO_3BaZrO_3La_{2/3}TiO_3$ system"* Solid State Ionics 7, 1324.

2. Ang. C, Yu. Z, Jing. Z, Lunkenheimer. P, Loidl. A, (2000) *"Dielectric spectra and electrical conduction in Fe-doped $SrTiO_3$"*, Phys. Rev. B 61, 3922.

3. Anicete-Santos. M, Cavalcante. L.S, Orhan. E, Paris. E.C, Simoes. L.G.P, Joya. M.R, Rosa. I.L.V, de Lucena. P.R, Santos. M.R.M.C, Santos-Júnior. L.S, Pizani. P.S, Leite. E.R, Varela. J.A, Longo. E, (2005) *"The role of structural order-disorder for visible intense photoluminescence in the $BaZr_{0.5}Ti_{0.5}O_3$ thin films"*, Chemical Physics, 316 260.

4. Austin.I.G, N.F. Mott, (1969) *"Polarons in crystalline and non-crystalline materials"*, Adv. Phys. 18, 41.

5. Balaya. P, Jamnik. J, Fleig. J, and Maier. J, (2006) *"Mesoscopic electrical conduction in nanocrystalline $SrTiO_3$"*, Appl. Phys. Lett. 88, 062109.

6. Begg. B.D, Finnie. K.S, Vance. E.R, (1996) *"Raman study of the relationship between room-temperature tetragonality and the curie point of barium titanate"*, Journal of the American Ceramic Society, 79, 2666.

7. Bera. J, Rout. S.K, (2005) *"On the formation mechanism of $BaTiO_3$–$BaZrO_3$ solid solution through solid-oxide reaction"* Mater. Lett. 59, 135.

8. Burfoot. J.C, (1967) "*Ferroelectrics",* Van Nostrand, New York.

9. Buscaglia. M.T, Buscaglia. V, Viviani. M, Nanni. P, Hanuskova. M, (2000) *"Influence of foreign ions on the crystal structure of $BaTiO_3$"*, Journal of the European Ceramic Society, 20, 1997.

10. Cavalcante. L.S, Gurgel. M.F.C, Paris. E.C, Simoes. A.Z, Joya. M.R, Varela. J.A, Pizani. P.S, Longo. E, (2007) *"Combined experimental and theoretical investigations of the photoluminescent behavior of $Ba(Ti,Zr)O_3$ thin films"*, ActaMaterialia, 55, 6416.

11. Cavalcante. L.S, Marques. V.S, Sczancoski. J.C, Escote. M.T, Joya. M.R, Varela. J.A, Santos. M.R.M.C, Pizani. P.S, Longo. E, (2008) "*Synthesis, structural refinement and optical behavior of $CaTiO_3$ powders: A comparative study of processing in different furnaces"*, Chemical Engineering Journal, 143, 299.

12. Cavalcante. L.S, Sczancoski. J.C, De Vicente. F.S, Frabbro. M.T, Siu. Li.M, Varela. J.A, Longo. E, (2009) *"Microstructure, dielectric properties and optical band*

gap control on the photoluminescence behavior of Ba[$Zr_{0.25}Ti_{0.75}$]O_3 thin films", J. Sol–Gel Sci. Technol. 49, 35.

13. Chaves. A, Katiyar. R.S, Porto. S.P.S, (1974) "*Coupled modes with A_1 symmetry in tetragonal $BaTiO_3$"*, Physical Review B, 10, 3522.

14. Chazono. H, Inomata. Y, Kohzu. N, Kishi. H, (2000) *"Influence of Firing Temperature on the Microstructure and Electrical Properties of BTZ based Dielectric Materials for Ni-MLCC"*, Key Engineering Materials, 181-182, 11.

15. Cheng, Z. Y, Katiyar. R. S, Yao. X and Guo. A, (1997) *"Dielectric behavior of lead magnesium niobate relaxors"*, Phys. Rev. B, 55, 8165.

16. Cheng, Z. Y, Zhang. L. Y, and Yao. X, (1996) *"Investigation of glassy behavior of lead magnesium niobate relaxors"*, J. Appl. Phys., 79, 8615.

17. Chou. X, Zhai. J, Jiang. H, Yao. X, (2007) *"Dielectric properties and relaxor behavior of rare-earth (La, Sm, Eu, Dy, Y) substituted barium zirconium titanate ceramics"*, J. Appl. Phys. 102, 084106.

18. Chou. X, Zhai. J, Yao. X, (2008) *"Relaxor behavior and dielectric properties of La_2O_3-doped barium zirconium titanate ceramics for tunable device applications"*, Mater. Chem. Phys. 109, 125.

19. Ciomaga. C, Viviani. M, Buscaglia. M.T, Buscaglia. V, Mitoseriu. L, Stancu. A, Nanni. P, (2007) "*Preparation and characterisation of the Ba(Zr,Ti)O_3 ceramics with relaxor properties"*, J. Eur. Ceram. Soc. 27, 4061.

20. Corker, D. L, A. M. Glazer, J. Dec, K. Roleder and R. W. Whatmore, (1997) *"A Re-investigation of the crystal structure of the perovskite $PbZrO_3$ by x-ray and neutron diffraction"*, Acta Cryst. B, 53, 135.

21. Crocombette. J.P, Jollet. F, (1994) *"Site selectivity in ZrO_2-doped Y_2O_3 evidenced by x-ray absorption spectra calculations"*, Journal of Physics: Condensed Matter, 6, 8341.

22. Cross, L. E. (1987) *"Relaxor ferroelectrics"*, Ferroelectrics, 76, 241.

23. Cross. L.E, (1994) "Relaxor ferroelectrics: an overview", *Ferroelectrics,* 151, 305.

24. De Lazaro. S, Milanez. J, De Figueiredo. A.T, Longo. V.M, Mastelaro. V.R, De Vicente. F.S, Hernandes. A.C, Varela. J.A, Longo. E, (2007) *"Relation between photoluminescence emission and local order-disorder in the $CaTiO_3$ lattice modifier"*, Applied Physics Letters, 90, 111904.

25. Dixit. A, Majumder. S.B, Dobal. P.S, Katiyar. R.S, Bhalla. A.S, (2004) *"Phase transition studies of sol-gel deposited barium zirconate titanate thin films"*, Thin Solid Films, 447, 284.

26. Dixit. A, Majumder. S.B, Katiyar. R.S, Bhalla. A.S, (2003) *"Relaxor behavior in sol–gel-derived $BaZr_{(0.40)}Ti_{(0.60)}O_3$ thin films"*, Appl. Phys. Lett. 82, 2679.

27. Dobal. P. S, Dixit. A, Katiyar. R. S, Yu. Z, Guo. R, Bhalla. A. S, (2001) *"Micro-Raman scattering and dielectric investigations of phase transition behavior in the $BaTiO_3$-$BaZrO_3$ system"*, Journal of Applied Physics, 89, 8085.

28. Domenico. Jr.M.D, Wemple. S.H, Porto. S.P.S, Buman. P.R, (1968) *"Raman Spectrum of Single-Domain $BaTiO_3$"*, Phys. Rev.174, 522.

29. Duan. C, Yuan. J, Zhao. J, (2005) *"Luminescence properties of efficient X-ray phosphors of $YBa_3B_9O_{18}$, $LuBa_3(BO_3)_3$, α-$YBa_3(BO_3)_3$ and $LuBO_3$"*, Journal of Solid State Chemistry, 178, 3698.

30. *E-Abd El-Wahabb,* (2000) *"Electrical and optical properties of $Sb_{31}Se_{36}Ag_{33}$"*, Vacuum 57, 339.

31. El-Sayed. A. M, (2002) *"Effect of chromium substitutions on some properties of NiZn ferrites"*, Ceram. Int. 28 651.

32. Farges. F, Brown. Jr.G.E, Rehr. J.J, (1997) *"Ti K-edge XANES studies of Ti coordination and disorder in oxide compounds: Comparison between theory and experiment"*, Physical Review B - Condensed Matter and Materials Physics, 56, 1809.

33. Farhi. R, Marssi. E l, Simon. M.A, Ravez. J, (1999) *"A Raman and dielectric study of ferroelectric $Ba(Ti_{1-x}Zr_x)O_3$ ceramics"*, J. Eur. Phys. B, 9, 599.

34. Finger. L.W, Cox. D.E, Jephcoat. A.P, (1994) *"A correction for powder diffraction peak asymmetry due to axial divergence"*, J. Appl. Crystallogr. 27, 892.

35. Frenkel. A.I, Ehre. D, Lyahovitskaya. V, Kanner. L, Wachtel. E, Lubomirsky. I, (2007) *"Origin of polarity in amorphous $SrTiO_3$"*, Physical Review Letters, 99, 215502.

36. Frenkel. A.I, Feldman. Y, Lyahovitskaya. V, Wachtel. E, Lubomirsky. I, (2005) *"Microscopic origin of polarity in quasiamorphous $BaTiO_3$"*, Phys. Rev.B 71, 024116.

37. Ganguli, M., Bhat. M. H and Rao. K. J, (1999) *"Lithium transport in Li_2SO_4–Li2O–B_2O_3"*, Phys. Chem. Glasses, 40, 297.

38. Gerhardt.R, (1994) *"Impedance and dielectric spectroscopy revisited: Distinguishing localized relaxation from long-range conductivity"*, J. Phys. Chem. Solids 55, 1491.

39. Ghosh, S and Ghosh. A, (2002) *"Electrical conductivity and conductivity relaxation in mixed alkali fluoride glasses"*, Solid State Ionics, 149, 67.

40. Glazer, A. M, (1975) *"Simple ways of determining perovskite structures"*, Acta Cryst. A, 31, 756.

41. Glazer, A. M. (1972) *"The classification of tilted octahedra in perovskites"*, Acta Cryst. B, 28, 3384.

42. Guo. Y, Kakimoto. K, and Ohsato. H, (2004) *"Ferroelectric-relaxor behavior of $(Na_{0.5}K_{0.5})NbO_3$-based ceramics"*, J. Phys. Chem. Solids. 65, 1831.

43. Guo. Y, Kakimoto. K, Ohsato. H, (2004) *"Ferroelectric-relaxor behavior of $(Na_{0.5}K_{0.5})NbO_3$ based ceramics"*, J. Phys. Chem. Solids, 65, 1831.

44. Gurgel. M.F.C, Espinosa. J.W.M, Campos. A.B, Rosa. I.L.V, Joya. M.R, Souza. A.G, Zaghete. M.A, Pizani. P.S, Leite. E.R, Varela. J.A, Longo. E, (2007) *"Photoluminescence of crystalline and disordered BTO:Mn powder: Experimental and theoretical modeling"*, Journal of Luminescence, 126, 771.

45. Hennings. D, Schell. H, Simon. G, (1982) *"Diffuse Ferroelectric Phase Transitions in $Ba(Ti_{1-y}Zr_y)O_3$ Ceramics*", J. Am. Ceram. Soc. 65, 539.

46. Hennings. D, Schnell. A, Simon. G, (1982) *"Diffuse ferroelectric phase transitions in $Ba(Ti_{1-y}Zr_y)O_3$ ceramics"*, Journal of the American Ceramic Society, 65, 539.

47. Hodge, I. M., Ingram. M. D and West. A. R, (1976) *"Impedance and modulus spectroscopy of polycrystalline solid electrolytes"*, J. Electroanal. Chem., 74, 125.

48. Hoffmann, S. and R. M. Waser (1997) *"Dielectric properties, leakage behaviour, and resistance degradation of thin films of the solid solution series $Ba(Ti_{1-y}Zr_y)O_3$"*, Integrated Ferroelectrics, 17, 141

49. Hosono.Y, Harada.K, Yamashita.Y, (2001) *"Crystal Growth and Electrical Properties of Lead-Free Piezoelectric Material $(Na_{1/2}Bi_{1/2})TiO_3$–$BaTiO_3$"*, Jpn.J.Appl.Phys. 40, 5722.

50. Howell, F. S., Bose. R. A, Macedo. P. B and Moynihan. C. T, (1974) *"Electrical relaxation in a glass-forming molten salt"*, J. Phys. Chem., 78, 639.

51. Hwang. J.H, Han. Y.H, (2001) *"Dielectric properties of erbium doped barium titanate"*, Japanese Journal of Applied Physics, Part 1 (Regular Papers, Short Notes & Review Papers), 40, 676.

52. Irvine J.T.S, Sinclair. D.C, and West. A.R, (1990) *"Electroceramics: Characterization by Impedance Spectroscopy"*, Adv. Mater, 2, 132.

53. Fritesberg. J, (1977) "*Proc. 4th Int. Meeting on Ferroelectricity*", Leningrad

54. Jaffe. B, Cook. W.R, Jaffe. H, **(**1971) *"Piezoelectric Ceramics",* Academic Press, London and New York.

55. Jing. Z, Ang. C, Yu. Z, Vilarinho. P.M, Baptista. J.L, (1999) *"Incorporation of yttrium in barium titanate ceramics"*, Journal of the American Ceramic Society, 82, 1345.

56. Jona. F, Shirane. G, (1962) "*Ferroelectric Crystals",* Pergamon Press, Oxford.

57. Jonscher. A.K, (1977) *"The 'universal' dielectric response"*, Nature 267, 673.

58. Kang. S.J.L, *"Sintering-Densification"*, Grain Growth and Microstructure, Amsterdam: Elsevier, 1o Edit. (2005) 39.

59. Kanzig. W, (1957) "*Ferroelectrics and Antiferroelectrics",* Academic Press, New York.

60. Karan. N.K, Katiyar. R.S, Maiti. T, Guo. R, Bhalla. A.S, (2009) *"Raman spectral studies of Zr^{4+}-rich $BaZr_xTi_{1-x}O_3(0.5\leq x\leq 1)$ phase diagram"*, J. Raman Spectrosc, 40, 370.

61. Kazaoui. S, Ravez. J, (1993) *"Dielectric relaxation in Ba(Ti0.8Zr0.2)O3 ceramics prepared from sol-gel and solid state reaction powders"*, Journal of Materials Science, 28, 1211.

62. Kell. R. C, Hellicar. N. J, (1956) *"Structural transitions in barium titanate zirconate transducer materials"*, Acustica, 6, 235.

63. Kirillov. V.V, Isupov. V.A, (1973) *"Relaxation polarization of $PbMg_{1/3}Nb_{2/3}O_3$ (PMN)-A ferroelectric with a diffused phase transition"*, Ferroelectrics, 5, 3.

64. Kishi. H, Kohzu. N, Sugino. J, Ohsato. H, Iguchi. Y, Okuda. T, (1999) *"Effect of rare-earth (La, Sm, Dy, Ho and Er) and Mg on the microstructure in $BaTiO_3$"*, Journal of the European Ceramic Society, 19, 1043.

65. Knight, K. S, (1994) *"Structural phase transitions in $BaCeO_3$"*, Solid State Ionics, 74, 109.

66. Kreisel. J, Bouvier. P, Maglione. M, Dkhil. B, Simon. A, (2004) *"High-pressure Raman investigation of the Pb-free relaxor $BaTi_{0.65}Zr_{0.35}O_3$"*, Physical Review *B* - Condensed Matter and Materials Physics, 69, 921041.

67. Lanfredi, S., Saia. P. S, Lebullenger. R and Hernandes. A. C, (2002) *"Electric conductivity and relaxation in fluoride, fluorophosphates and phosphate glasses: analysis by impedance spectroscopy"*, Solid State Ionics, 146, 329.

68. Larson. A.C, Von Dreele. R.B, (2000) "*Generalized structure analysis system (GSAS)"*, Los Alamos National Laboratory Report, USA, LAUR 86.

69. Lee. S.J, Kwak. M.H, Moon. S.E, Ryu. H.C, Kim. Y.T, Kang. K.Y, (2005) *"Dielectric properties of paraelectric $Ba(Zr,Ti)O_3$ thin films for tunable microwave applications"*, Integr. Ferroelectr. 77, 93.

70. Lee. W.-H, Hennings. D, Lee. Y.-C, (2001) *"Effect of Dy-Doping on Resistance Degradation of Multilayer Ceramic Capacitors with Ni Electrodes under the Highly Accelerated Life Test"*, J. Ceram. Soc. Jpn. 109, 823.

71. Lin. M.-H, Lu. H.-Y, (2002) *"Site-occupancy of yttrium as a dopant in BaOexcess BaTiO3"*, Materials Science and Engineering A, 335, 101.

72. Lines. M.E, Glass. A.M, (1977) "*Principles and Applications of Ferroelectrics and Related Materials",* Clarendon Press, Oxford.

73. Longo. V.M, Cavalcante. L.S, Erlo. R, Mastelaro. V.R, de Figueiredo. A.T, Sambrano. J.R, de Lazaro. S, Freitas. A.Z, Gomes. L, Vieira. N.D, Varela. J.A, Longo. E, (2008) *"Strong violet-blue light photoluminescence emission at room temperature in $SrZrO_3$: Joint experimental and theoretical study"*, Acta Materialia, 56, 2191.

74. Macdonald, J. R, (1987) *"Impedance Spectroscopy Emphasizing Solid materials and Systems"*, John Wiley and Sons, New York.

75. Maiti. T, Alberta. E, Guo. R, Bhalla. A.S, (2006) *"The polar cluster like behavior in Ti^{4+} substituted $BaZrO_3$ ceramics"*, Materials Letters, 60, 3861.

76. Maiti. T, Guo. R, Bhalla. A.S, (2006) *"The evolution of relaxor behavior in Ti^{4+} doped $BaZrO_3$ ceramics"*, Journal of Applied Physics, 100, 114109.

77. Maiti. T, Guo. R, Bhalla. A.S, (2007) *"Enhanced electric field tunable dielectric properties of $BaZr_xTi_{1-x}O_3$ relaxor ferroelectrics"*, Appl. Phys. Lett. 90, 182901.

78. Makovec. D, Samardzija. Z, Delalut. U, Kolar. D, (1995) *"Defect structure and phase relations of highly lanthanum-doped barium titanate"*, Journal of the American Ceramic Society, 78, 2193.

79. Martirena. H.T, Burfoot. J.C, (1974) *"Grain-size and pressure effects on the dielectric and piezoelectric properties of hot-pressed PZT-5"*, Feroelectrics 7, 151.

80. McQuarrie. M, Behnke. F.W, (1954) *"Structural and dielectric studies in the system (Ba,Ca)(Ti,Zr)O_3"*, Journal of the American Ceramic Society, 37, 539.

81. Megaw, H.D, Darlington. C.N.W, (1975) *"Geometrical and structural relations in the rhombohedral perovskites"*, Acta Cryst. A, 31, 161.

82. Megaw. H.D, (1957) "*Ferroelectricity in Crystals",* Methuen and Co., London.

83. Menard. L.D, Wang. Q, Kang. J.H, Sealey. A.J, Girolami. G.S, Teng. X, (2009) *"Structural characterization of bimetallic nanomaterials with overlapping x-ray absorption edges"*, Phys. Rev. B 80, 064111.

84. Mollah.S, Som.K.K, Bose.K, Chaudri. B.K, (1993) *"AC conductivity in $Bi_4Sr_3Ca_3Cu_yO_x$ (y=0–5) and $Bi_4Sr_3Ca_{3-z}Li_zCu4O_x$ (z=0.1–1.0) semiconducting oxide glasses"*, J. Appl. Phys. 74, 931.

85. Moreira. M.L, Mambrini. G.P, Volanti. D.P, Leite. E.R, Orlandi. M.O, Pizani. P.S, Mastelaro. V.R, Paiva-Santos. C.O, Longo. E, Varela. J.A, (2008) *"Hydrothermal Microwave: A New Route to Obtain Photoluminescent Crystalline $BaTiO_3$ Nanoparticles"*, *Chem. Mater*. **20**, 5381.

86. Morrison. F.D, Sinclair. D.C, West. A.R, (1999) *"Electrical and structural characteristics of lanthanum-doped barium titanate ceramics"*, Journal of Applied Physics, 86, 6355.

87. Mott. N.F, (1990) "*Metal Insulator Transitions"*, Taylor and Francis, London.

88. Moulson. A.J, Herbert. J.M, (1990) "*Electroceramics",* Chapman and Hall Ltd., London.

89. Neirman, S. (1988) *"Curie point temperature of $Ba(Ti_{1-x}Zr_x)O_3$ solid solutions"*, Journal of Materials Science, 23, 3973.

90. Neirman. S, (1988) *"Curie point temperature of Ba(Ti1-xZrx)O3 solid solutions"*, Journal of Materials Science, 23, 3973.

91. Nowick, A. S. and Lim. B. S, (1994) *"Analysis of ac conductivity data for Na2O:3SiO2 glass by stretched exponential and Jonscher power-law method"*, J. Non-Cryst. Solids, 172-174, 1389.

92. Nye. J.F, (1957) "*Physical Properties of Crystals",* Oxford University Press, Oxford.

93. Okazaki. A, Suemune. Y, (1961) *"The crystal structure of $KCuF_3$"*, J. Phys. Soc. Jpn., 16, 176.

94. Orhan. E, Varela. J.A, Zenatti. A, Gurgel. M.F.C, Pontes. F.M, Leite. E.R, Longo. E, Pizani. P.S, Beltran. A, Andres. J, (2005) *"Room-temperature photoluminescence of $BaTiO_3$: Joint experimental and theoretical study"*, Phys. Rev. B 71, 085113.

95. Ostos. C, Mestres. L, Martinez-Sarrion. M.L, Garcia. J.E, Albareda. A, Perez. R, (2009) *"Synthesis and characterization of A-site deficient rare-earth doped $BaZr_xTi_{1-x}O_3$ perovskite-type compounds"*, Solid State Sciences, 11, 1016.

96. Park.K.J, Kima.C.H, Yoon.Y.J, Songa.S.M, Kima.Y.T, Hur.K.H, (2009) *"Doping behaviors of dysprosium, yttrium and holmium in $BaTiO_3$ ceramics",* Journal of the European Ceramic Society 29 (2009) 1735.

97. Potrepka. D.M, Tidrow. S.C, Tauber. A, (2002) *"Improved temperature stability of microwave properties in tunable devices using substituted $Ba_{1-x}Sr_xTiO_3$"*, Integrated Ferroelectrics, 42, 97.

98. Prasad.K, Kumar.A, Choudary.S.N, Choudary.R.N.P, (2005) *"Relaxor behaviour of $Pb[(Mg_{3/4}Co_{1/4})_{1/3}Nb_{2/3}]O_3$ ceramic"*, Solid State Ionics 176, 1641.

99. Pu. Y, Chen. W, Chen. S, Langhammer. H.T, (2005) *"Microstructure and dielectric properties of dysprosium-doped barium titanate ceramics"*, Ceramica, 51, 214.

100. Rahaman. M.N, (1995) *"Ceramic Processing and Sintering"*, Marcel Dekker, New York, 2o Edit, 483.

101. Rahaman. M.N, (2008) *"Sintering of Ceramics"*, CRC Press/Taylor and Francis Group, Boca Raton, 55.

102. Randall. C. A, and Bhalla. A.S, (1990) *"Nanostructural – property relations in complex lead perovskites"*, Jpn. J. Appl. Phys., 29, 327.

103. Ravel. B, Bouldin. C.E, Renevier. H, Hodeau. J.L, Berar. J.F, (1990) *"X-ray absorption edge separation using diffraction anomalous fine structure"*, Physical Review B – Condensed Matter and Materials Physics, 60, 778.

104. Reddy. S.B, Rao. K.P, Rao. M.S.R, (2007) *"Observation of high permittivity in Ho substituted $BaZr_{0.1}Ti_{0.9}O_3$ ceramics"*, Appl. Phys. Lett. 91, 022917

105. Rietveld. H.M, (1969) *"A profile refinement method for nuclear and magnetic structures"*, J. Appl. Crystallogr. 2, 65.

106. Rolov. B. N, (1965) *"Effect of composition fluctuation on unsharp ferroelectric transition",* Soviet Phys. Solid state, 6, 1676

107. Rout. S. K, Panigrahi. S, Sinha. E, (2007) *"Dielectric properties and diffuse phase transition in* $Ba_{1-x}Mg_xTi_{0.6}Zr_{0.4}O_3$ *solid solutions"*, Mater. Chem. Phys. 101, 428.

108. Rout. S. K, Panigrahi. S, Sinha. E, Bera. J, Sinha. T.P, (2006) *"Phase formation and dielectric phase transition in* $Ba_{1-x}Ca_xTi_{0.6}Zr_{0.4}O_3$ *solid solutions"*, J. Phy. and Chem Solids, 67 11, 2257.

109. Saha. S, Sinha. T.P, (2002) *"Low-temperature scaling behavior of* $BaFe_{0.5}Nb_{0.5}O_3$*"*, Phys. Rev. B 65, 134103.

110. Salam.R, (1990) *"Trapping Parameters of Electronic Defectes States in Indium Tin Oxide from AC Conductivity"*, Phys. Status Solidi (a) 117, 535.

111. Samara. G. A, (1966) *"Pressure and temperature dependences of the dielectric properties of the perovskites* $BaTiO_3$ *and* $SrTiO_3$*"*, Phys. Rev. 151, 378.

112. Sciau. Ph, Calvarin. G, Ravez. J, (2000) *"X-ray diffraction study of* $BaTi_{0.65}Zr_{0.35}O_3$ *and* $Ba_{0.92}Ca_{0.08}Ti_{0.75}Zr_{0.25}O_3$ *compositions: influence of electric field"*, Solid State Communications, 113, 77.

113. Shan. D, Qu. Y.F, Song. J.J, (2007) *"Dielectric properties and substitution preference of yttrium doped barium zirconium titanate ceramics"*, Solid State Commun. 141, 65.

114. Shanthakumar. P, Balasubramanian. M, Pease. D.M, Frenkel. A.I, Potrepka. D.M, Kraizman. V, Budnick. J.I, Hines. W.A, (2006) *"X-ray study of the ferroelectric* $[Ba_{0.6}Sr_{0.4}][(YTa)_{0.03}\ Ti_{0.94}]O_3$*"*, Physical Review B - Condensed Matter and Materials Physics, 74, 174103.

115. Simões. A.Z, Riccardi. C.S, Cavalcante. L.S, Longo. E, Varela. J.A, Mizaikoff. B, (2007) *"Impact of oxygen atmosphere on piezoelectric properties of* $CaBi_2Nb_2O_9$ *thin films"*, Acta Mater. 55, 4707.

116. Smolensky. G, (1984) "*Ferroelectrics with diffuse phase transition",* Ferroelectricity, 53, 129.

117. Smolenskii. G.A, (1970) *"Physical phenomena in ferroelectrics with diffused phase transition"*, J. Phys. Soc. Japan 28, 26

118. Sobha, K. C. and Rao. K. J, (1995) *"Ac conductivity and transport studies in phosphate glasses with NASICON-type chemistry",* Solid State Ionics, 81,145.

119. Stephens. P.W, (1999) *"Phenomenological model of anisotropic peak broadening in powder diffraction"*, J. Appl. Crystallogr. 32, 281.

120. Tang. X.G, Chew. K.H, Chan. H.L.W, (2004) *"Diffuse phase transition and dielectric tunability of $Ba(Zr_yTi_{1-y})O_3$ relaxor ferroelectric ceramics"*, Acta Mater, 52, 5177.

121. Tang. X.G, Wang. J, Wang. X.X, Chan. H.L.W (2004) *"Effects of grain size on the dielectric properties and tunabilities of sol–gel derived $Ba(Zr_{0.2}Ti_{0.8})O_3$ ceramics"*, Solid State Commun. 131, 163.

122. Tang. X.G, Wang. J, Wang. X.X, Chan. H.L.W, (2004) *"Effects of grain size on the dielectric properties and tunabilities of sol-gel derived $Ba(Zr_{0.2}Ti_{0.8})O_3$ ceramics"*, Solid State Communications, 131, 163.

123. Tang. X.G, Wang. X.X, Chew. K.-H, Chan. H.L.W, (2005) *"Relaxor behavior of $(Ba,Sr)(Zr,Ti)O_3$ ferroelectric ceramics"*, Solid State Commun. 136, 89.

124. Tiwari. V.S, Pandey. D, (1994) *"Structure and Properties of (Ba,Ca) TiO_3 Ceramics Prepared Using $(Ba,Ca)TiO_3$ Ceramics I, Crystallographic and Microstructural Studies"*, J.Am Ceram Soc.II, 77, 1819.

125. Uchino, K. and S. Nomura, (1982) *"Critical exponents of the dielectric constant in diffused-phase-transition crystals"*, Ferroelectrics Lett. Sect, 44, 55.

126. Uchono. K, Sadanaga. E, Hirose. T, (1989) *"Microwave characteristics of $A(B_{3+1/2}B_{5+1/2})O_3$ ceramics (A = Ba, Ca, Sr; B^{3+} = La, Nd, Sm, Yb; B^{5+} = Nb, Ta)"*, J. Am. Ceram. Soc. 72, 1955.

127. Valasek. J, (1921) *"Piezo-Electric and Allied Phenomena in Rochelle Salt"*, Physical Review, 17, 475.

128. Vedrinskii. R.V, Kraizman. V.L, Novakovich. A.A, Demekhin. Ph.V, Urazhdin. S.V, (1998) *"Pre-edge fine structure of the 3d atom K x-ray absorption spectra and quantitative atomic structure determinations for ferroelectric perovskite structure crystals"*, Journal of Physics Condensed Matter, 10, 9561.

129. Verbitskaia. T. N, Zhdanov. G, Venevtsev. I. N, Soloviev. S, (1958) *"Electrical and X-ray Diffraction Studies of the $BaTiO_3$-$BaZrO_3$ System"*, Sou Phys.-Crystallogr, 3, 182.

130. Victor. P, Bhattacharya. S, Krupanidhi. S. B, (2003) *"Dielectric relaxation in laser ablated polycrystalline $ZrTiO_4$ thin films"*, J. Appl. Phys. 94, 5135.

131. W. Kanzig, (1957) "*Ferroelectrics and Antiferroelectrics*", Academic Press, New York.

132. Wang. D, Yu. R, Feng. S, Zheng. W, Takei. T, Kumada. N, Kinomura. N, (2002) *"Hydrothermal synthesis of perovskite-type solid solution of (1-x)$BaTiO_3$·x$La_{2/3}TiO_3$"*, Solid State Ionics, 151, 329.

133. Wang. L.M, Richert. R, (2005*) "Debye Type Dielectric Relaxation and the Glass Transition of Alcohols"*, J. Phys. Chem. B, 109, 11091.

134. Wang. Y, Li. L, Qi. J, Gui. Z, (2002) *"Ferroelectric characteristics of ytterbium-doped barium zirconium titanate ceramics"*, Ceramics International, 28, 657.

135. Watanabe. K, Ohsato. H, Kishi. H, Okino. Y, Kohzu. N, Iguchi. Y, Okuda. T, (1998) "*Solubility of La-Mg and La-Al in $BaTiO_3$*", Solid State Ionics 108, 129.

136. Weber. U, Greuel. G, Boettger. U, Weber. S, Hennings. D and Waser. R, (2001) *"Dielectric Properties of Ba(Zr,Ti)O_3-Based Ferroelectrics for Capacitor Applications"*, J. Am. Ceram. Soc. 84, 759.

137. Weber. U, Greuel. G, Boettger. U, Weber. S, Hennings. D, Waser. R, (2001) *"Dielectric properties of Ba(Zr,Ti)O_3-based ferroelectrics for capacitor applications",* J. Am. Ceram. Soc. 84, 759.

138. Wieczorek. W, Plocharski. J, J. Przyluski, (1988) *"Impedance spectroscopy and phase structure of PEO---NaI complexes"*, Solid State Ionics 28–30, 979.

139. Wood. D.L, Tauc. J, (1972) *"Weak absorption tails in amorphous semiconductors"*, Physical Review B, 5, 3144.

140. Wul. B, Goldman. I.M, (1945) C. R. Acad. Sci. U.R.S.S., 46, 177.

141. Xu. Y, (1991) "*Ferroelectric Materials and Their Applications",* North-Holland Elsevier, Science Publications, Amsterdam.

142. Yang. J.H, Choo. W.K, Lee. J.H, Lee. C.H, (1999) *"The crystal structure of the B-site ordered complex perovskite Sr($Yb_{0.5}$ $Nb_{0.5}$)O_3"*, Acta Cryst. B, 55, 348.

143. Yao. X, Chen. Z, Cross. L.S, (1983) *"Polarization and depolarization behavior of hot presses lead lanthanum zirconate titanate ceramics"*, J. Appl. Phys., 54, 3399.

144. Yu. Z, Ang. C, Guo. R, Bhalla. A. S, (2002) *"Dielectric properties and high tunability of Ba($Ti_{0.7}Zr_{0.3}$)O_3 ceramics under dc electric field"*, Applied Physics Letters, 81, 1285.

145. Yu. Z, Ang. C, Guo. R, Bhalla. A.S, (2007) *"Dielectric properties of Ba($Ti_{1-x}Zr_x$)O_3 solid solutions"*, Mater. Lett. 61, 326.

146. Yu. Z, Guo. R, Bhalla. A.S, (2000) *"Dielectric behavior of $Ba(Ti_{1-x}Zr_x)O_3$ single crystals"*, J. Appl. Phys. 88, 410.

147. Yu. Z, Guo. R, Bhalla. A.S, (2002) *"Dielectric properties and high tunability of $Ba(Ti_{0.7}Zr_{0.3})O_3$ ceramics under dc electric field"*, Appl. Phys. Lett. 81, 1285.

148. Zhai. J.W, Yao. X, Zhang. L.Y, Shen. B, (2006) *"Dielectric nonlinear characteristics of $Ba(Zr_{0.35}Ti_{0.65})O_3$ thin films grown by a sol-gel process"*, J. Appl. Phys. Lett. 84, 3136.

149. Zhang. Q, Cagin. T, Goddard III. W.A, (2006) *"The ferroelectric and cubic phases in $BaTiO_3$ ferroelectrics are also antiferroelectric"*, Proceedings of the National Academy of Sciences of the United States of America, 103, 14695.

150. Zhu. J, Chen. X.B, He. J.H, Shen. J.C, (2007) *"Investigations on Raman and X-ray photoemission scattering patterns of vanadium-doped $SrBi_4Ti_4O_{15}$ ferroelectric ceramics"*, Phys. Lett. A 362, 471.

List of Research Publications/Accepted/Communicated papers

1. **Structure and optical properties of $[Ba_{1-x}Y_{2x/3}](Zr_{0.25}Ti_{0.75})O_3$ powders**
   Sczancoski. J.C, Cavalcante. L.S, **Badapanda. T**, Rout. S.K, Panigrahi. S, Mastelaro. V.R, Varela. J.A, Siu Li. M, Longo. E,
   Solid State Sciences, Volume 12, Issue 7, Pages 1160-1167 (2010)

2. **Structural and dielectric relaxor properties of yttrium-doped $Ba(Zr_{0.25}Ti_{0.75})O_3$ ceramics**
   Badapanda, T, Rout, S.K, Cavalcante, L.S, Sczancoski, J.C, Panigrahi, S, Sinha,T.P, Longo, E,
   Materials Chemistry and Physics, Volume 121, Issues 1-2, Pages 147-153 (2010)

3. **Effect of Dy substitution on dielectric properties of BTZ relaxor ceramics**
   Badapanda, T, Rout, S.K, Panigrahi, S, Sinha, T.P, Woo, S.I.
   Ferroelectrics 385 (1 PART 6), pp. 177-186, (2009)

4. **Photoluminescence property of $Ba(Zr_{0.25}Ti_{0.75})O_3$ powders prepared by solid state reaction and polymeric precursor method**
   Rout. S.K, Cavalcante. L.S, Sczancoski. J.C, **Badapanda. T**, Panigrahi. S, Siu Li. M, Longo. E.
   Physica B: Condensed Matter, Volume 404, Issue 20, 1, Pages 3341-3347 (2009)

5. **Optical and dielectric relaxor behaviour of $Ba(Zr_{0.25}Ti_{0.75})O_3$ ceramic explained by means of distorted clusters**
   Badapanda, T, Rout, S.K, Cavalcante, L.S, Sczancoski, J.C, Panigrahi, S, Longo, E, Li, M.S.
   Journal of Physics D: Applied Physics 42 (17), art. no. 175414 (2009)

6. **Phase formation and dielectric study of Bi doped $BaTi_{0.75}Zr_{0.25}O_3$ ceramic**
   Badapanda, T, Rout, S.K, Panigrahi, S, Sinha, T.P.
   Current Applied Physics, Volume 9, Issue 4, Pages 727-731 (2009)

7. **Relaxor behaviour of $(Ba_{0.5}Sr_{0.5})(Ti_{0.6}Zr_{0.4})0_3$ ceramics**

   Badapanda, T, Rout, S.K, Panigrahi, S, Sinha, T.P.

   Bulletin of Materials Science 31 (6), pp. 897-901 (2008)

8. **Ferroelectric phase transition of $Ba_{1-x}Sr_xTi_{0.6}Zr_{0.4}O_3$ ceramics**

   Badapanda, T, Rout, S.K, Panigrahi, S, Sinha, E, Sinha, T.P.

   Phase Transitions 81 (10), pp. 897-906 (2008)

9. **Dielectric and phase transition of $BaTi_{0.6}Zr_{0.4}O_3$ ceramics prepared by a soft chemical route**

   Rout, S.K, **Badapanda, T**, Sinha, E, Panigrahi, S, Barhai, P.K, Sinha, T.P.

   Applied Physics A: Materials Science and Processing 91 (1), pp. 101-106 (2008)

10. **Dielectric study of spin coated nano-thick $BaZr_xTi_{1-x}O_3$ film**

    Rout, S.K, **Badapanda, T**, Panigrahi, S.

    Indian Journal of Pure and Applied Physics 45 (9), pp. 749-753 (2007)